Techniques for Low Coherence Pulsed Doppler Lidar

A thesis submitted to the
University of Waikato
for the degree
of
Doctor of Philosophy in Physics
by

Adrian Andrew Dorrington

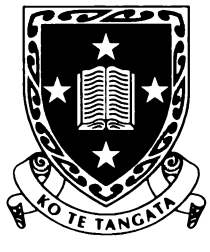

The
University
of Waikato
Te Whare Wānanga
o Waikato
Hamilton, New Zealand

August 2000

Abstract

Wind shear and clear air turbulence are atmospheric phenomena that pose a hazard to aircraft and their passengers. In the past, these phenomena have caused injuries and the occasional death. The ability of a lidar system to make wind speed measurements and detect wind shear and turbulence has been known for some time. However, lidar systems are still not commercially viable as early warning systems in aircraft and at airports. The main reason is the expense and bulk of the single frequency injection-locked lasers currently used. These are required to ensure coherence is maintained between the reference and measurement beams over long pathlength differences.

In order to reduce the cost and size of lidar systems, we have developed new lidar design philosophies based on using components that are cheaper and smaller. Two different techniques are presented in this thesis, one to eliminate the requirement for a highly coherent laser source, and the other provides a method to generate a frequency offset that is an alternative to the currently favoured acousto-optic modulator.

The first approach presented is a design in which a sample of the transmitted pulse is stored in a fibre optic ring resonator of pathlength longer than the pulse. Each time the pulse circulates the storage loop a fraction is split off and used as the reference beam. Because this reference beam has travelled an equivalent distance to the measurements beam, the coherence requirements are relaxed significantly allowing the use of a much cheaper and smaller low coherence source.

In the second method presented, a frequency offset is generated without the use of the currently favoured and relatively expensive acousto-optic modulator. This method utilises a quadrature beam combiner and radio frequency quadrature modulator techniques. Configured as a single sideband (SSB) modulator, two balanced mixers produce double sideband

signals in which one sideband is π out-of-phase. When combined, one sideband cancels leaving a single sideband output containing the baseband Doppler signal shifted up the RF spectrum by a predetermined offset. This is implemented in both electronic and semi-optical configurations.

Concept validation experiments have been performed for both techniques. Using the reference beam storage loop, the velocity of a rotating mirror was measured at several simulated ranges. Successful optical mixing between the stored reference and the delayed measurement beams has been demonstrated. Utilising the SSB offset generation method, the velocity of a piezo mounted mirror has also been successfully measured, after an offset was applied with the new techniques. The results obtained show that both concepts are viable, and that these techniques could be applied in a new lidar design philosophy resulting in significant benefits with respect to complexity, cost, size, weight, and power consumption.

Acknowledgements

The completion of this thesis would not have been possible without the help and support of a great many people, and to them I am grateful. In particular, I would like to extend my gratitude to my supervisor Rainer Künnemeyer for his guidance, support and friendship. The help provided by the rest of the staff and students in the Department of Physics and Electronic Engineering at the University of Waikato is also much appreciated.

In addition, I would like to thank Paul Danehy, Hans Bachor, staff and students in the Department of Physics at the Australian National University for many thought provoking discussions and the loan of equipment.

Thanks to the University of Waikato Postgraduate Scholarship for financial assistance, and to Howell Round and the Department for sponsoring conferences and overseas travel.

Thanks also to the Lyfords for, among other things, numerous free dinners during my (financially challenging) studies, and especially to Mike for his diligent proof reading.

Finally, very special thanks to Belinda for her patience and support, and to Mum and Dad for their encouragement and motivation.

Contents

List of figures

Abbreviations

AC	-	Alternating current
AM	-	Amplitude modulation
AMSC	-	Amplitude modulation, suppressed carrier
AOM	-	Acousto-optic modulator
CMOS	-	Complementary metal oxide semiconductor
CW	-	Continuous wave
DC	-	Direct current
DCM	-	Differential cross multiplier
DIAL	-	Differential absorption lidar
EDFA	-	Erbium doped fibre amplifier
EM	-	Electromagnetic
EOM	-	Electro-optic modulator
FFT	-	Fast Fourier transform
FM	-	Frequency modulation
IC	-	Integrated circuit
IF	-	Intermediate frequency
LDA	-	Laser Doppler anemometry
LDV	-	Laser Doppler velocimetry
LO	-	Local oscillator
NASA	-	National Aeronautics and Space Administration
PBS	-	Polarising beam splitter
PC	-	Personal computer (IBM)
PCB	-	Printed circuit board
PLL	-	Phase-locked loop
RF	-	Radio frequency
S/N	-	Signal-to-noise (ratio)
SSB	-	Single sideband
VCO	-	Voltage controlled oscillator
VHC	-	Very high speed CMOS

Chapter 1
Introduction

Clear-air turbulence and wind shear are two atmospheric phenomena that are of significant concern to the aviation industry. Sometimes referred to as 'rough air' or 'air pockets', these phenomena are characterised by rapidly changing air currents. Although they do not usually cause damage to modern aircraft, they are the leading cause of in-flight injuries and, in extreme cases, death to flight crew and passengers (NASA 1992a).

Atmospheric turbulence is normally associated with visible storm activity, and can be detected by on-board weather radar. However, on the outskirts of a thunderstorm, up to 50 miles from the centre of activity or at high altitudes near the jet stream and in mountainous regions, invisible turbulence can exist in an otherwise clear sky (NASA 1998). This is called clear air turbulence and is most dangerous when encountered unexpectedly.

Wind shear describes a rapid change in wind currents. It can cause the aircraft to stall, or rapidly gain or lose altitude (as illustrated in Figure 1.1), and hence is of the greatest danger during take off and landing. Between 1964 and 1985, wind shear caused 500 fatalities and 200 injuries, involving 26 civil aircraft in the United States of America (NASA 1992b).

Lidar systems have become common tools for the remote, non-contact measurement of atmospheric properties for research applications. A lidar system that could give advanced warning of clear-air turbulence and wind shear would be very useful in the aviation industry.

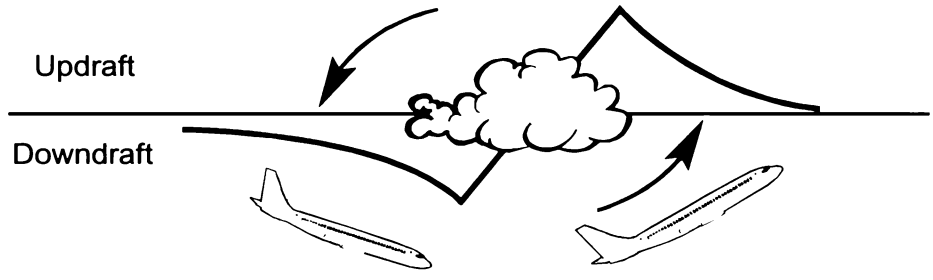

Figure 1.1 – Wind Shear: An aircraft can experience a sudden loss or gain of altitude causing crew passengers and luggage to be tossed about (NASA 1998).

Even though the ability of lidar systems to detect wind speed and turbulence has been proven, no commercial systems have been developed so far. The main reason for this is that designs to date, for long range measurements, require the use of single frequency injection-locked laser transmitters, which are bulky and expensive. This expense and size limits the commercial viability of lidar based early warning detection systems.

The aim of the research presented here is to develop new systems and lidar design approaches that allow the manufacture of cheaper and smaller lidars. This will make lidars commercially feasible and provide a new safety tool for the aviation industry. Two techniques will be presented that permit the replacement of the most expensive and bulky components of current lidar designs with cheaper alternatives.

In the next chapter, the basics of lidar systems are introduced, 'laser Doppler velocimetry' and 'pulsed Doppler lidar' are covered in depth, and the literature relevant to the research is reviewed.

Chapter three describes the first part of the research. A reference beam storage loop is used to relax the coherence requirements and allow the use of a much cheaper and smaller low coherence source in place of the currently favoured injection-locked lasers. Results from a software simulation and an experimental set-up are presented that validate the concept.

The second part of the research is described in chapter four. Single sideband modulation techniques are used as a frequency shifting method

instead of an acousto-optic modulator. Again, the concepts are validated through software simulations and an experimental set-up.

Chapter five reviews the new techniques, concludes that the thesis aims have been achieved, and comments on the application of these techniques to commercial viability lidar systems.

Chapter 2
An introduction to lidar

The word Lidar is an acronym for 'light detection and ranging'. It is a remote sensing technique and describes a device that uses light to determine properties such as distance, velocity, particle size, temperature, and chemical content of one or more objects at a remote location. It is also often referred to as Laser Radar, as its development is an extension of standard radio frequency radar techniques.

This chapter introduces the basics of lidar optical measurement systems. Also explained here are specific details of current lidar design techniques for atmospheric pulsed Doppler lidar relevant to the presented research.

2.1. Lidar overview

There is a great variety of optical measurement techniques that can be classified as lidar. The basic types of optical measurement configurations are explained below, and some common optical measurement systems are discussed in more depth.

2.1.1. Coherent and incoherent lidar

Lidar designs are separated into two broad categories based on the techniques used to detect light scattered from the target and received by the lidar unit.

The first category is termed 'incoherent', also known as 'direct detection' lidar, and is illustrated in Figure 2.1a. In this type of system, laser light from the lidar illuminates a target. Some of this light is scattered back

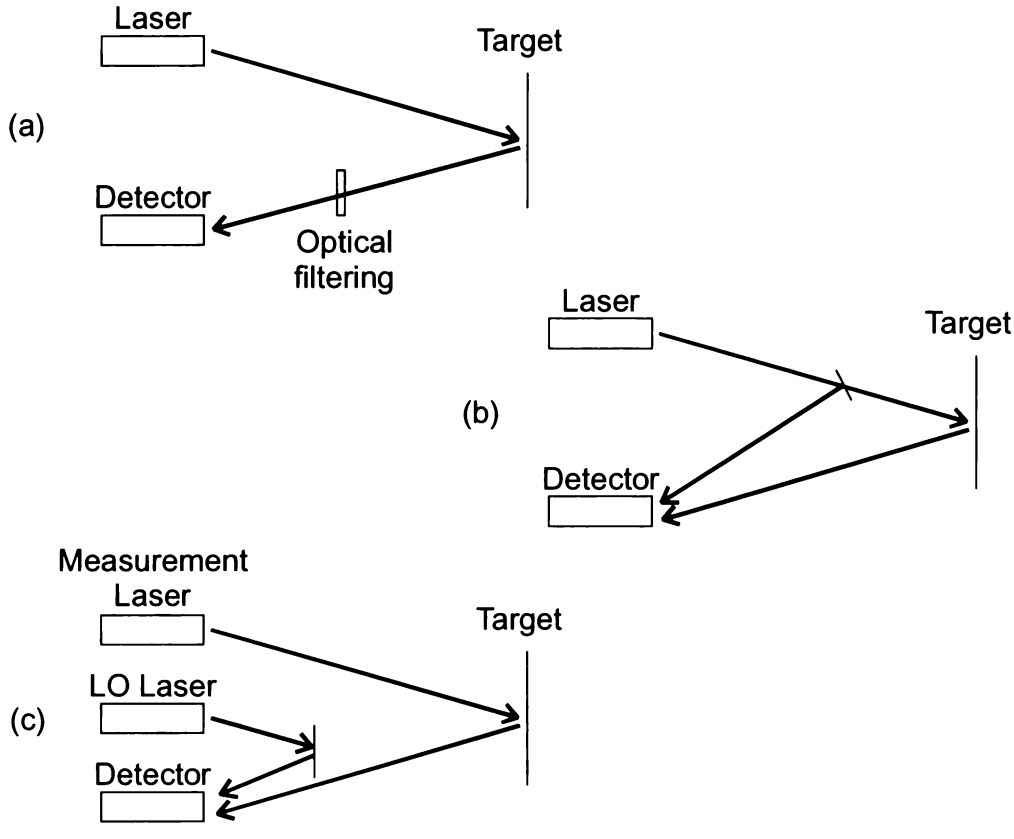

Figure 2.1 – Basic forms of lidar systems: (a) incoherent, (b) homodyne and (c) heterodyne.

towards the lidar where it is then received and detected. Essentially, only the intensity of the received signal is measured, with some systems also making use of timing information and, to a certain extent, spectral information through pre-detection filtering.

In contrast, a 'coherent' lidar decodes the full frequency, phase and timing information of the received signal through optical mixing techniques. There are two different optical mixing configurations employed. Both methods mix the received light with a reference beam generating an intermediate frequency beat signal that is then processed electronically. The simplest is the homodyne method, illustrated in Figure 2.1b, where a portion of the transmitted beam is used as the reference beam. Often this is not practical, so heterodyne techniques are employed. A second local oscillator laser, injection-locked to the transmitting laser, is used as a reference beam generator, illustrated in Figure 2.1c.

2.1.2. Common optical measurement configurations

Two of the most common optical measurement applications are distance and velocity measurement. For each of these applications, there are several possible implementations, utilising both coherent and incoherent techniques. In this section, an overview of these techniques is presented by way of examples. The more common configurations for these two applications will now be described.

2.1.2.1. Distance measurement

The measurement of distance from the lidar to a target object can be realised with two common approaches.

The "Time of Flight" method, illustrated in Figure 2.2a, is probably the most common technique. A pulse of light is transmitted towards, and then scattered by the target. The time required for the pulse to propagate to the target and back to the lidar is measured, which (with knowledge of the speed of light) reveals the distance to the target.

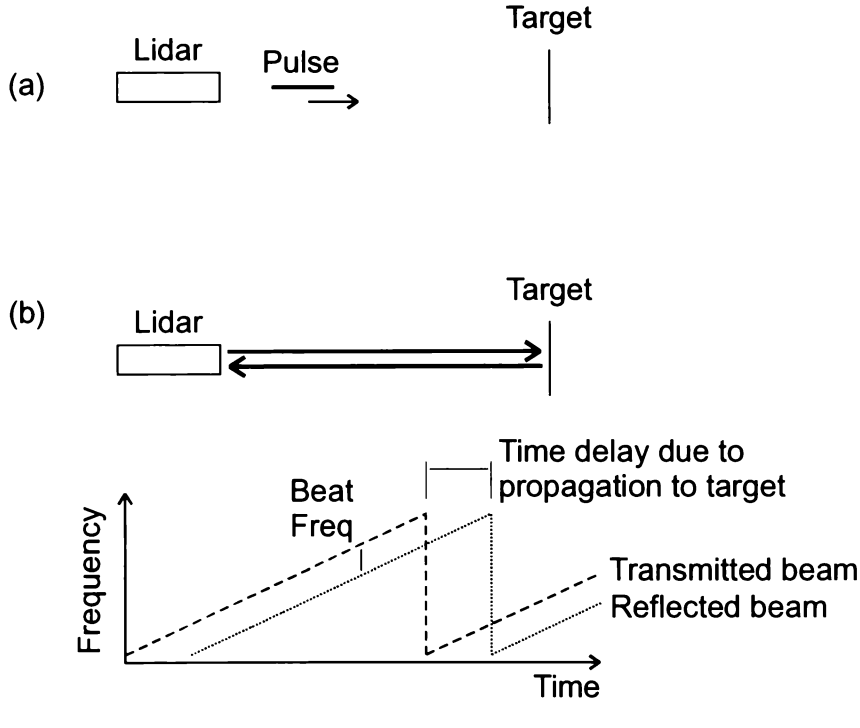

Figure 2.2 – Lidar configurations used to measure distance: (a) time of flight, and (b) continuous wave frequency modulated (CW FM).

The second type of distance measurement uses a coherent system as illustrated in Figure 2.2b. A continuous wave (CW) transmitting laser is frequency modulated (FM) at a constant rate, in a triangle or saw-tooth fashion. At any given distance, the received light is time delayed due the propagation of the measurement beam from the lidar to the target, and back. This results in a frequency difference between the received signal and the reference beam causing a beat frequency when the signals are mixed optically. As the frequency difference is dependent on propagation time, the frequency of the beat signal is proportional to distance. This system is termed FM CW lidar.

2.1.2.2. Velocity measurement

The measurement of velocity is one of the most common uses for coherent lidar. The principle relies on the Doppler shift imparted on a light beam scattered by a moving target. Through optical mixing techniques a beat signal is produced that has a frequency proportional to the Doppler shift, and hence the target's velocity. These types of systems are called Laser Doppler Velocimeters (LDV) or Laser Doppler Anemometers (LDA). The simplest implementation is known as the reference beam technique, where scattered light beats with a reference beam in a homodyne fashion very similar to that described previously. Other techniques include the differential and the dual scatter techniques.

The differential technique uses two laser beams intersecting at the point of interest. A beat signal is produced by optically mixing scattered light from one beam that has been shifted up the frequency spectrum (due to the Doppler effect), and from the other beam that has been shifted down. An alternative explanation is: the intersecting beams create an interference pattern of bright and dark bands, and as a particle traverses the pattern it scatters light alternately from these bright and dark bands causing an oscillating signal proportional to velocity. The Dual Scatter technique is very similar, but the target is illuminated with one beam and scattered light is collected from two directions. All of these LDV techniques are described in more detail in the following section.

Velocity can also be measured with the use of incoherent techniques. In this case, the transmitting laser is tuned near the cut-off of a high-resolution optical filter, such as a Fabry-Perot etalon or iodine molecular filter (McGill and Skinner 1997). The received light is passed initially though a relatively broad filter to reject background light, then through the high-resolution filter causing attenuation of the signal proportional to the Doppler shift imparted upon it. From knowledge of the intensity ratio of the filtered and unfiltered received light and the filter characteristics, the velocity of the target can be derived. This is known as the edge technique and is illustrated in Figure 2.3.

2.1.3. Atmospheric applications

Lidar has become an important and powerful remote sensing tool for atmospheric research. It provides the ability to make multiple

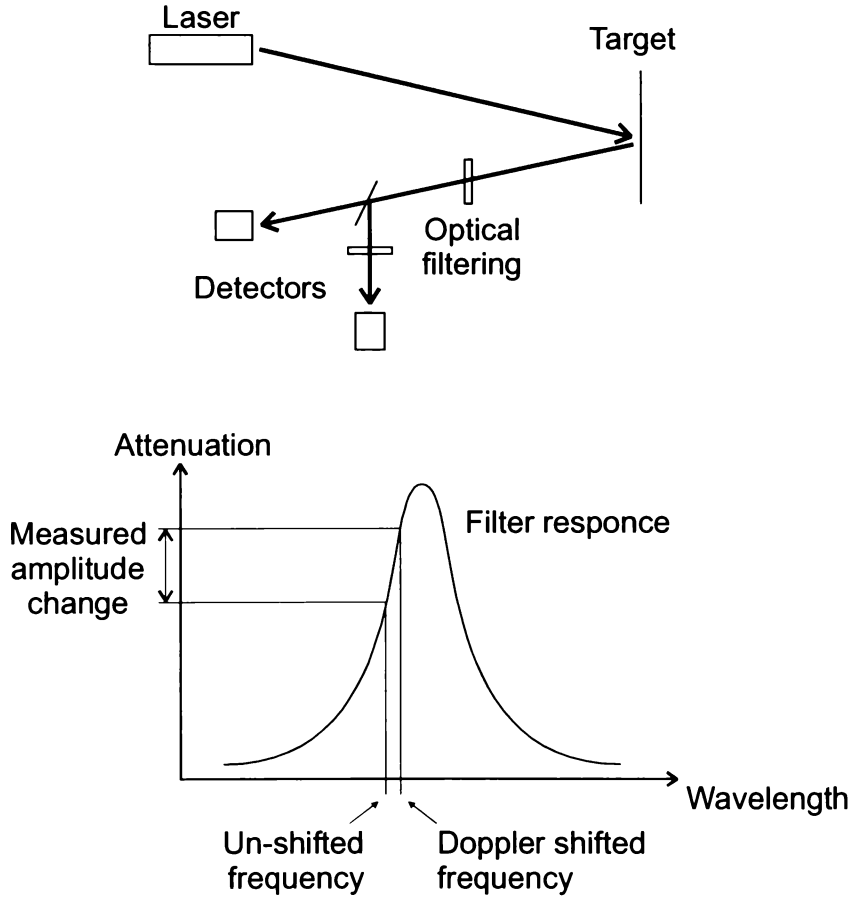

Figure 2.3 – The edge technique using two detectors. The received Doppler shifted light detected before and after a high-resolution optical filter. The amplitude ratio indicates target velocity.

measurements over long range in a short period of time. As a result, significant improvements have been made in the understanding of atmospheric behaviour, which in turn leads to improved weather prediction.

Although the hard target and point sensing applications described above are in the strictest meaning of the word lidar systems, they are not normally referred to as such. Instead, the word lidar is usually reserved for atmospheric sensing applications. The two main atmospheric applications of lidar systems are chemical content analysis using an implementation called Differential Absorption Lidar (DIAL), and wind speed velocimetery using a form of LDV, which is referred to as Doppler Lidar.

2.1.3.1. Differential absorption lidar

Atmospheric parameters such as cloud water content, ozone density, and chemical pollutants can be identified with differential absorption lidar. In this system (illustrated in Figure 2.4), the target is illuminated with laser light containing two or more wavelengths. One wavelength is chosen specifically to coincide with the absorption lines of the chemicals under investigation, while the other is chosen such that it is not absorbed. The amplitude ratio of the received light at the absorbed and non-absorbed wavelengths provides an indication of the abundance of chemicals of interest (Singh 1997).

2.1.3.2. Lidar for wind speed measurement

The simplest examples of lidar systems for wind speed measurement are the reference beam and differential Doppler LDV (Drain 1980, Woodfield 1986, and Rogers 1989). In these implementations the wind velocity at only one location can be studied. Modern lidar systems however, utilise a pulsed measurement laser allowing the acquisition of many sequential measurements along the laser beam's line of propagation.

The principle of coherent lidar is illustrated in Figure 2.5. A pulsed laser beam is generated and directed into the atmosphere. As this pulse propagates light is scattered by air molecules (Rayleigh scattering) and by

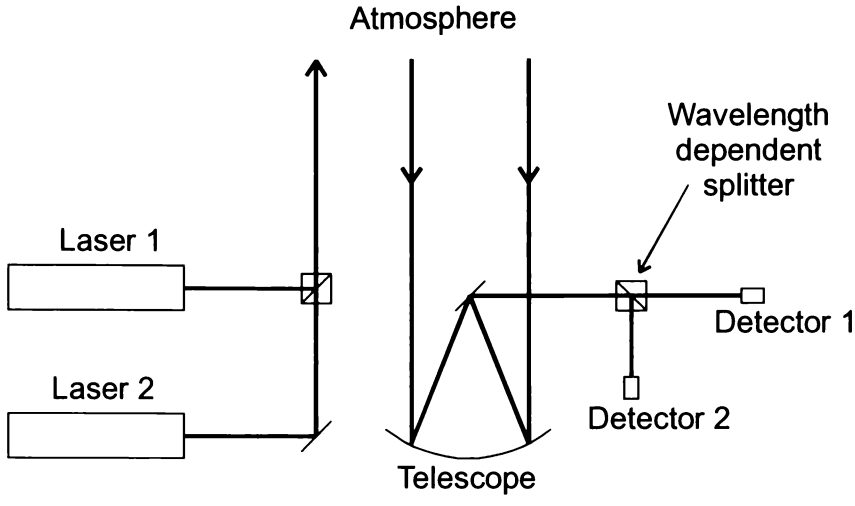

Figure 2.4 – Differential absorption lidar (DIAL), with two laser beams of different wavelengths directed into the atmosphere. The telescope collects the scattered light and directs it to two detectors, one for each wavelength.

larger aerosol particle (Mie scattering). A portion of this scattered light finds its way back along the transmitted beam path to the lidar unit where it is processed to determine various properties of the scattering particles. The scattered light is collected and optically mixed with a reference beam generated either by sampling a portion of the transmitted beam (homodyne detection), or by a separate injection-locked local oscillator laser (heterodyne detection).

2.2. Laser Doppler velocimetry

Laser Doppler Velocimetry (LDV) is a technique that has become very popular for non-contact velocity measurement of liquids, gases and solid surfaces. There are a variety of optical configurations in use. Almost all of these are based on the optical homodyne technique, which utilises a monochromatic laser light source and optical mixing to determine the Doppler shift imparted by the object under investigation.

This section describes the three basic LDV optical configurations, as well as their theory of operation.

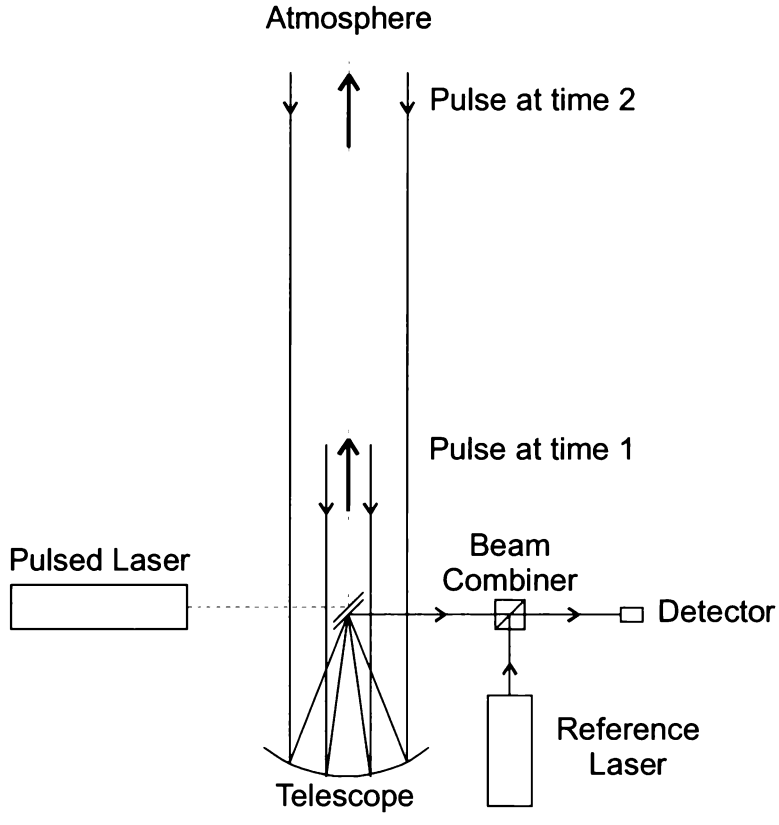

Figure 2.5 – Pulsed lidar concept, showing scattered light from two separate instances in time, collected and optically mixed with a reference beam (Richter et al. 1994).

2.2.1. Reference beam technique

A typical optical arrangement of a reference beam LDV system designed to measure the flow velocity of a liquid or gas in a pipe is illustrated in Figure 2.6. Emitted laser light (the measurement beam) is directed towards the flow where it is scattered by moving particles. This scattered light is collected and then combined with a portion of the measurement laser beam used as the reference beam. The area in space that is illuminated by the laser and is visible from the detector optics is the only area in which velocity measurements can be made. This is called the measurement volume. Optical mixing between the reference beam and the scattered light occurs on the detector, which results in a beat signal that has a frequency proportional to the Doppler shift. Electronics are then employed to decode the beat signal and derive the velocity of the particles.

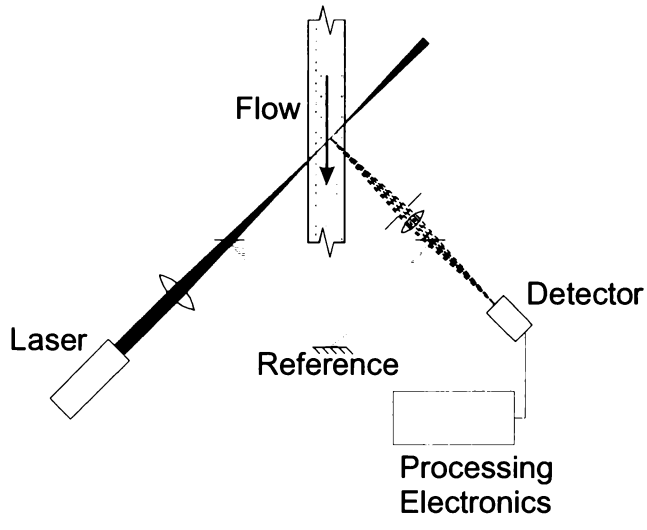

Figure 2.6 – Reference beam Laser Doppler Velocimeter arrangement measuring flow of a liquid or gas in a pipe (Drain 1980).

In the following sections, the operational theory of LDV systems is discussed in detail.

2.2.1.1. Light source

As previously mentioned, light reflected or scattered off a moving target exhibits a change in frequency due to the Doppler effect. Up until the advent of the laser, it was not possible to measure this shift because the available light sources were not sufficiently monochromatic and coherent. However, it is possible to distinguish between a Doppler shifted laser beam and a non-shifted one, and hence measure a shift imparted by a moving target. This is possible because the line width of the laser is sufficiently narrow in comparison with the Doppler shift.

Coherent LDV systems employ homodyne (or heterodyne) optical mixing, described in more detail in the following sections, to determine the Doppler shift. Optical mixing can only occur if the two beams being mixed are coherent with one another. For this reason, the coherence length of the laser must be taken into account when selecting a light source and designing the optical arrangement of the velocimeter. This is particularly relevant when there is a large difference in the optical pathlength of the measurement and reference beams.

2.2.1.2. The Doppler shift

The Doppler effect describes the change in frequency when a source emitting a wave, and a receiver detecting the wave are in motion relative to each other. One common example is a car passing a stationary observer with its horn sounding. The horns pitch appears to be higher as the car approaches and lower as it moves away.

It also describes the situation where the source and receiver are stationary, relative to each other, and the wave is reflected off a moving obstacle. This is the case for Laser Doppler Velocimetey.

Figure 2.7a illustrates the situation were the source is stationary, and the receiver is moving. From the receiver's point of view, the wave fronts are approaching more rapidly, because it is moving towards them. Therefore, more wave fronts are encountered in any given time period, resulting in a higher perceived frequency.

More specifically, the velocity of the wave appears to have increased by the velocity of the receiver along the line between the source and receiver.

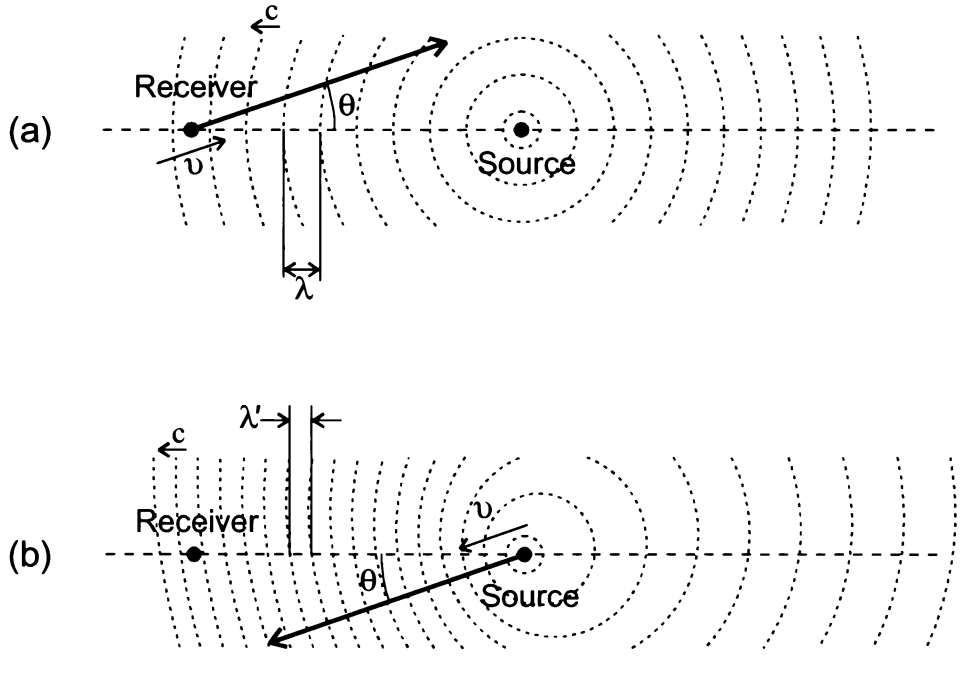

Figure 2.7 – Doppler shifts with: a) a moving receiver, b) a moving source.

This new velocity is

$$c' = c + v \cdot \cos\theta \tag{2.1}$$

where c is the wave front velocity and θ is the angle between the direction of motion and a line passing through both the receiver and transmitter. The frequency perceived by the receiver is therefore

$$\nu' = \frac{c + v \cdot \cos\theta}{\lambda} \tag{2.2}$$

which, in terms of emitted frequency is

$$\nu' = \nu\left(1 + \frac{v}{c}\cos\theta\right) \tag{2.3}$$

In the case of a moving source and a stationary receiver, as illustrated in Figure 2.7b, the wave velocity remains constant from the receiver's point of view. However, the spacing between the wave fronts is reduced because by the time a new wave front is emitted, the source has moved closer, and "caught up" to some degree, to the previous one. As a result, the receiver perceives a shorter wavelength.

We can calculate the new wavelength by subtracting the distance travelled by the source in one wave period from the emitter wavelength and find

$$\begin{aligned} \lambda' &= \lambda - \frac{v \cdot \cos\theta}{\nu} \\ &= \frac{c - v \cdot \cos\theta}{\nu} \end{aligned} \tag{2.4}$$

The perceived frequency can now be found as

$$\begin{aligned} \nu' &= \frac{c}{\lambda'} \\ &= \frac{c}{\frac{c - \upsilon \cdot \cos\theta}{\nu}} \\ &= \frac{\nu}{1 - \frac{\upsilon}{c}\cos\theta} \end{aligned} \qquad 2.5$$

These derivations do not hold for Doppler shift applied to light, or any other electro-magnetic wave. The problem arises initially in the case of a moving receiver where the received wave velocity is increased. This, however, is not possible for light waves, as the speed of light is a constant irrespective of the source and receiver's relative motion.

In the relativistic situation, the moving receiver experiences time dilation (the slowing of time), as described by Einstein's special theory of relativity. Expressed algebraically (Tippler 1983) as

$$\Delta t = \frac{\Delta t'}{\sqrt{1 - \frac{\upsilon^2}{c^2}}} \qquad 2.6$$

This compensates for the velocity increase, resulting in the perceived wavefront velocity remaining constant, and because time has slowed more wave fronts are encountered in a given period, hence the frequency shift is maintained. The relativistic Doppler shift for a moving receiver then becomes

$$\nu' = \nu \frac{1 + \frac{\upsilon}{c}\cos\theta}{\sqrt{1 - \frac{\upsilon^2}{c^2}}} \qquad 2.7$$

In the receiver's frame of reference, a moving source experiences length contraction

$$L' = \sqrt{1-\frac{v^2}{c^2}}L_0 \qquad 2.8$$

and therefore the Doppler shift becomes

$$\nu' = \nu \frac{\sqrt{1-\frac{v^2}{c^2}}}{1-\frac{v}{c}\cos\theta'} \qquad 2.9$$

where θ' is θ transformed into the receiver's frame of reference.

In most LDV situations, and specifically in the case of wind speed applications that are investigated in this thesis, the velocities are very much less than the speed of light. Hence, the first order approximations of the relativistic expressions are adequate. These approximations are the same as the original expressions derived before the relativistic transformations were applied, and hence these simplified expressions will be used from here on.

Figure 2.8 illustrates the situation of a stationary source and receiver, with the wave reflected off a moving particle. In this case, the received wave has undergone two Doppler shifts. The moving particle sees the first shift as a moving receiver, and therefore perceives the frequency as

$$\nu' = \nu\left(1+\frac{v}{c}\cos\theta_1\right) \qquad 2.10$$

where θ_1 is the angle between the particle's trajectory and the line between the source and particle. It then re-emits the wave to the receiver as a moving source, where the receiver perceives the frequency as

$$\nu'' = \frac{\nu'}{1-v/c\cdot\cos\theta_2} \qquad 2.11$$

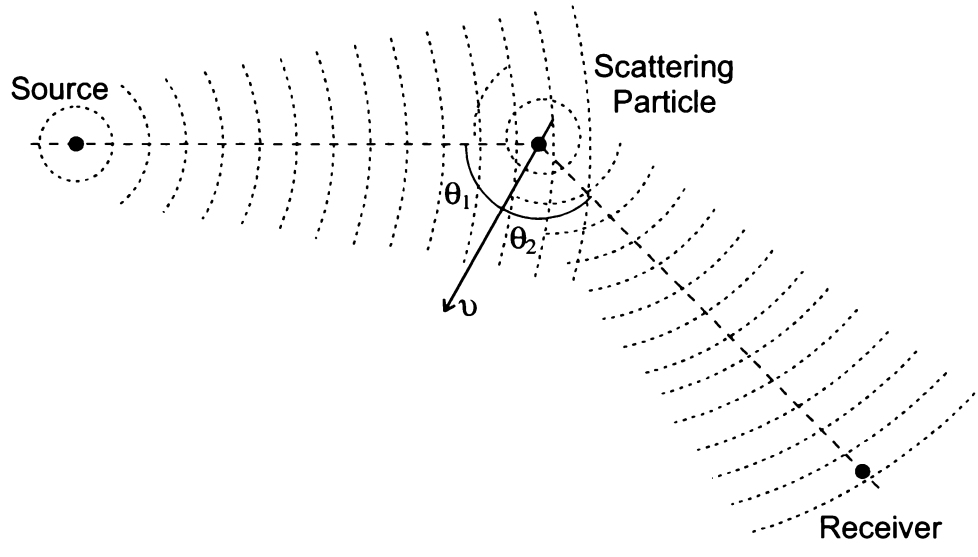

Figure 2.8 – Doppler shift of scattered light from a moving particle with a stationary source and receiver.

where θ_2 is the angle between the particle's trajectory and the line between the receiver and particle.

Substituting equation 2.10 into 2.11 we find the received frequency as a function of transmitted frequency

$$\nu'' = \nu \frac{1+\frac{\upsilon}{c}\cos\theta_1}{1-\frac{\upsilon}{c}\cos\theta_2} \qquad 2.12$$

It can be seen from this expression that no Doppler shift will be observed if $\theta_1+\theta_2=\pi$, which means that the source and receiver are at right angles.

2.2.1.3. Scattering

Scattering is the interaction of light with matter. It is the process of absorption and re-radiation of EM waves. According to Bohren (1995), matter can be considered as a coherent array of dipole antennas that, upon exposure to a primary EM field, resonate and emit a secondary EM field. The superposition of these two fields is the resulting scattered radiation. Bohren also suggests that reflection and diffraction are simply a special case of scattering. For example, reflected light is described as the interference pattern generated by a vast number of scattered waves. This

concept is supported by Born and Wolf (1980) who treat scattering in terms of diffraction.

The theory presented by Mie in 1908 was one of the first to completely describe how EM waves are scattered by a sphere (Bohren 1995). It was an improvement on the older work by Rayleigh, which is only applicable to objects whose diameter is less then one wavelength of light.

There is a marked difference between the scattering behaviours of particles of a diameter greater than and less than a wavelength of light. As a result, the term Rayleigh scattering is commonly used to describe scattering from small particles, and Mie scattering for scattering from large particles. In LDV terms, the most important difference is the forward to backscatter ratio. In the larger particle situation, there is approximately 100 to 1000 times more forward-scatter than backscatter, and side-scatter can vary dramatically depending on the particle. However, for particles smaller than one-third the wavelength of light, forward to backscatter ratios of close to 1 can be observed, and there is very little side-scatter (Drain 1980, Born and Wolf 1980).

Another important parameter for LDV is the scattering cross-section, or the effective scattering area, which is the ratio of incident light to the total scattered light. For larger particles, this is approximated as twice the geometrical cross-section of the particle. Smaller particles, however, have a scattering cross-section that is proportional to the particle's radius to the sixth power, and is inversely proportional to the wavelength of the incident light to the power of four (Drain 1980).

Often there are very few scattering particles in LDV applications, or the scattering cross-section of the particles is very small in the flow under study. Consequently, the returned signal is not measurable. In these situations, scattering particles are artificially added to the flow to enhance scattering and the returned signal. This technique is called 'seeding the flow'.

2.2.1.4. Optical mixing and detection

When light is incident on a detector, such as a photodiode or photomultiplier tube, a photo current is produced proportional to optical intensity. When two or more EM waves are incident on the same detector, the combined intensity causes a photo current. However, if the EM waves are coherent, they will interact producing an interference pattern on the detector resulting in a detected beat signal.

Optical intensity is equivalent to the magnitude squared of the complex amplitude (Saled and Teich 1991). To illustrate a beat signal produced by two coherent waves of different wavelengths and different phases, consider the complex wavefunction expression for combination of these two beams

$$U(t) = \alpha \exp(j\omega_1 t + \varphi_1) + \beta \exp(j\omega_2 t + \varphi_2) \qquad 2.13$$

where ω_1 ($=2\pi\nu_1$) and ω_2 ($=2\pi\nu_2$) are the angular frequencies of the two beams, φ_1 and φ_2 are the phases, and α and β are the amplitudes. Note that the spatial dependence has been suppressed for convenience.

If these beams are incident on a detector, the magnitude squared of equation 2.13 must be calculated to find the intensity, and hence the photo current generated in the detector

$$\begin{aligned} I(t) &= \left|\alpha \cdot \exp[j(\omega_1 t + \varphi_1)] + \beta \cdot \exp[j(\omega_2 t + \varphi_2)]\right|^2 \\ &= \alpha^2 + \beta^2 + 2\alpha\beta \cos(\omega_1 t - \omega_2 t + \varphi_1 - \varphi_2) \end{aligned} \qquad 2.14$$

The resulting signal (in equation 2.14) consists of a constant intensity, or DC offset combined with a time varying component at a frequency equal to the difference between the frequencies of the originally mixed beams.

Consider now the LDV application of optical mixing, and the two beams described above are the reference beam and scattered light from a moving target. Then the beat signal is the difference in frequency between the reference beam and the scattered light, which has a Doppler shift imparted by the target. Hence, the frequency of the electronic signal is directly proportional to the target's velocity.

2.2.1.5. Optical pre-processing

As mentioned above, coherent LDV systems cannot discriminate direction. This is because the optical mixing process provides only the frequency difference, which is the same regardless of whether the scattered light is Doppler shifted up or down in frequency. There are several methods of producing direction discriminating signals by using optical devices to pre-process the laser beam prior to mixing and detection. These methods, most of which are described by Drain (1980), are explained below. References to other authors are given when not covered by Drain.

Two Phase Detection

By producing two Doppler signals that have a phase difference of $\pi/2$, direction can be discriminated by determining which signal leads or lags the other. Methods of generating such signals include:

- Using orthogonal polarised beams, generating a polarisation based beat signal which is separated into its vertical and horizontal components before being detected.

- Aligning the beams entering the combining beam splitter with a slight angle produces an interference pattern, which is passed through gratings before detection (Weir et al. 1991).

- Utilising a beam combiner that is capable of producing outputs with the desired phase difference. The most common type of beam combiner for this application is a 3x3 fibre optic coupler, as demonstrated, for example, by Lo et al. (1997), Koo et al. (1982), and Sheem (1980).

Frequency Shifting

Another approach is to apply a frequency shift to the measurement beam, reference beam, or both, which results in a zero velocity beat signal that has a fixed frequency offset. Movement of the target in one direction causes an increase in the beat frequency and movement in the other a decrease. Optical frequency offset can be achieved with the use of:

- Rotating diffraction gratings, which produce diffracted beams that are shifted in frequency proportionally to the speed of rotation.

- Acousto-optic modulators (AOM), which diffract the incident light in a similar way to rotating diffraction gratings, but with the use of acoustic waves induced in a crystal by a piezoelectric device. Such systems are used routinely and can be found frequently in the literature.

- Electro-optic modulators (EOM), which can be configured as phase modulators, or used to create beams with rotating polarisation.

- Piezoelectric mounted mirrors used as phase modulators by making small changes to the pathlength of one of the beams.

- Lasers frequency modulated (FM) by a triangle or saw-tooth signal and delay lines. Demonstrated by Czarske and Muller (1996), this system relies on mixing two (or more) beams that have a constantly changing frequency and several optical delays, causing a constant frequency difference.

- Two modes from the same laser source, which are optically mixed (Biselli and Werner 1989).

2.2.1.6. Doppler signals

To measure velocity, the frequency of the beat produced when the scattered light is optically mixed with the reference beam must be determined. As mentioned before, the frequency of the beat signal is the difference between the frequency of the reference beam and the Doppler shifted measurement beam. By rearranging equation 2.12, the change in frequency or Doppler shift can be found as

$$\Delta\nu = \frac{1+\frac{\upsilon}{c}\cos\theta_1}{1-\frac{\upsilon}{c}\cos\theta_2} \qquad 2.15$$

As described by Drain (1980): the velocities being measured will always be much less than the speed of light, so we can consider the first order approximation of this expression

$$\Delta v = \frac{2v}{c}(\cos\theta_1 + \cos\theta_2) \qquad 2.16$$

If α is the angle between the illumination and observation directions (in Figure 2.8)

$$\alpha = \pi - (\theta_1 + \theta_2) \qquad 2.17$$

and β as the angle between the direction of particle motion and the bisector for of the illumination and observation lines

$$\beta = \frac{\theta_1 - \theta_2}{2} \qquad 2.18$$

then, the expression for detected Doppler frequency simplifies to

$$\Delta v = \frac{2v}{\lambda}\cos\beta \sin\frac{\alpha}{2} \qquad 2.19$$

Note that the Doppler frequency is dependent on the angle of illumination and observation, and hence if the detection aperture is large, a range of Doppler frequencies will be detected. To increase accuracy, this aperture must be small which decreases the amount of light detected and results in a poor signal-to-noise ratio.

The nature of the detected signal depends dramatically on the optical set up, and what is being measured. A velocimeter measuring a reasonably flat solid surface travelling at a constant velocity would produce a constant amplitude and constant frequency sine wave, as illustrated in Figure 2.9a. If the velocity were to fluctuate, the frequency of the Doppler signal would fluctuate accordingly.

When measuring liquids and gases, the beat signal is not continuous, as it is for a solid surface, because the scattering particles are not distributed at

fixed distances or locations. If a flow contains only few particles, there would usually be only one particle in the measurement volume at a time. This gives rise to a Doppler burst signal, illustrated in Figure 2.9b, as the particle enters, traverses and exits the measurement volume.

As the density of scattering particles increases, the bursts become closer in time, and eventually combine to a continuous signal (Figure 2.9c). The Doppler signal varies in amplitude and is subject to phase changes because

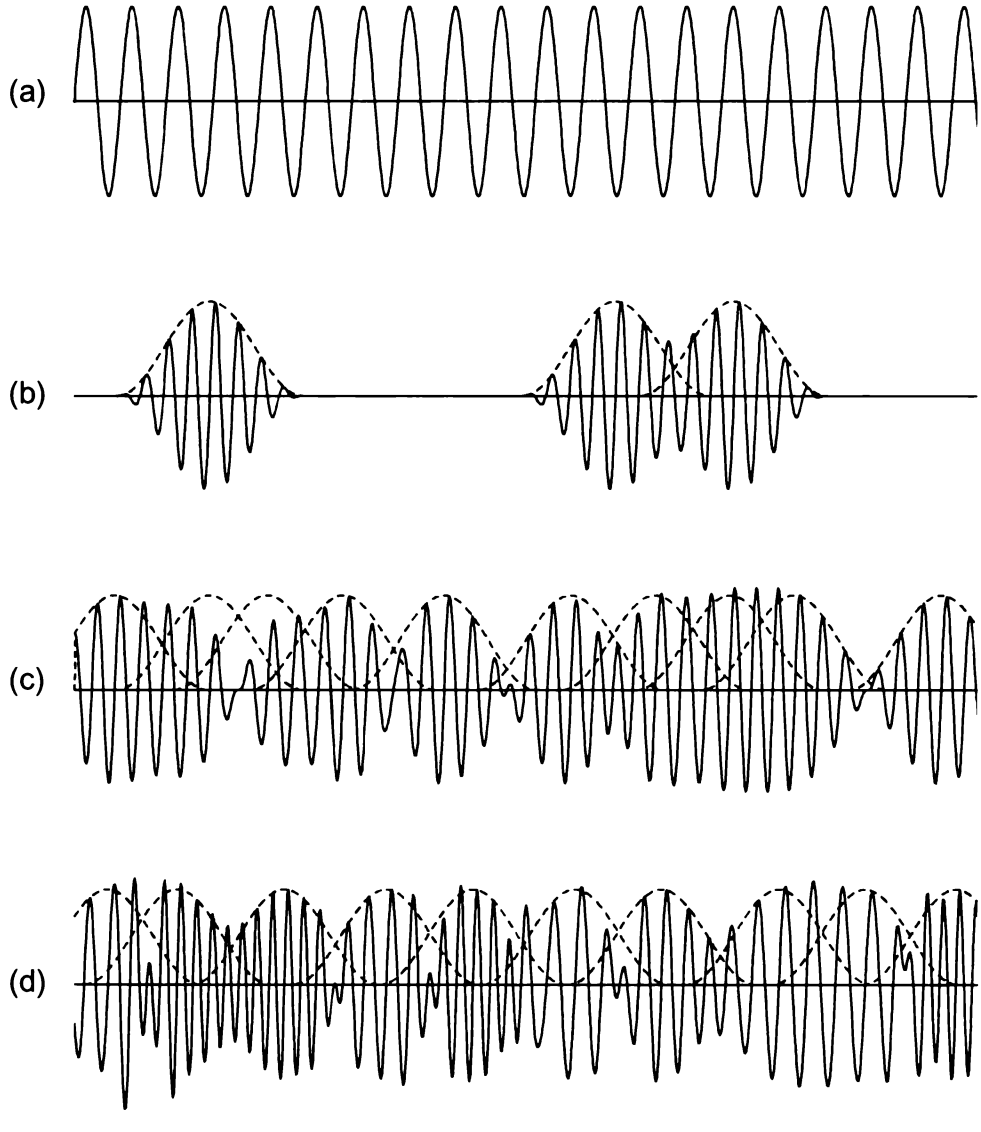

Figure 2.9 – Simulated Doppler signals (solid line) and burst envelopes (broken line): (a) constant amplitude and phase from a relatively flat solid surface, (b) Burst signal scatted from medium with low particle density, (c) varying amplitude and phase signal from higher particle density medium, and (d) varying amplitude, phase and frequency from turbulent medium.

each individual Doppler burst has a different amplitude and phase. In the case of a turbulent flow, illustrated in Figure 2.9d, each burst may have a different frequency giving rise to a broad peak in the spectrum of the Doppler signal.

2.2.1.7. Processing

In order to provide a direct indication of velocity the Doppler beat signal needs to be processed to establish its frequency (and to compensate for any offset that may have been applied). Originally, existing laboratory equipment was used as a frequency estimator.

A frequency counter can be used to determine the frequency of a Doppler signal. However, a spectrum analyser can decode the Doppler signal and provide much more information. Average velocity is indicated by the frequency peak, and information relating to the turbulent or laminar nature of the flow can be deduced from the peak width.

In order to increase the accuracy and ease of use of Doppler frequency estimators, custom electronics have been designed. There is no single solution for signal processing as each velocimetery application produces Doppler signals with varying characteristics. Most of the fundamental analogue processing schemes are explained by Drain (1980) and are summarised below:

- Frequency trackers: In this system, the output from a voltage controlled local oscillator (VCO) is mixed with the incoming Doppler signal to produce an intermediate frequency (IF). A feedback circuit is used to ensure that the IF signal remains at a constant pre-defined frequency by adjusting the VCO output. As a result, the VCO tracks any changes in the Doppler signal, and therefore its controlling voltage can be taken as the decoded velocity output. Additional signal level monitoring circuitry is also employed to determine if the Doppler signal has "dropped out", and therefore has become unusable. Follett (1981) presented a similar arrangement, which

includes filtering circuitry that allows the tracking of the maximum Doppler frequency of a spectrally broad signal.

- Filter bank: In this system, the Doppler signal is passed through an array of band-pass filter's, whose centre frequencies are equally spaced in the frequency domain such that they cover the range of interest. The ratio of the filters outputs provides information of the measured velocity. The resolution of such a system is relatively poor, but may be the best choice of processor for noisy intermittent signals.

- Photon correlation: In extremely low light situations, a varying amplitude signal may not be detectable, but instead only single photon events. However, it is often still possible to reconstruct the Doppler signal by counting the number of photons in a fixed period and building a representation of photon density quantised in time.

In more recent times, digital processing of the Doppler signals has become practical. The simplest form of digital processing is performing a Fast Fourier Transform (FFT) on sampled data, which is similar to using an analogue spectrum analyser, as described above. The main advantage of the digital system is that the spectrum is not affected by the limitations of an analogue analyser. These include analogue mixing bandwidth and timing limitations associated with the spectral scanning process. However, digital systems are usually limited by their maximum sampling rate.

Another digital processing method is the implementation of a digital correlator to combat poor signal-to-noise ratios (Ikeda and Nakajima 1996, Zeitler 1997). More commonly, however, digital decoding techniques concentrate on the processing of quadrature Doppler signals (two or more signals with a phase difference of $\pi/2$).

Quadrature signals can be generated by optical two-phase arrangements (described previously), and also by quadrature demodulation of the Doppler signal (Agrawal 1984, Czarske and Müller 1996, Czarske and Dölle

1998). Quadrature demodulation requires two mixing operations, each producing one of the two quadrature outputs. One output is generated by mixing the input with a carrier signal, and the other by mixing the same input with the carrier phase shifted by $\pi/2$. For LDV situations, the input is the frequency shifted Doppler signal, and the carrier is the frequency shifting AOM drive.

Contained within the quadrature signals are the real and imaginary parts of the Doppler signal. As a result, these can be used to derive the phase change of the Doppler shifted light, in addition to the previously detected amplitude change. The simplest method of processing the real and imaginary signals is to perform a complex FFT, which provides a better phase discrimination than a standard FFT. A more common approach however is to derive the phase change signal, which can provide directional velocity information even if the Doppler signal contains less than one complete cycle.

The two main methods for extracting phase change information are the differential-cross multiplier (DCM) and arctangent algorithms, which are described by Lo and Sirkis (1995), and Müller et al. (1997). In digital implementations, no one of these methods outperforms the others, however, DCM can be implemented in analogue electronics (Koo et al. 1982). Czarske et al. (1993) describe an electronic system, rather than the software implementations described so far, for decoding a digitised version of the phase change signal.

2.2.2. Other techniques

Besides the reference beam method, there are two other common optical arrangements for LDV systems. The methods and techniques capable of determination of velocity components in more than one direction are discussed below. Also covered briefly are possible modifications to the optics aimed at reducing the large DC outputs typical of LDV systems.

2.2.2.1. Differential Doppler

The Differential Doppler technique, illustrated in Figure 2.10a, is another LDV optical configuration. Its principle of operation is fundamentally the same as the reference beam technique, but two measurement beams are imaged into the measurement volume rather than one, and no reference beam is used.

Unlike the reference beam method, which measures the component of velocity that is in the direction of propagation of the measurement beam, the differential technique measures the velocity component that is perpendicular to the bisector of the measurement beams.

Consider each measurement beam, and the scattered light from that beam, separately until the two beams reach the detector. At this point optical mixing occurs between the two scattered beams, one of which has been Doppler shifted up in frequency, and the other down. In other words, the frequency of the detected signal is the difference between the Doppler shifts from both measurement beams.

If the angle of observation changes, the Doppler shift from one beam will

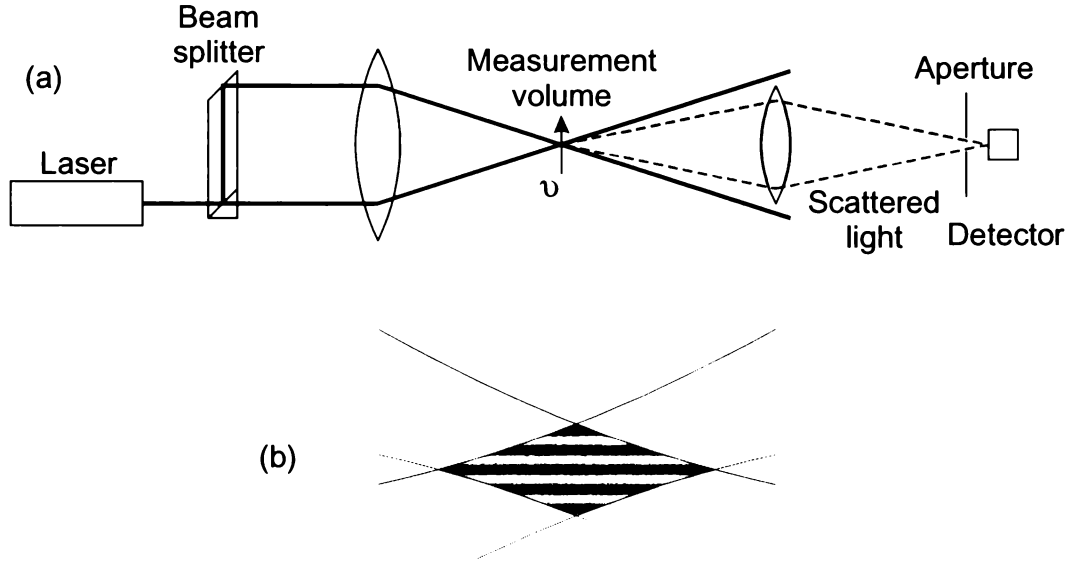

Figure 2.10 – The Differential Doppler technique: (a) optical arrangement and (b) enlargement of measurement volume showing fringe pattern.

increase, and from the other beam decrease. As a result, the difference remains the same, and the detected signal (frequency) is independent of observation angle. Because of this the detection aperture can be increased, and more light collected resulting in a better signal-to-noise ratio than can be achieved with the reference beam technique. For this reason, the differential Doppler technique has become the most common implementation for LDV systems.

A common alternative explanation (Drain 1980) is that the intersecting measurement beams form a set of inference fringes (illustrated in Figure 2.10b). The spacing of the fringes can be calculated from the following expression

$$s = \frac{\lambda}{2\sin\left(\frac{\alpha}{2}\right)} \qquad 2.20$$

where λ is the wavelength of light and α is the angle between the measurement beams. As a particle passes through these fringes of alternating light and dark bands, it scatters light of alternating intensity.

The alternating intensity detected is the Doppler signal, which has a frequency of

$$f = \frac{2\upsilon\cos(\beta)\sin\left(\frac{\alpha}{2}\right)}{\lambda} \qquad 2.21$$

where υ is the velocity of the particle and β is the angle between the direction of motion perpendicular to the fringe patterns.

2.2.2.2. Dual scatter technique

The arrangement illustrated in Figure 2.11 is referred to as the Dual Scatter technique. It is similar to the differential technique except that the transmitter and receiver have been reversed. Instead of illuminating with two beams, only one is used, and scattered light is collected from two directions. A beat signal is observed when the two scattered light beams,

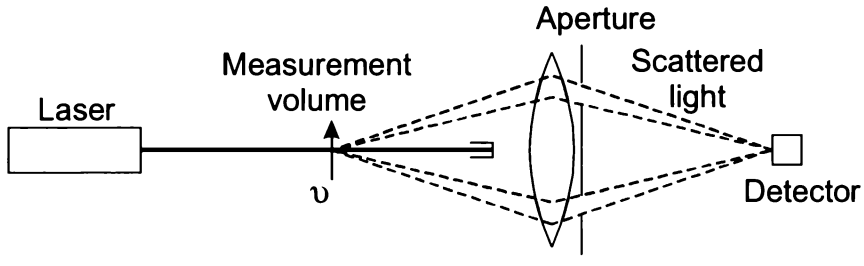

Figure 2.11 – Optical arrangement for dual scatter type LDV

one of which is shifted up in frequency and the other down, are combined on the detector.

In this technique, the angle of illumination has no affect on the detected Doppler signal, but the angle of detection does. Hence, the aperture size also affects spectral width of the Doppler signal, as it does for the reference beam technique.

2.2.2.3. Multi-component measurements

The reference beam technique is sensitive to velocity components in the direction of propagation of the measurement beam. Conversely, both the differential and dual scatter techniques measure the component normal to the (average) angle of illumination (for the differential technique) or detection (for the dual scatter technique). In some situations, it is advantageous to measure more than one velocity component simultaneously.

The measurement of two velocity components, in both directions normal to the illumination angle, is usually achieved by establishing two interference patterns perpendicular to each other. Each pattern produces a Doppler signal for one component.

Nakatani et al. (1984) describe a differential technique that illuminates with two sets of two beams. The two sets have orthogonal polarisations, which generate two interference patterns distinguished by polarisation. The collection optics employ polarising beam splitters to allow detection of the two beat signals independently.

Czarske and Müller (1996) present an approach that illuminates from three directions, each with a different offset frequency. When the scattered light is collected and mixing occurs, velocity components in three directions, separated by frequency, can be decoded.

Another not so common approach is to illuminate with two different laser wavelengths. The Doppler signals can then be separated with chromatic filters prior to detection (Drain 1980).

The techniques described so far can be applied to the differential Doppler technique. However, the dual scatter technique lends itself to two component detection with the addition of a third detection angle and a second photo-detector. This is not commonly used, probably because a significantly better signal-to-noise ratio can be achieved with the differential technique.

If measurement of three velocity components is required, either the differential or dual scatter techniques must be combined with the reference beam technique to determine the component in the direction of illumination.

2.2.2.4. Pedestal removal

It is common for a Doppler signal to have a DC offset level, called a pedestal, caused by background light, high level reference beam illumination, or scattering from more than one particle. It is also common for two burst signals, scattered from two separate particles in a flow, to have a phase difference of π. When detected, these signals will cancel causing a signal drop-out.

The DC level can be removed by high-pass filtering, but there is a more sophisticated technique used to combat this problem called 'pedestal removal'. In this system, two signals are generated with a phase difference of π in a similar fashion to two-phase detection as described above. These signals are then differenced electronically, cancelling any background DC level and significantly enhancing the amplitude of the Doppler signal.

2.3. Atmospheric Doppler lidar

The research presented in this thesis relates specifically to Doppler Lidar, which is the name given to the application of laser velocimetry techniques for wind speed measurement. In the past, the differential Doppler technique has been proposed as a configuration to measure wind speed. Although it is possible to obtain a better signal-to-noise ratio with this technique, it only allows the measurement of wind speed at one spatial location. A modified reference beam technique, which utilises a pulsed measurement beam, has emerged as a more versatile and appropriate optical arrangement.

2.3.1. A typical pulsed Doppler lidar

Pulsed Doppler lidar, as illustrated in Figure 2.12, is a reference beam configuration that utilises a pulsed measurement beam and a CW reference beam. This allows measurements at multiple ranges along the direction of propagation. The distance travelled by the laser pulse is, of course, a function of the time since departure, and therefore scattered light received by the lidar at a specific time can be related to a particular distance.

Because the measurement laser is pulsed, and scattered light returns continuously (as long as the measurement pulse propagates through scattering media) a second CW, local oscillator (LO), laser is required with which to mix the collected light. It is not uncommon for a lidar to be used to measure wind speeds at distances in excess of 10 km, which means the LO must remain coherent with the transmitted pulse over very long pathlength differences. In practice this means a single frequency laser must be used, and a portion of the LO laser must be diverted as an injection locking beam for the pulsed laser. An AOM is often used to apply a frequency offset to the injection beam before it is directed into the slave pulsed laser.

As illustrated in Figure 2.12, the transmitted and received light is arranged coaxially, which means they travel along the same path and use the same optics. This is not always the case but does offer the advantages of high

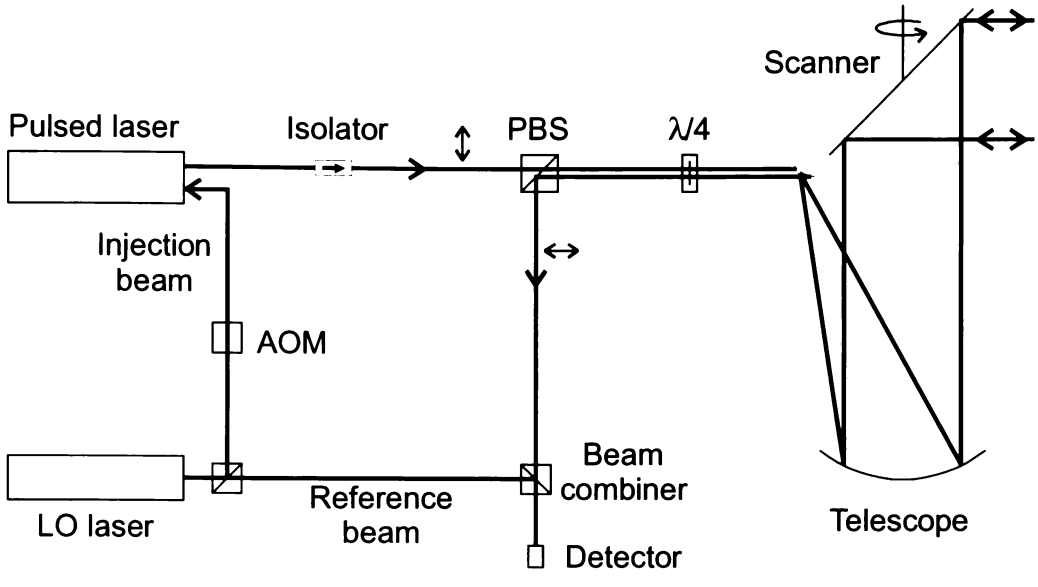

Figure 2.12 – A typical pulsed Doppler lidar optical arrangement

efficiency overlap of illumination and collection volumes. To overcome the problem of separating the transmitted and received beams, which are directed through the same optics, the transmitted beam is linearly polarised and passed through a polarising beam splitter (PBS) to the telescope. A quarter-wave plate is used to convert the transmitted beam to circular polarisation, which, upon scattering in the atmosphere, is largely maintained. When the received beam is passed back through the same quarter-wave plate, it is converted to linear polarisation orthogonal to the transmitted beam, causing the PBS to deflect it towards the receiving optics rather than towards the transmitting laser. A Faraday isolator is used to protect the laser from back reflections from the optics and the atmosphere.

Optical mixing of the reference beam and the received light is performed in a similar fashion to the LDV techniques described above. The main difference is the low light levels received from atmospheric scattering.

A telescope arrangement is used to collect enough light for accurate detection, and in the case of a co-axial transmitter, to direct the transmitted light into the atmosphere. In addition, rotating mirrors provide the ability to "scan" across the atmosphere allowing measurements at different angles and the ability to compile a three-dimensional profile of wind velocities.

2.3.2. Light sources for lidar

Mocker and Wagener (1994) summarise the aspects that need to be considered when selecting a laser source for a lidar system. These include:

- Atmospheric properties such as scattering efficiencies and attenuation of the measurement beam and scattered light.
- Laser physics including laser efficiency, coherence length, output power, pulse length, and the lifetime of the equipment.
- Eye safety, for wavelengths less than 1.2-1.4 μm, is of particular importance.
- Detection equipment's quantum efficiency, heterodyne performance and frequency response.

Initially CO_2 lasers, operating at wavelengths around 10 μm, were the primary choice for lidar transmitter sources mainly because they are capable of delivering the required power and remain coherent over long distances. One example is presented by Sroga et al. (1994), who used pulse energies in the order of 1 J and pulse lengths of around 3 μs.

More recently, diode pumped solid state lasers operating at wavelengths in the region of 1 and 2 μm have been used. In addition to the obvious size and power consumption advantages, solid state lasers use less expensive optics and detectors, and have better spatial resolution for the same velocity resolution (Henderson et al. 1993). The main disadvantage is that they are less eye-safe.

Kavaya et al. (1989) have implemented a lidar using a Nd:YAG laser operating at 1.064 μm with pulse energies of 5 mJ to 8 mJ and pulse lengths of 0.5 μs to 1 μs. Another example using a Cr,Tm,Ho:YAG laser at 2 μm wavelength, with pulse energies of 50 mJ and pulse lengths of 150 ns, was demonstrated by Henderson et al. (1993).

Lidar systems have also been demonstrated at 532 nm by Fischer et al. (1995), and at 1540 nm by Spinhirne et al. (1997).

2.3.3. Atmospheric scattering

Intuitively, it may not seem possible for light to be scattered from the atmosphere. However, a most vivid demonstration is visible to the naked eye on an overcast day when beams of light can be seen as the sun breaks through small gaps in the clouds. Of course, the light seen is that fraction which is scattered by the atmosphere and is visible only because of the absence of equal quantities of background scattering.

There are two elastic mechanisms (where the scattered light is not changed in wavelength) responsible for atmospheric scattering. One from air molecules described by Rayleigh theory and evident only at shorter, blue and ultra-violet wavelengths. The other mechanism is scattering from larger aerosol particles such as dust and pollen suspended in the atmosphere. In general Mie theory is used to describe aerosol scattering. However, this is only an approximation as Mie theory considers scattering from spheres, and aerosols are not always spherical.

Inelastic scattering, such as Raman scattering when there is a wavelength change as the incident light is absorbed and re-emitted, is also apparent in the atmosphere. For velocity measurements, inelastic scattering is not considered, because it provides no additional information, and the scattered intensities are three orders of magnitude less than the molecular scattering (Singh 1997).

For applications near the earth's surface, where aerosols are abundant, aerosol scattering lidars are the most common choice. This is because aerosol scattering returns a larger signal at the more convenient longer wavelengths. Also, signals from aerosol scattering have a considerably narrower spectral width than those obtained from molecular scattering systems which are susceptible to thermal broadening (McGill and Spinhirne 1998). In the upper atmosphere however, there are few aerosols, and molecular scatter based systems are often more appropriate.

The ratio of illumination to that backscatter intensity for a given illuminated volume is called the 'backscatter coefficient', and is represented by the symbol β with the units $m^{-1}sr^{-1}$. This is sometimes split into its molecular (Rayliegh) β_R and aerosol (Mie) β_M components. In order to calculate the received light intensity, the illumination intensity must be multiplied by the solid angle of illumination and collection, the length of the emitted pulse (defining the illuminated, and visible volume), and the backscatter coefficient.

A more rigorous approach considers the efficiency of the optical components (including the overlap of transmitting and receiving optics) and the attenuation over the return pathlength. Such an analysis is not included here, but can be found by studying the lidar equation given by Singh (1997), or for the case of multiple scattering events, that given by Bissonnette (1996).

Aerosol backscatter coefficients vary dramatically with physical location, time, and are also wavelength dependent. At altitudes above the mid-troposphere (approximately 5 km), a strong seasonal dependence is evident (Tratt and Menzies 1994). Several surveys have been conducted to measure the backscatter coefficients, including those reported by Tratt and Menzies (1994), Spinhirne et al. (1997), Menzies and Tratt (1994), and Gras and Jones (1989).

From this data we have compiled a generalisation of backscatter coefficients. Figure 2.13 illustrates this approximation as backscatter versus altitude versus wavelength, but deviations from this approximation of at least one order of magnitude are highly probable.

2.3.4. Detection and processing system

The major problem in constructing lidar systems is receiving and detecting the very small atmospheric backscatter signals. Very sensitive photodetectors or photomultiplier tubes are required, along with significant post detection signal processing, before a reliable wind measurement can be produced.

2.3.4.1. Expected signals

While the measurement laser pulse propagates through the atmosphere, and scattered light returns to the lidar, the optical mixing process produces a Doppler signal. Unlike an LDV system, which can produce burst type signals, lidar Doppler signals are generally continuous, varying in amplitude and frequency as long as there are sufficient scatterers, and hence amplitude of received light.

In general, wind speeds do not exceed 100 m/s producing a maximum Doppler signal of 10 MHz at 10 μm wavelengths (Stoyanov et al. 1995), or 200 MHz at 500 nm wavelengths. Often, however, a lidar will be moving in relation to the atmosphere, producing a frequency offset in addition to any

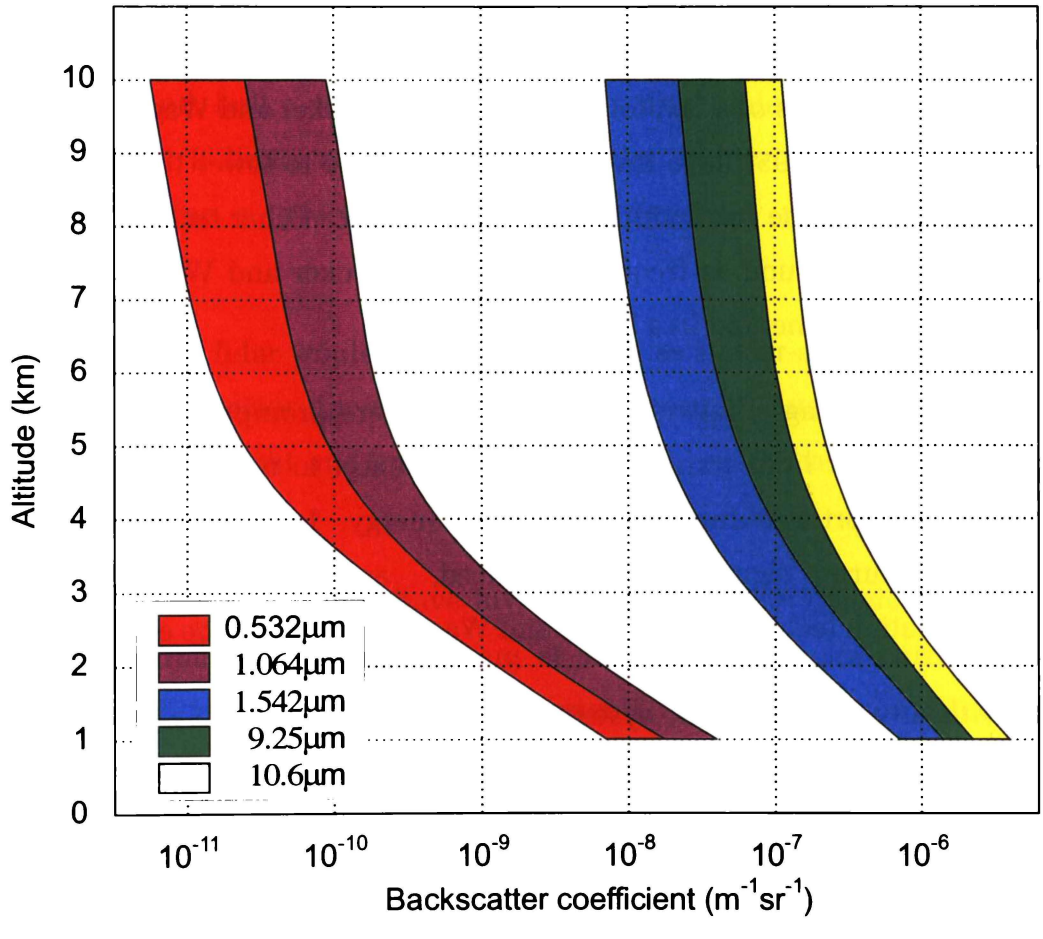

Figure 2.13 – Approximate backscatter coefficients for 0.532, 1.064, 1.542, 9.25 and 10.6 μm wavelengths. Data compiled from results presented by Tratt and Menzies (1994), Spinhirne et al. (1997), Menzies and Tratt (1994), and Gras and Jones (1989).

offset applied by the optical techniques. At 10 μm this falls in the range 80-100 MHz for airborne systems and is in the order of 1.3 GHz for orbiting platforms (Stoyanov et al. 1995).

2.3.4.2. Sampling and processing

Investigation of atmospheric characteristics requires the recording of measurements for post processing. For this reason, lidar systems often employ a personal computer (PC) for data collection.

Doppler signals can either be sampled directly after being detected, or processed electronically first. Direct sampling provides a larger bandwidth, but is not so common as high sampling and data rates are required. It is more common to quadrature demodulate which produces two signals at a lower, more manageable, frequency with a $\pi/2$ phase difference (Kavaya et al. 1989, Sroga et al. 1994). These quadrature signals are then digitally processed by means of a fast fourier transform (Mocker and Wagener 1994). Stoyanov et al. (1995) have investigated techniques to lower the data rates while preserving the bandwidth of direct sampling. Other techniques used in LDV systems, such as frequency tracking (Mocker and Wagener 1994), can also be implemented in a lidar system.

Low backscattering efficiencies of the atmosphere prompt the use of high power lasers for lidar transmitters. In an attempt to maintain eye-safety, there is an effort to reduce the transmitted energy. In such systems, much weaker return signals are produced, and photon-counting or autocorrelation techniques (Mocker and Wagener 1994) can be employed.

As with any measurement system, the signal-to-noise (S/N) ratio of the incoming signal affects the accuracy of measurement. In lidar systems, the detected signal is the convolution of the spectrum of the transmitted pulse, the spectrum arising from atmospheric motion, and the spectrum of the local oscillator (Rye and Hardesty 1993a, 1993b). As a result, the sources of noise include the transmitting and local oscillator lasers, as well as the detector and processing electronics.

Due to the small return signals, it is common to have a poor S/N ratio which results in a large uncertainty in the velocity estimate. Usually this is combated by an accumulation of processed readings, as opposed to averaging raw data prior to processing, (Rye and Hardesty 1993a). Various studies have been undertaken to find ways of quantifying and improving S/N ratios (DiMarzio and Linderg 1992) and of discovering how to optimise lidar performance (Frehlich 1990, Rye and Hardesty 1997b, and Zhao et al. 1990a and 1990b).

The availability of high speed computers has made more sophisticated post processing techniques such as pseudo-random noise modulation and de-convolution feasible (Stoyanov et al. 2000).

2.3.5. Applications and commercialisation

Lidar systems are now in common use for atmospheric research but are still too large and bulky to be considered for any widespread commercial application. If lidars could be made smaller, lighter, and cheaper, they would become a practical every-day commercial product for many applications.

In particular, a lidar would be most beneficial as a clear-air turbulence and wind shear detector in aircraft and at airports. Another application requiring low weight and small lidar systems is space based atmospheric monitoring systems.

Although some researchers have investigated the use of coherent lidar for clear air turbulence detection (Targ et al. 1996), there are currently no commercially available early warning systems. The main reason is the cost and size of the injection-locked laser system, described in the previous chapter, of the currently favoured lidar design. Retrofitting one aircraft with a lidar unit has been estimated at a cost of between US$100,000 and US$200,000 (Tatterson 1998).

Chapter 3
Low coherence lidar

The commercial viability of lidar systems is hindered by the high cost and large size, due mainly to the injection-locked laser systems currently used. The first part of this thesis describes a new method of obtaining velocity measurements over long ranges without the use of single frequency lasers. Instead, smaller, cheaper, low coherence sources can be used allowing the construction of lidar systems for commercial application at a viable price. This chapter describes this novel concept and presents results of experiments, proving the validity of the design.

3.1. Introduction

In order to reduce the cost and size of lidar systems, we have investigated replacing the long coherence injection-locked lasers with a cheaper, smaller and less complex low coherence source. This source must still be pulsed in order to obtain multiple measurements over distance, which causes two major problems. Firstly, there is no CW reference laser with which to beat the scattered light, and secondly, even if there were a reference, it would not be coherent over the large measurement distances required.

3.2. Low coherence lidar concept

To date, lidar systems have used single frequency lasers to ensure that collected light, which may have travelled several tens of kilometres, remains coherent with the reference beam, which has travelled only a metre or two. In order to use a low coherence laser source, the problem of preserving coherence over a long path difference must be overcome.

Hence, the pathlength difference must not be allowed to exceed the coherence length of the laser. This means the reference beam must also travel a long distance, equivalent to that of the measurement beam.

The low coherence lidar concept (Dorrington et al. 1999) generates the measurement and reference beams simultaneously by splitting the transmitted light and storing a portion in a ring resonator storage loop until the scattered light returns. While the measurement beam propagates out through the atmosphere, is scattered, and returns to the lidar, the reference beam propagates multiple times through the storage resonator. Consequently, the measurement beam and the reference beam have travelled equivalent distances before being mixed. Hence, the two beams remain coherent even though they have travelled a distance much larger than the laser's coherence length, within limits imposed by the storage resonator.

This storage loop is designed to have a round trip time slightly longer than the pulse length, so that a single input pulse will generate an output pulse train that exponentially decays in amplitude at a rate dependent on the input/output coupling ratio of the resonator. Since the pulse length is shorter than the storage loop round trip length, the stored pulse never

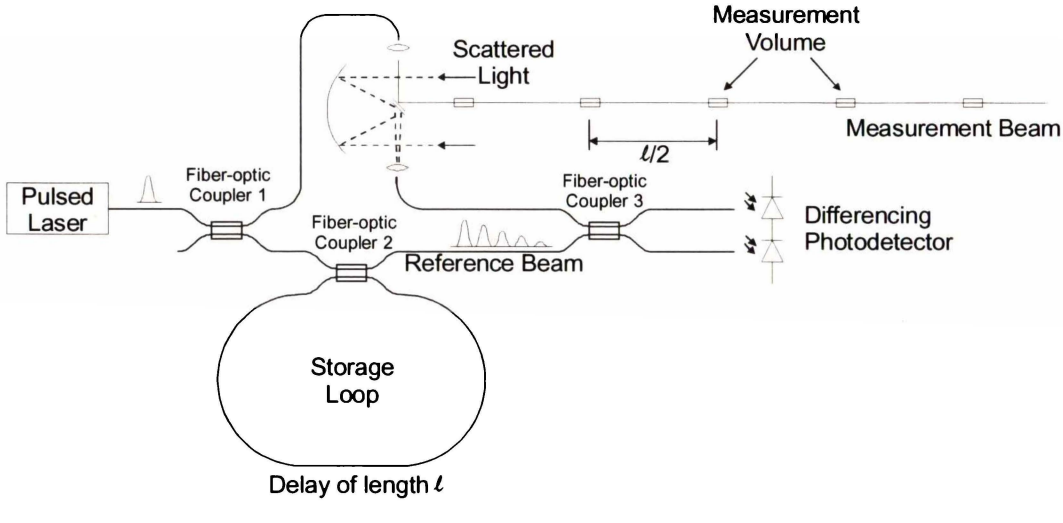

Figure 3.1 – Low coherence lidar concept in a fibre optic implementation, showing a fibre optic based storage loop, and measurement volumes separated by half of the length of the storage loop.

encounters or interferes with itself.

Figure 3.1 illustrates the concept of a low-coherence lidar system utilizing a fibre optic reference beam storage loop. Fibre-optic coupler 1 splits the light from the pulsed laser source, with the majority of its power as the measurement beam, and the remainder as the reference beam. The measurement beam is then directed into the atmosphere through a telescope as with any other type of lidar. This telescope also collects the scattered, Doppler shifted light and directs it to fibre-optic coupler 3, where it is mixed with the reference beam output of the storage loop.

The reference beam output of coupler 1 is connected to the storage loop consisting of coupler 2 and a delay fibre. When entering coupler 2 for the first time, a fraction of the light pulse is split off and becomes the stored reference beam in the loop, while the rest is passed to coupler 3. There is now a laser pulse inside the loop, and each time it passes coupler 2, a fraction is split off and passed to coupler 3, while the rest remains stored in the loop. The resulting reference beam is an exponentially decaying pulse train.

Each pulse in the reference beam has travelled a discrete distance equal to a multiple of the storage loop length. Hence, for each reference beam pulse there is a corresponding discrete distance along the measurement beam path from which scattered light is coherent. As a result, mixing occurs and measurements can be made for light scattered from an illuminated measurement volume defined by the diameter or solid angle of the emitted measurement beam, and either the pulse length or the coherence length of the laser. The distance between these measurement volumes is half of the optical pathlength of the storage loop, as the measurement beam must travel out and back again.

Theoretical pulse train outputs, from the storage loop, are illustrated in Figure 3.2. The two traces illustrate two different input/output coupling ratios. A higher initial output can be achieved with a 50/50 coupler, but the peak intensity decays quite rapidly. The 90/10 coupler provides a

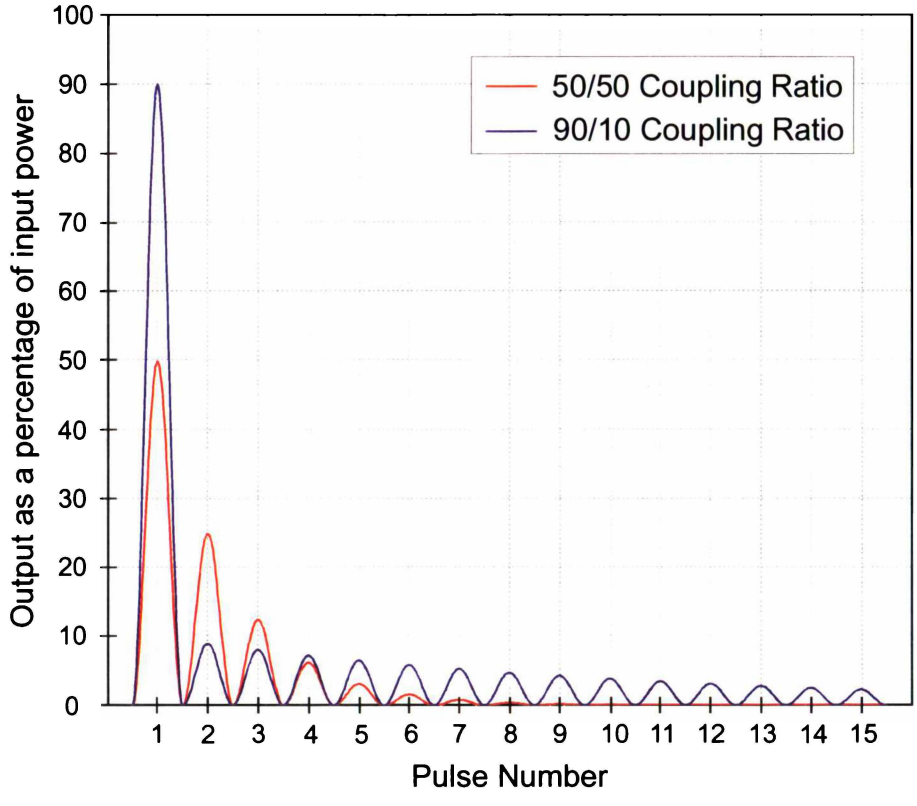

Figure 3.2 – Theoretical pulse train output from a storage loop, as a percentage of input power, for two coupling ratios.

much more stable output level, and hence can store a pulse for longer, but to obtain a similar output level to the 50/50 coupler a larger initial input level is required.

Ideally, a large number of output pulses would ensure a long measurement range, but to achieve a large number of pulses a very small coupling ratio is necessary. However, this in turn means a very small fraction of the input light will be coupled into the storage loop during the initial pulse. Hence, there is a trade-off between the number of pulses obtainable and the input power requirements.

3.3. Experimental validation

In order to prove that the low coherence lidar and storage loop concepts are viable, a validation experiment was performed. The experiment was designed to show two main mechanisms in action:

- The storage of a reference pulse and generation of a reference beam pulse train.

- Optical mixing of a Doppler shifted measurement beam with stored reference pulses, and the capability of measuring the velocity of a target at ranges greater then the coherence length of the laser.

In this section, the optical set up and measurement equipment used in this experiment are described, the results obtained are presented, and their implications are discussed.

3.3.1. Optical arrangement

A schematic diagram illustrating the experimental set-up of the validation experiment is shown in Figure 3.3, and a photograph is shown in Figure 3.4. The system measures the velocity of a rotating mirror with two separate methods.

The first method utilises the low coherence lidar concept. A measurement beam is reflected off the moving mirror and is optically mixed with a

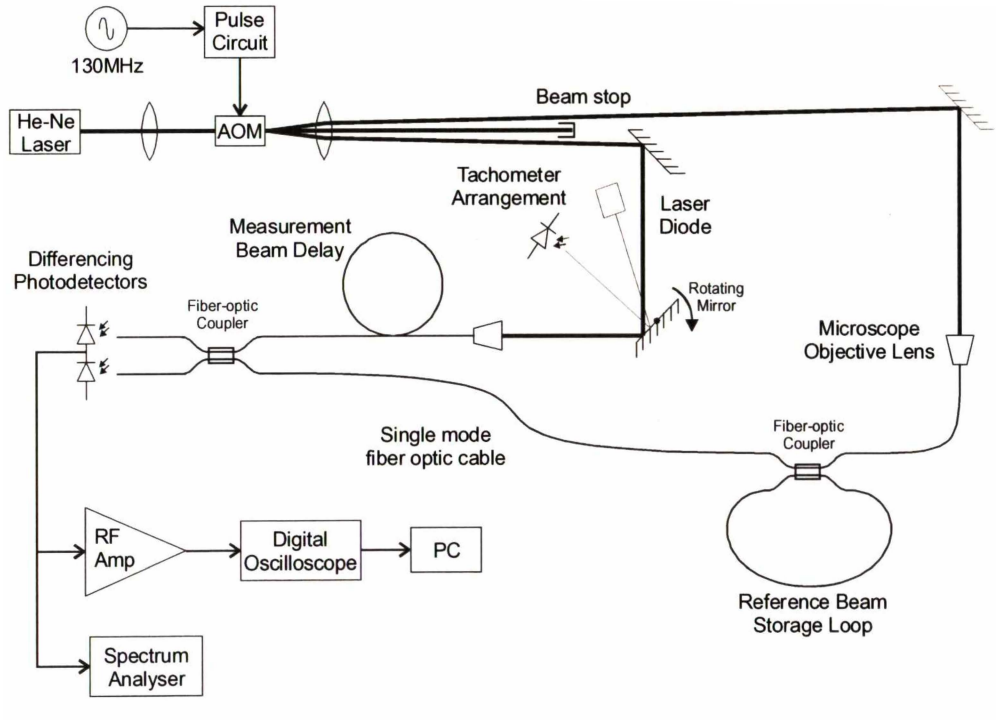

Figure 3.3 – Optical arrangement of the low coherence lidar concept validation experiment.

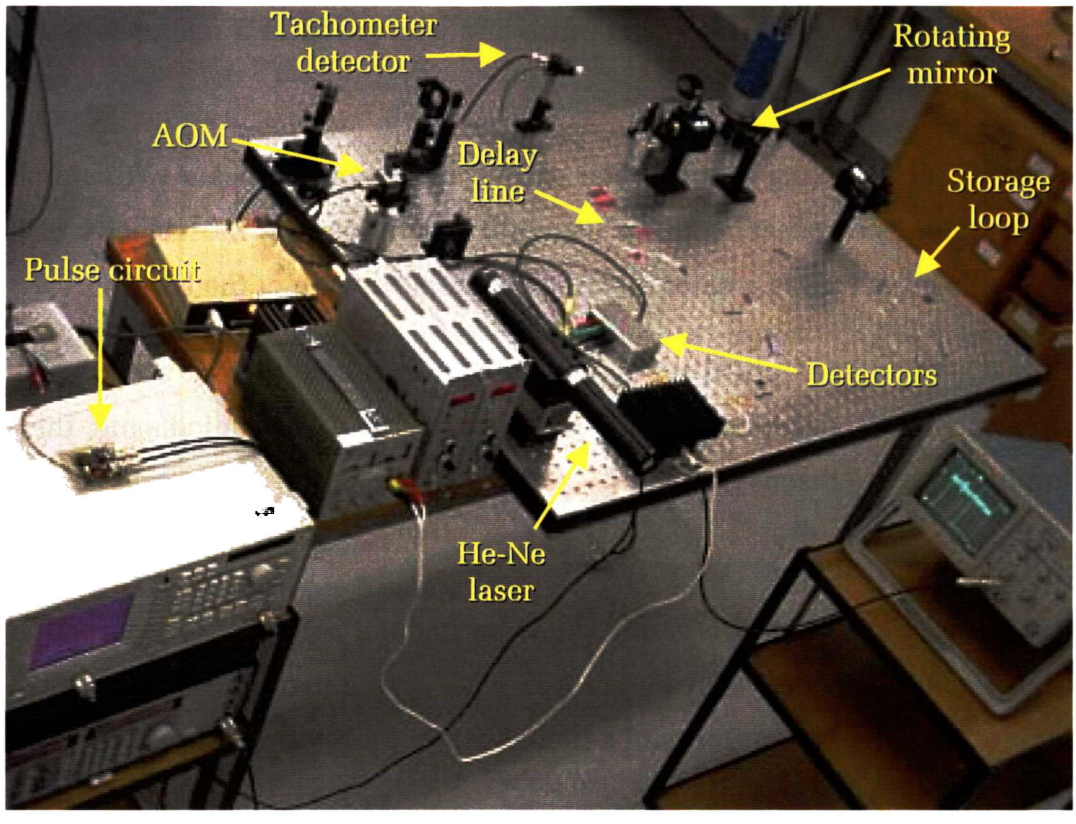

Figure 3.4 – Photograph of storage loop experiment.

reference beam pulse train (generated by the storage loop). This is done at several ranges by adjusting the length of the measurement beam delay fibre, simulating return signals from several measurement volumes. The second method monitors the rotation speed of the mirror using a tachometer arrangement, and then the velocity is calculated. In the following sections, these measurements are presented and compared to evaluate the storage loop concept.

3.3.1.1. Reference and measurement beam generation

A CW He-Ne laser (1125, Uniphase, San Joes USA) was used as the light source, which was passed through an acousto-optic modulator, AOM, (EFL-M120, Matsushita) which was excited by 30 ns pulses of a 130 MHz signal at a power level of 15 dBm. Arranged in a Raman-Nath configuration, this produced pulses on both first order diffracted beams. One was used as the reference beam and the other as the measurement beam. Using both the up-shifted and down-shifted diffracted beams conveniently provided a 260 MHz offset on the Doppler signals during optical mixing.

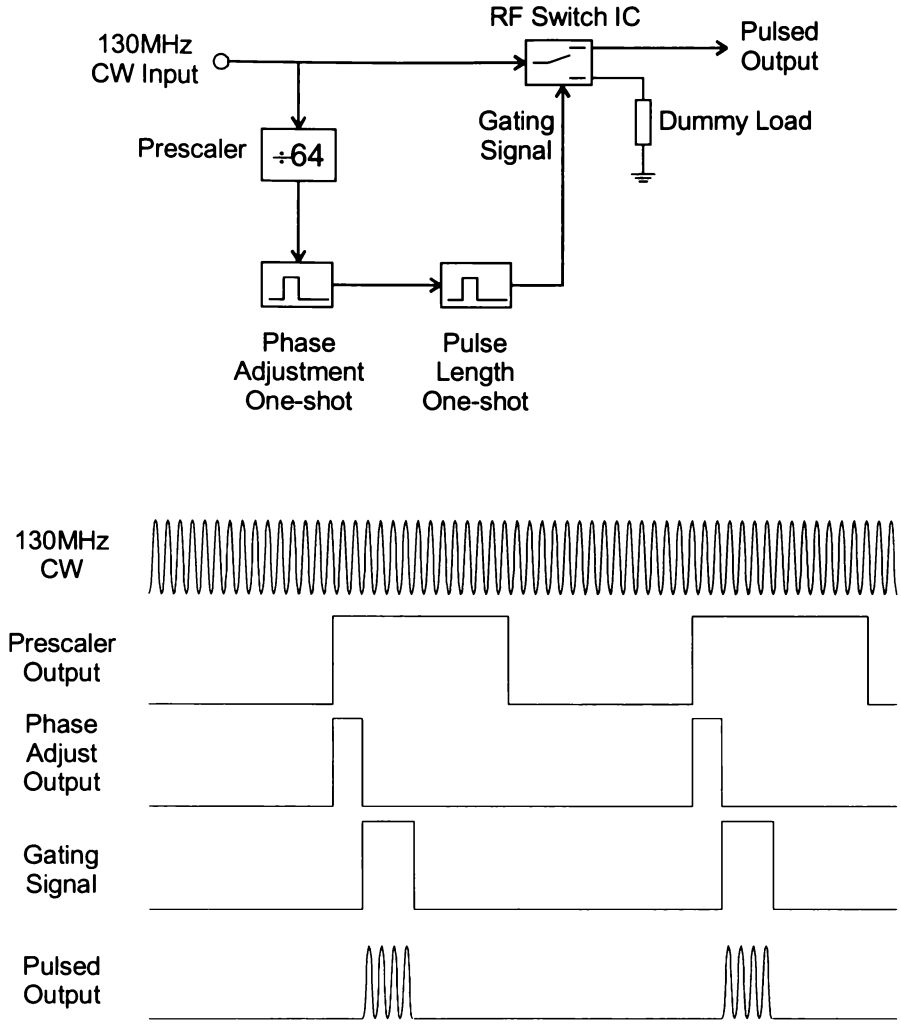

Figure 3.5 – Block diagram of phase-locked pulse generation circuit and circuit timing.

The AOM drive signal was generated by a RF signal generator (SMY-02, Rohde & Schwarz, Munich Germany) producing a 130 MHz CW output with no modulation, and was then passed though a custom designed pulsing circuit (refer Figure 3.5). The full circuit diagram and PCB layout are included in Appendix VI.

The circuit employed a single pole double throw RF switching IC to turn the 130 MHz driving signal on and off. The switch was controlled by a series of Schmitt trigger 'very high speed CMOS' (VHC) NAND gates arranged as a variable delay and a variable one-shot, which was driven by the output of a divide by 64 prescaler. The input of the prescaler was connected to the 130 MHz CW input signal, which had the effect of phase

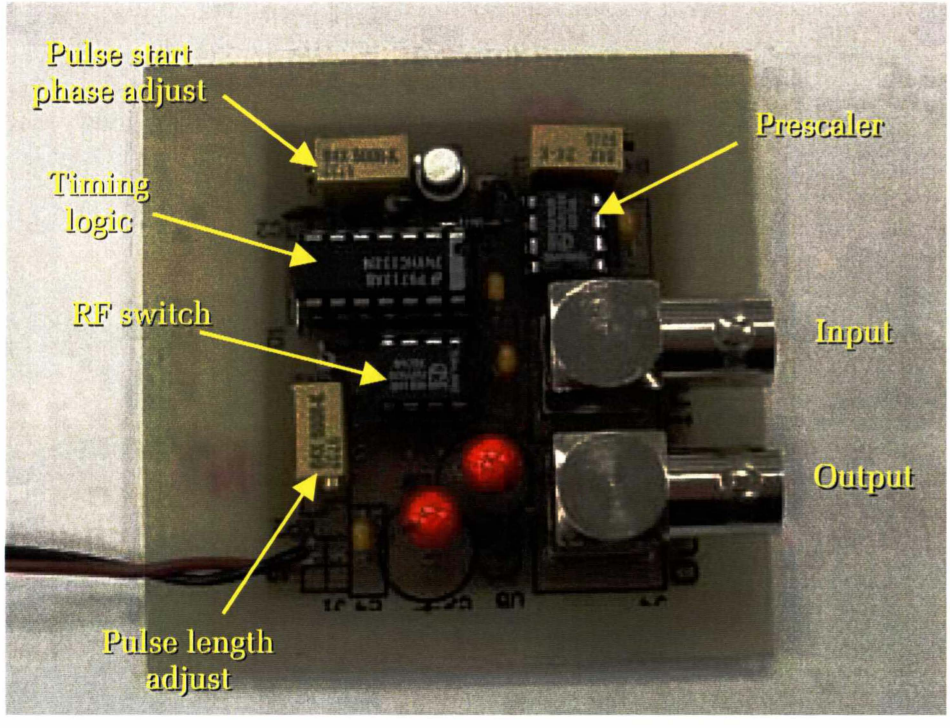

Figure 3.6 – Photograph of phase-locked pulse circuit.

locking the pulsing circuit to the input signal. As a result, the starting phase of the AOM driving signal was always the same and could be controlled. This produces a considerably more stable light pulse compared to what is achieved with non-phase-locking pulsing circuits. A block diagram of this circuit and a theoretical timing diagram are shown in Figure 3.5, and a photograph of the board in Figure 3.6.

Diffraction and frequency shifting in acousto-optic devices is caused by acoustic waves passing through the path of an incident laser beam. As a result, the optical rise time is a function of the speed of sound (in the crystalline medium) and the diameter of the laser beam. In order to achieve the fastest possible rise time, the laser beam was focused onto the AOM producing the smallest possible beam diameter. An example of a measured output pulse from the AOM is shown in Figure 3.7.

The conversion efficiency of the available AOM was poor, with the first order diffracted beams containing about 200 μW each for an input of almost 7 mW. Further loss was introduced by coupling the free space beam into the single mode fibre.

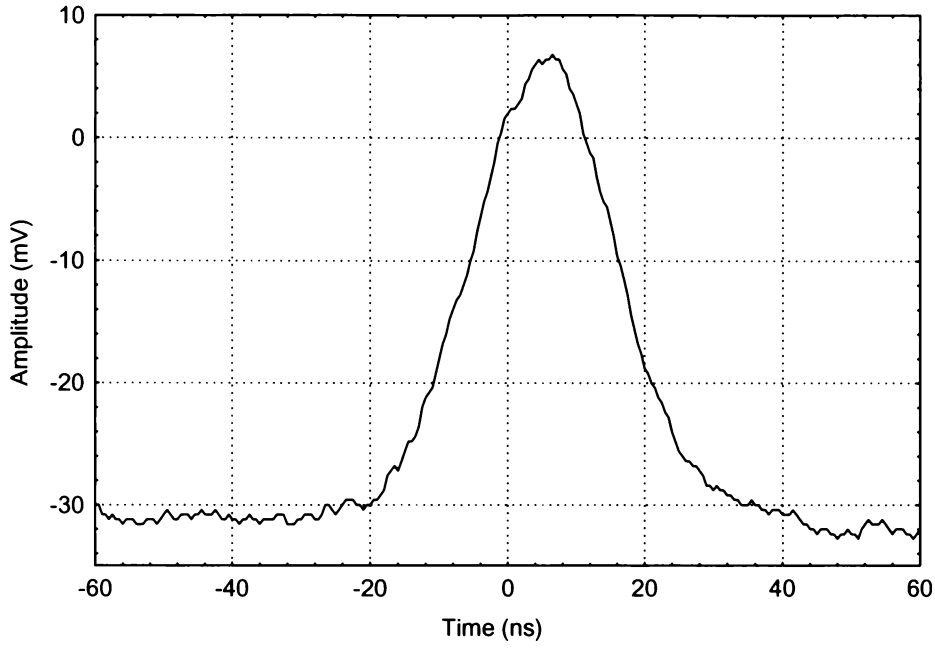

Figure 3.7 – A typical optical pulse output from the AOM

3.3.1.2. Storage loop

The reference beam was focused by a microscope objective lens into one of the input ports of a 2x2 fused fibre optic coupler. The other input fibre was connected to one of the output fibres via a delay line, forming the storage loop resonator with a total optical pathlength of 12.4 m. This equates to a time delay of approximately 41 ns. A 50/50 coupler (Gould Fibre Optics, Chudleigh United Kingdom) was used to generate the pulse train, providing 4 or 5 viable pulses before it decayed to unusable levels. Figure 3.8 shows a generated pulse train output. For our purposes this was sufficient, and preferable to a slower decay pulse train of low amplitude (as discussed above).

3.3.1.3. Doppler shift

Before being imaged into the fibre delay line, the measurement beam was Doppler shifted by a rotating mirror. Measurements were taken at ten different rotation speeds, simulating ten different wind speeds. These results were then compared to the mirror velocities obtained by a tachometer. This tachometer consisted of a laser diode and photodetector

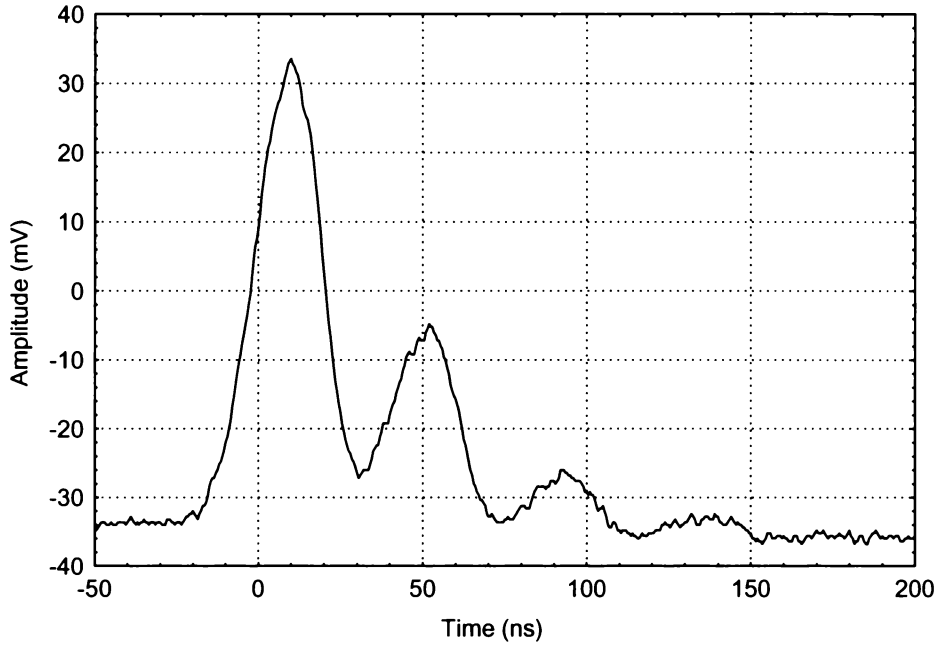

Figure 3.8 – A typical pulse train output from the storage loop.

connected to a frequency counter and was used to monitor the rotation rate of the mirror (illustrated in Figure 3.3).

To record results at several distances, additional fibre length was added to the measurement beam delay. These lengths were carefully arranged to coincide the arrival of the measurement pulse with one of the reference pulses. The first four reference pulses, representing the first four measurement volumes, had sufficient amplitude to be detected, and hence velocity measurements were acquired at each of these distances in turn.

3.3.1.4. Optical mixing and detection

The measurement and reference beams were optically mixed in a 2x2 (Gould Fibre Optics, Chudleigh United Kingdom) fibre coupler producing the signal illustrated in Figure 3.9. In addition to the desired beat signal imposed on pulse 2, unwanted beating is evident in pulses 3 onwards. In the next section, the storage loop is simulated in software and the unwanted beat signals are explained as beating between reflections off fibre ends and joins.

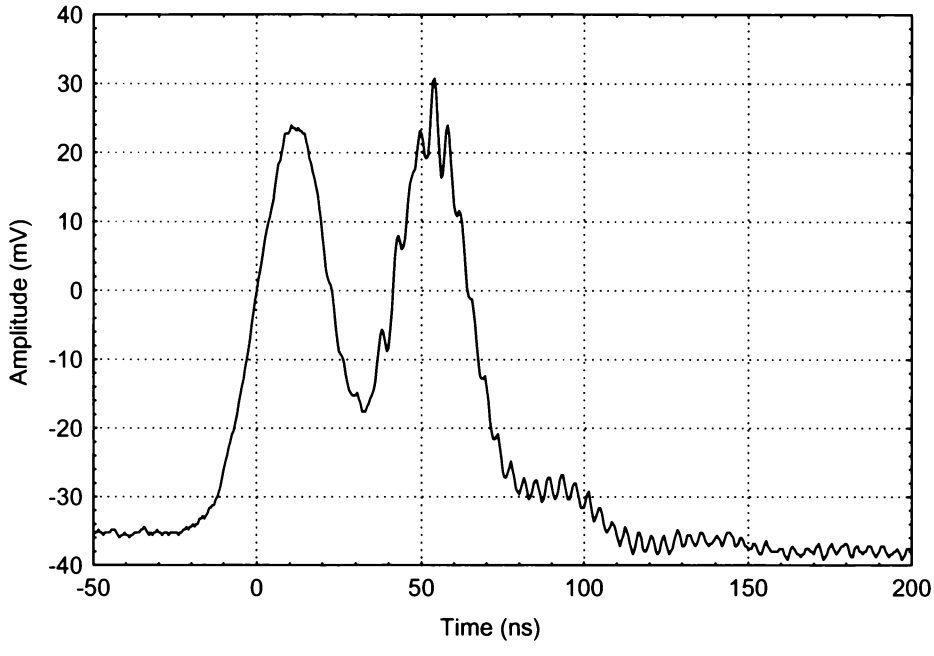

Figure 3.9 – A typical mixed Doppler signal. The measurement pulse is arranged to interfere with the second reference pulse.

The outputs of the couplers were each connected to one of the single-mode fibre-coupled Si avalanche photodiodes (C30902E, EG&G, Quebec Canada) biased with 200 V. The diodes were arranged in the differencing configuration illustrated in Figure 3.10, which is also known as a two-port balanced coherent receiver (Agrawal 1997). In this configuration, any optical signal common to both detectors, including background light, is cancelled. The photocurrent common to both detectors passes directly from the positive to the negative power supply rails, resulting in no output current in the load.

Optical mixing that occurs in an appropriately matched 2x2 fused coupler produces an output that is π out-of-phase. This phenomenon can be explained as conservation of energy. If the coupler's inputs are in such a phase that the interference causes no light to appear at one output, then all of the light must be present at the other output.

Because the "Doppler bursts" at the outputs of the coupler are π out-of-phase, the photodiodes conduct alternately, causing an alternating positive and negative output signal. As a result the Doppler burst signal amplitude

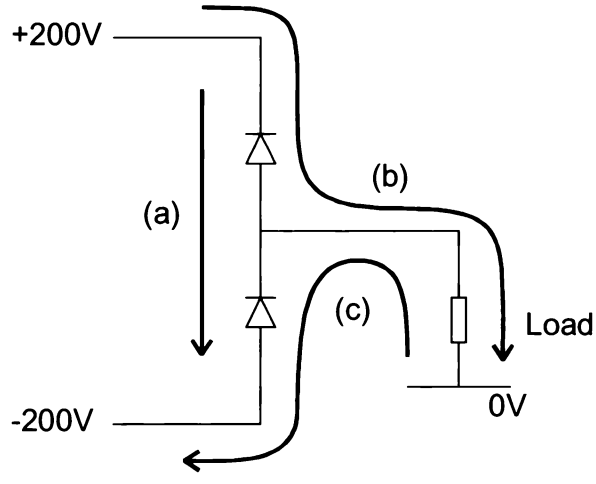

Figure 3.10 – Simplified differiental detector circuit. (a) Incident light common to both photo-diodes generates the same photo-current that passes from the positive supply to the negative supply with no output load current. (b) Light on the positive detector side only causes a positive load current. (c) Light on the negative detector side causes a negative load current.

doubles. Figure 3.11 shows the signal from the differencing detectors, which in this case do not have exactly matching gains causing some residual pulse shape.

The signals from the photodetectors were amplified by a radio frequency amplifier (ZHL-1-2W/BNC, Minicircuits, Brooklyn USA) before being sampled at 1 giga samples per second and recorded by a digital oscilloscope (TDS 360, Tektronix, Beaverton USA) and downloaded to a PC.

3.3.2. Simulation

A simulation of the fibre optic arrangement was performed in software. This involved modelling the fibre section of the experimental set-up and calculating the signal for both directions of propagation at all discontinuities along the fibre. These discontinuities include terminations, joins, and couplers. A schematic of the simulation is shown in Figure 3.12 illustrating each simulation point and the delay times between them. The Matlab code of this simulation is included in Appendix II.

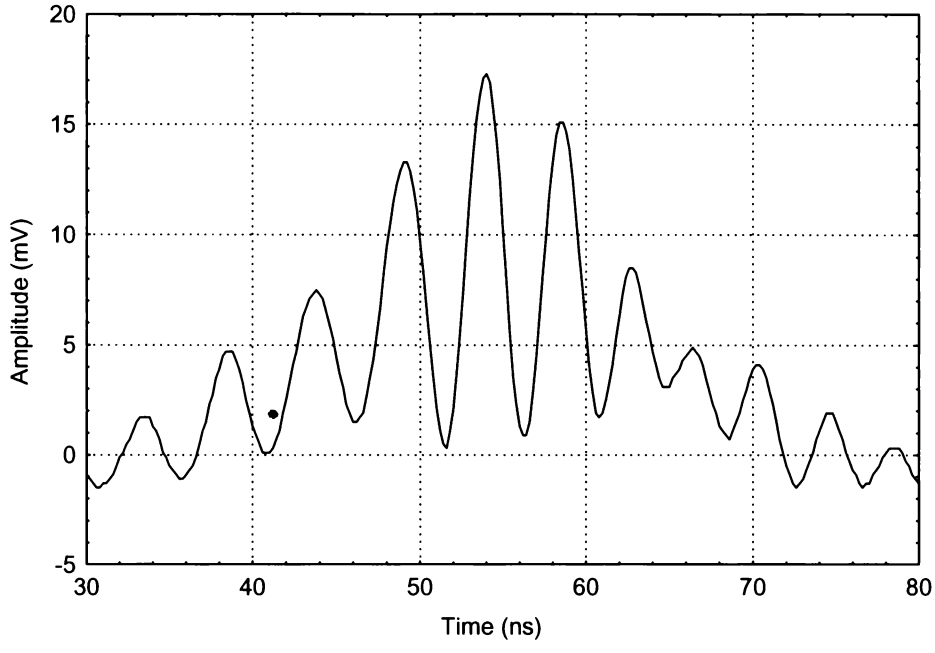

Figure 3.11 – A typical Doppler burst signal output from the differencing detectors.

The input signal was generated as a complex wave function multiplied by a pulse envelope

$$U(t)=\begin{cases}\exp(j2\pi ft)\sin\left(\pi\dfrac{t}{\tau}\right) & 0\le t\le\tau\\ 0 & \text{otherwise}\end{cases} \qquad 3.1$$

where f is the frequency of the wave, t is time and τ is the total pulse width.

To reduce computation time, the frequencies were chosen to be 12.5 GHz, and 12.76 GHz for the up-shifted and down-shifted inputs, respectively. This allowed a manageable sample time of 10 ps, but maintained an adequate frequency difference between the wave and the beat signals of more than an order of magnitude. The total pulse width, τ, was set to 60 ns, providing a full width half maximum of approximately 30 ns.

At each fibre join the intensity of the transmitted wave was reduced to 98%, and 1% of the incident intensity was reflected with a π phase change. This is more than an order of magnitude greater than the specifications for the fibre connectors, however, it is still a reasonable approximation,

considering some connectors have been reused a number of times. This reuse leads to a loss of index matching gel, responsible for suppressing reflections, and could also compromise alignment. In addition, the input and detector terminations were assumed to be a 4% reflector, and the couplers a 50% intensity split.

To derive the detected signal the magnitude squared of the complex wave was calculated. This was done for all nodes allowing each one to be monitored as if a non-intrusive detector were placed in every location. It is interesting to investigate the measurement and reference beam inputs to the final beam combining coupler, shown in Figure 3.13.

The measurement beam (node 37) exhibits some small beat signals from reference pulses that have been reflected off the detector or fibre joins. Both the output signals along with the difference between them (processed electronically in the experiment) is shown in Figure 3.14. Also evident here is the presence of unwanted beat signals due to the mixing of reflections.

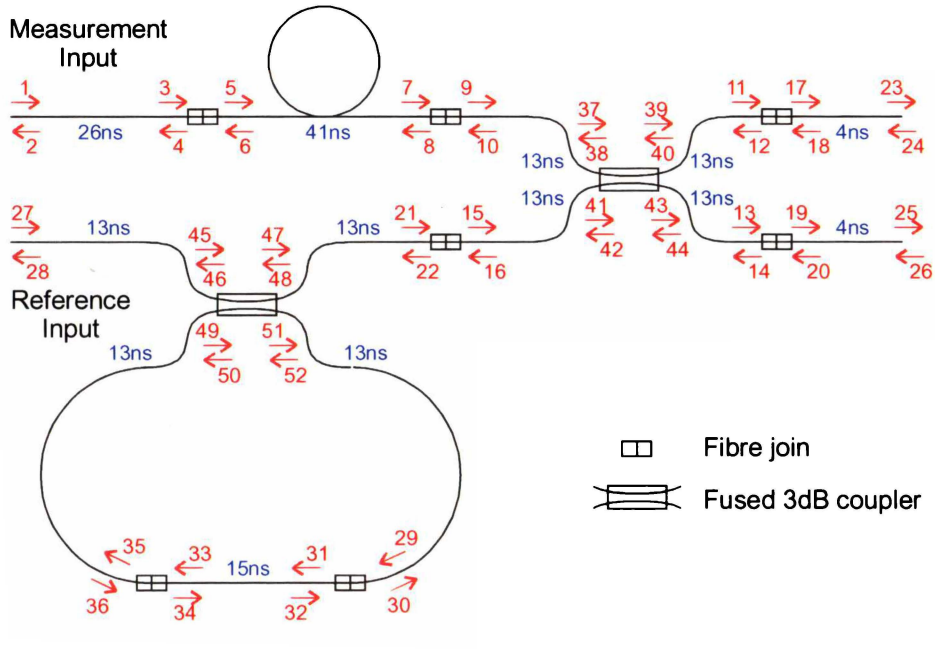

Figure 3.12 – Schematic diagram of storage loop experiment simulation. Simulation nodes are shown in red, and delays in blue.

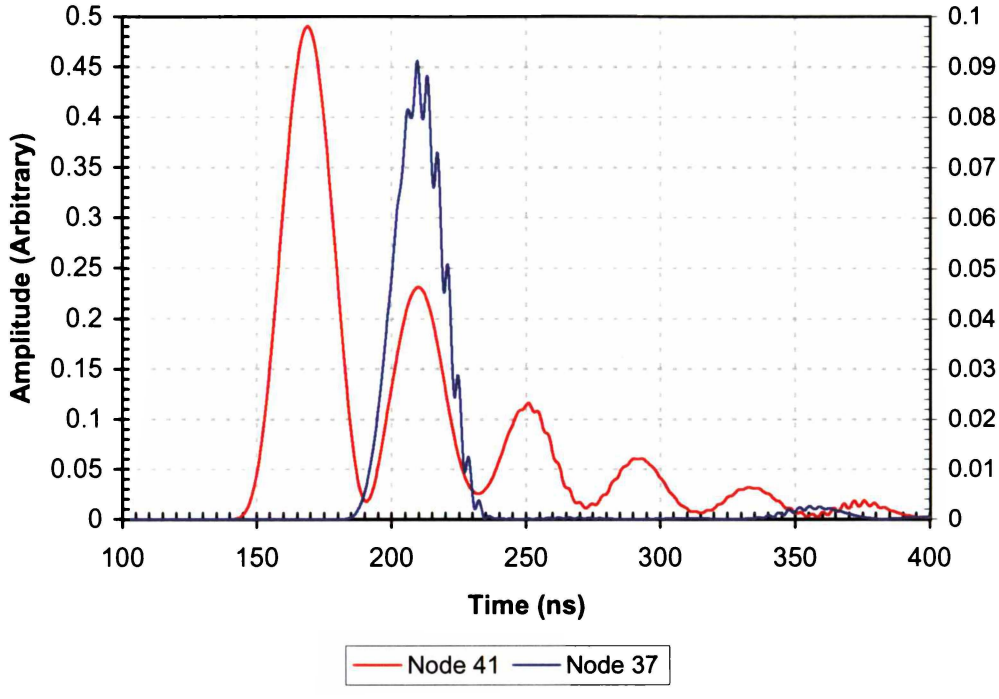

Figure 3.13 – Simulated signals entering the beam combining coupler of the storage loop. The reference pulse train is shown in red, and the measurement pulse in blue.

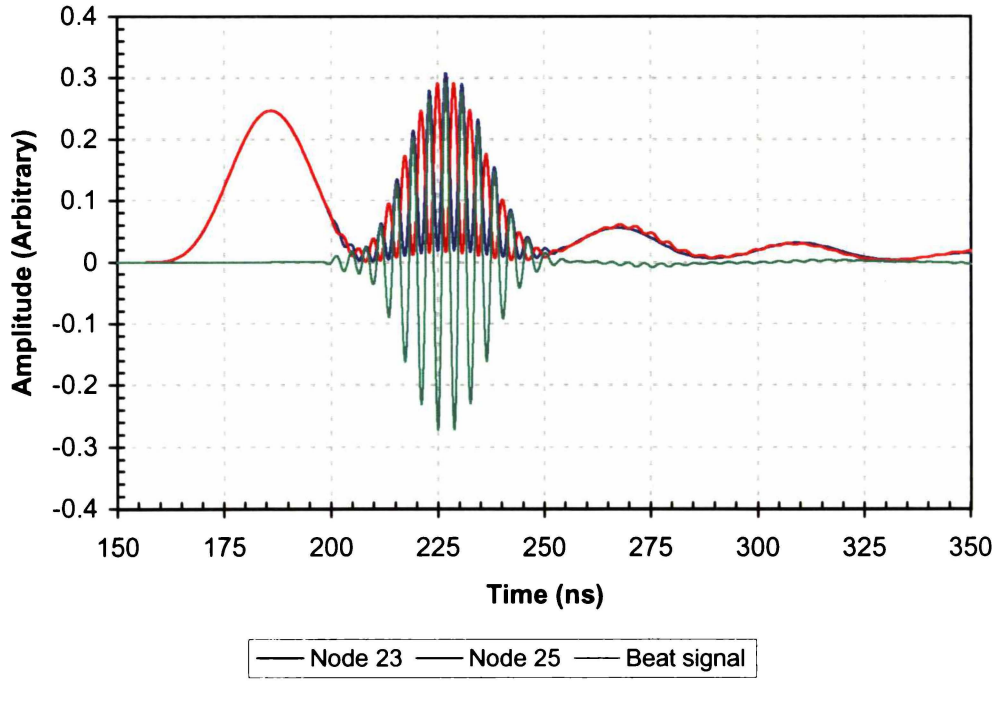

Figure 3.14 – Simulated output of storage loop. The two detected signals are shown in red and blue, and the difference shown in green.

There are two main differences between the signals in the simulation and those obtained from the experiment. Firstly, the desired beat signal is smaller in amplitude in the experiment, indicating the mixing was not as efficient as anticipated. This is partly because the fibre couplers are not exactly a 50/50 split, as per the simulation.

Secondly, there are differences in the temporal position and amplitude of the unwanted beat signals. If time were taken to characterise each fibre end, join and coupler, more accurate results could be obtained. Despite this, the purpose of determining the origin of the unwanted beat signals is still served.

3.3.3. Signal processing

The data, collected experimentally, was processed in software (Matlab, The MathWorks Inc, Natick USA) to find the frequency of the Doppler burst and to calculate the velocity of the mirror by performing a peak search on the fast Fourier transformed (FFT) data. A flow diagram illustrating the processing algorithm is shown in Figure 3.15, and the code used is included in Appendix III. Because of the burst nature of the signal and low number of data points (64), very poor accuracy was obtained initially. At a sampling rate of 1 Gsps, the FFT has a Nyquest upper frequency limit of 500 MHz. For 64 time domain points the FFT produces 32 frequency domain points, providing a frequency resolution of 15.625 MHz. At a laser wavelength of 633 nm, the minimum desired velocity resolution of 0.1 m/s corresponds to 158 kHz, which is two orders of magnitude below the FFT frequency resolution.

Two steps were taken to increase resolution in the frequency domain:

- The time base on the oscilloscope was increased to provide 5×10^9 points per second. The actual sampling rate could not be increased beyond 1×10^9 samples per second, which means the upper frequency limit remains at 500 MHz, but the oscilloscope inserts interpolated points causing the Nyquest frequency to be increased to 2.5 GHz.

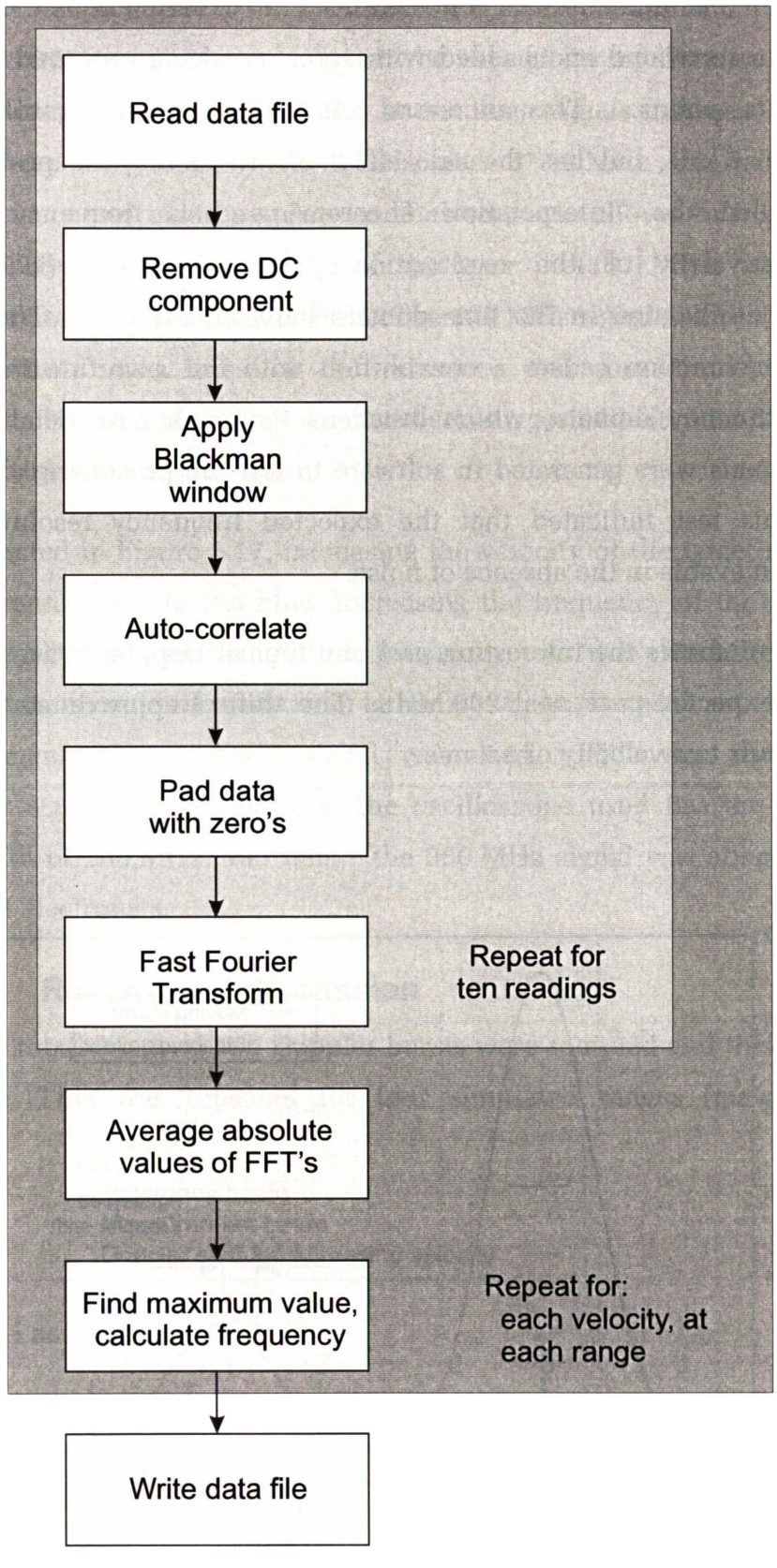

Figure 3.15 – Flow diagram of the processing algorithm used to determine velocity from experimentally recorded Doppler data.

- The time domain data, collected from the experiment by the PC, was autocorrelated and padded with zeros, resulting in a total of 16384 data points. This increased the FFT frequency resolution to 152.6 kHz, but has the side effect of broadening the peaks. It is called the "Interpolation Theorem" and is frequency domain equivalent of the explanation given by James (1995). A multiplication in the time domain between the burst signal and a *rect* function causes a convolution with the *sync* function in the frequency domain, which broadens the peak. Artificial Doppler signals were generated in software to test the processing algorithm. This test indicated that the expected frequency resolution was achievable in the absence of noise.

Figure 3.16 shows the interesting part of a typical Doppler burst spectrum and the expected peak near 260 MHz. The shift of approximately 9 MHz corresponds to a velocity of 5.7 m/s.

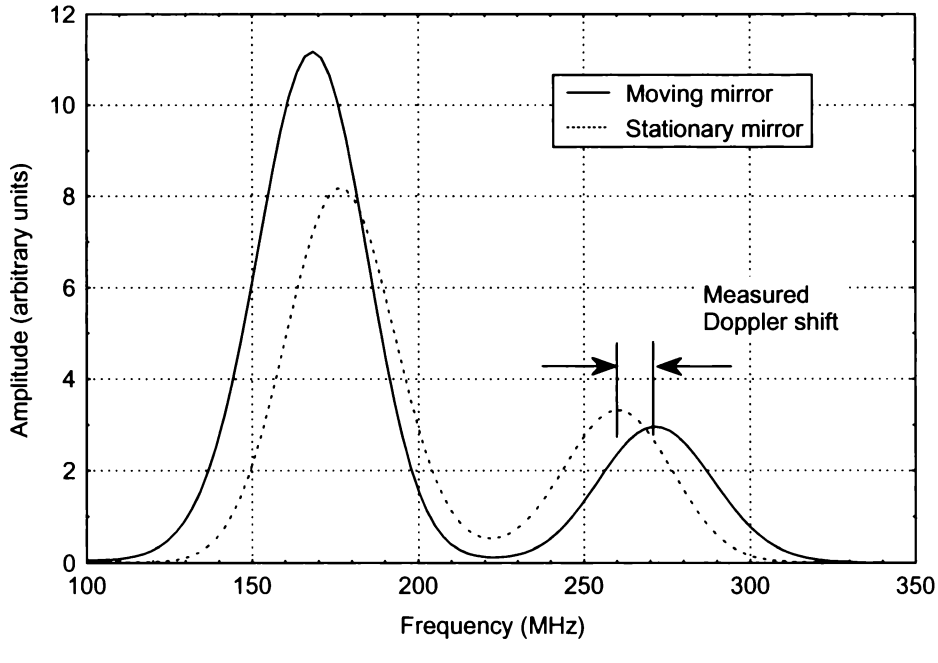

Figure 3.16 – The interesting section of a Doppler burst spectrum obtained from the experiment. The solid line indicates a Doppler shifted signal, and the broken line a non-shifted signal.

Also apparent in Figure 3.16 is a second unexpected Doppler signal based around 176 MHz. This was found to be caused by interference between different longitudinal modes of the laser. Beat signals between the these modes were measured at 436.9 MHz and 873.8 MHz (limited by the detector response) using a spectrum analyser. As shown in Figure 3.17, this indicates the mode spacing of the laser is 436.9 MHz, which was confirmed from the laser's datasheet. The 176 MHz signal is a beat between the different mode lines of the reference and measurement beams. Generating beat signals in this way has been suggested before by Biselli and Werner (1989).

As illustrated in Figure 3.17, increasing the velocity of the target shifts the measurement beam to the blue, increasing the frequency of the 260 MHz beat signal, and reducing the frequency of the 176 MHz signal. Measurements could be made from either signal, but for each set of velocity measurements the strongest signal was used. This was usually the 176 MHz signal, in part because the oscilloscope used has an analogue bandwidth of 200 MHz, and hence the 260 MHz signal was attenuated by the input electronics.

3.3.4. Results and discussion

For each rotation speed, ten Doppler bursts were sampled and their spectra averaged. This was repeated for four simulated ranges (measurement

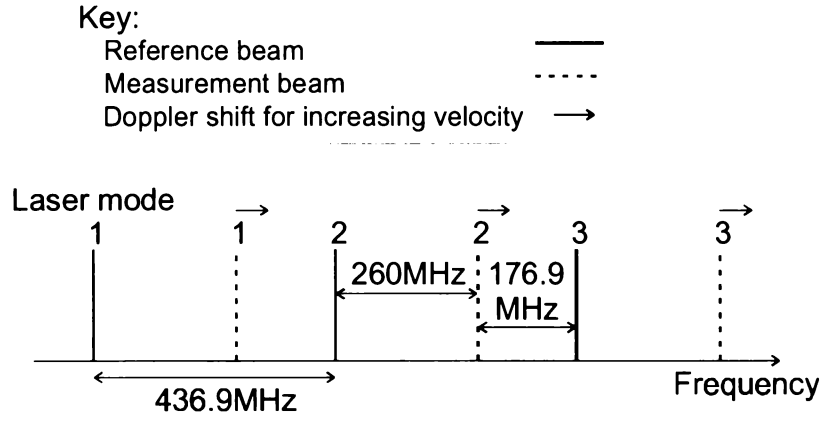

Figure 3.17 – Reference and measurement beam longitudinal laser modes, showing the generation of the 260 MHz and 176 MHz beat signals.

distances) by increasing the length of the measurement beam fibre optic delay. The conversion from frequency shift to velocity was performed with a simplified version of expression 2.19

$$\Delta\nu = \frac{2\upsilon\cos\theta}{\lambda} \qquad 3.2$$

where $\Delta\nu$ is frequency change, υ is velocity and θ is half the angle between the incident and reflected beams (Drain 1980). This holds when the direction of motion is along the bisector of the illumination and detection angles only.

3.3.4.1. Recorded data

Figure 3.18 shows a plot of measured versus actual velocity (determined with the tachometer). The motor speed drifted during the measurement period resulting in an uncertainty of approximately $\pm 0.05\ ms^{-1}$ on the tachometer measured velocity. Errors due to the measurement equipment combine to an uncertainty of $\pm 0.2\ ms^{-1}$ in the Doppler burst processed velocity estimation. To maintain clarity in the graph, these errors have

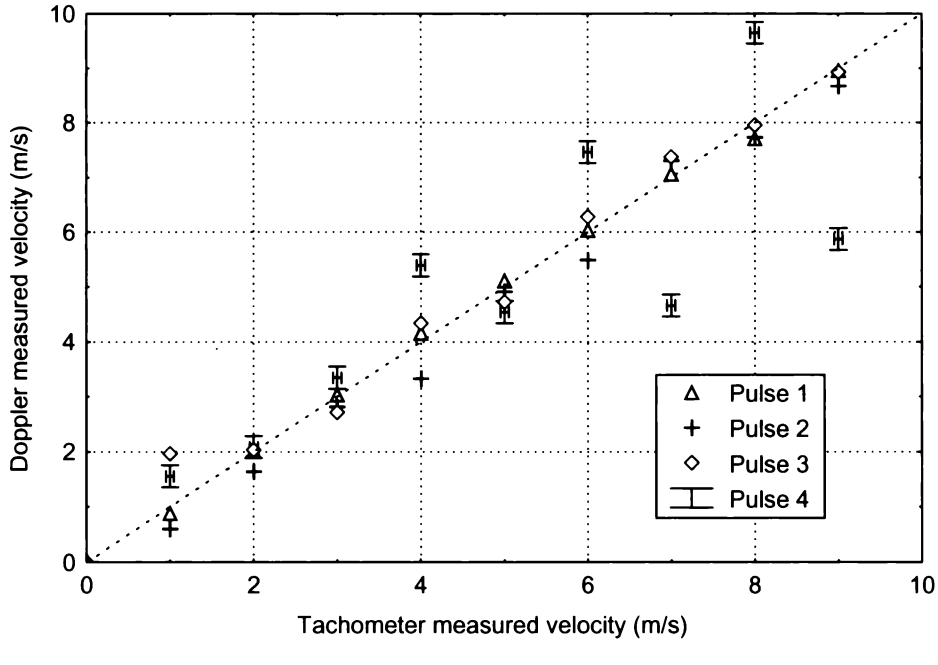

Figure 3.18 – Validation experiment results for the first four reference pulses, showing Doppler measured velocity vs tachometer measured velocity.

been illustrated in the Pulse 4 results only. Not included are errors due to noise or signal processing.

The signal-to-noise ratio of the beat signals from the first reference pulse was calculated to be 13 dB. The measured results from the first pulse correlate with the actual velocity within the measurement errors. Because of the 3 dB coupler in the storage loop, each successive reference pulse halves in intensity. As a result, the amplitude of each Doppler burst drops by approximately 3 dB for each reference pulse with variations due to fibre optic joins.

The effects of the declining S/N ratio can be seen on the graph; the correlation between the measured and actual velocities deteriorates for later pulses. Reference pulse number 4 is only just detectable above the noise (as shown in Figure 3.8), and the results for this pulse are unreliable. This confirms that the beat signal is produced by the mechanism being investigated (optical mixing of the stored reference pulses and the delayed measurement pulse). As previously mentioned, the limitation to four reference pulses is due to the experimental set up and could be improved in the future.

3.3.4.2. Theoretical storage limit

Dispersion is an effect that causes broadening of pulses in a fibre optic cable, because the material has different refractive indices at different wavelengths. A pulse contains a spread of frequencies centred on the laser's wavelength, with the shorter pulses having broader spectrums. Each frequency component experiences a different refractive index in the cable and therefore travels at a different velocity causing the received pulse to be spread in time.

With respect to a He-Ne laser and single mode fibres, the main cause of pulse broadening is group velocity dispersion. This is because a He-Ne laser has a very narrow line width, which is negligible when compared to the Fourier limited spectral width of the pulse envelope (Yariv 1996). The

pulse width after travelling a specified distance in a fibre can be calculated, for a Gaussian temporal envelope, as

$$\tau(L)=\tau_0\sqrt{1+\left(\frac{1.47DL\lambda^2}{\tau_0^2}\right)^2} \qquad 3.3$$

where τ_0 is the initial pulse width in picoseconds, D is the dispersion coefficient, L is the distance travelled in kilometres and λ is the wavelength in micrometers.

The dispersion coefficient of a typical optical fibre at a wavelength of 633 nm is approximately 200 ps·km^{-1}·nm^{-1}.(Saleh and Teich 1991). If we consider a 1% increase in pulse width to be the limit of acceptability, then the pulse can be stored for up to 1×10^6 km. This extreme distance is due to the very narrow line width of the He-Ne laser, and also to the relatively slow pulse length. A pulse 100 times narrower (300 ps) for example, would have an approximate range limit of only 100 km. In practice, other effects such as attenuation would limit the range, but from a dispersion point of view there is no practical limit to pulse storage.

If a different low coherence laser was used, for example a 1550 nm laser diode with a line width of 2 nm, the material dispersion become the dominant effect. It can be expressed quantitatively as the temporal width of a input impulse after travelling a length of fibre. This is called the response time, and can be calculated as

$$\sigma_\tau=|D|\sigma L \qquad 3.4$$

where D is the material dispersion coefficient for the centre wavelength, σ is the laser linewidth in nm, and L is the distance travelled in km (Saleh and Teich 1991).

At 1550 nm, the dispersion coefficient of a typical fibre is 17 ps·km^{-1}·nm^{-1}, resulting in a response time of 34 ps·km^{-1}. Therefore, the maximum storage length in this situation is approximately 88 km. This is considerably less

than the distance achievable with a He-Ne laser, but still significantly greater than the operating ranges of most lidar systems.

3.3.4.3. Processing limitations

Our experiment used pulse lengths of approximately 30 ns, which provided Doppler bursts of equivalent times. Compared to other lidar designs, these short pulses provide a high spatial measurement resolution, with the distance between measurement volumes of approximately 6 m. However, because of the short burst, they also provide a challenge when processing the data to determine velocity. The peak search algorithm simply located the frequency in the FFT with the largest amplitude. This is very susceptible to noise because any distortions in the peak shape may cause the highest amplitude to appear off centre. Some additional work is required in the area of signal processing as well as optical design before a high spatial resolution, low coherence lidar can approach the velocity measurement accuracies of current lidar systems. For example, a standard deviation of 0.4 ms^{-1} for a 10 sample average was demonstrated by Korb et al. (1997).

3.3.5. Experimental limitations

There are several limiting factors in this experiment, but as our aim was only to confirm that this technique is viable, we did not require absolute or highly accurate measurements. The limitations were not improved upon because the goal of the experiment was achieved, and even though better results could be obtained, time and equipment restrictions made improvements impractical. The limitations are as follows:

- The accuracy of measured results at low signal-to-noise ratios is relatively poor because minimal effort was directed towards the signal processing.

- The unexpected 176 MHz signal could be suppressed by choosing a different low coherence laser and/or by employing more sophisticated signal processing.

- In our experiment, the offset of 260 MHz was a consequence of using the AOM to pulse the beams. A different offset frequency or pulse system could be used to help suppress unwanted signals.

- The reference pulse decays to an unusable level very quickly because of the 50/50 coupler in the storage loop. We had to use this coupler because of the lack of optical power available as an input to the loop. A higher-powered pulsed laser and/or a more efficient AOM arrangement, combined with a different coupling ratio, could be used to give equivalent pulse intensities with a slower decay.

3.4. Conclusion

We have devised a fibre optic ring resonator system to store a reference pulse and generate a reference pulse train for pulsed Doppler lidar. Simulations have been performed and an experiment constructed to validate the concept. For this experiment, a phase-locked pulsing AOM drive circuit and a differencing avalanche photodetector circuit have been designed and constructed. Doppler burst results were recorded and processed to derive velocity.

In comparison, previous lidar systems (as described in Chapter 2) utilise a second injection-locked laser to generate the reference beam. The application of the storage loop, as presented in this thesis, provides a new method of generating the reference beam by replacing both the transmitting laser and the reference laser with one low coherence source.

Validation experiments have been conducted that measure the velocity of a target by beating reflected light from several simulated distances with a reference beam stored in the resonator. These experiments suggest that a lidar system capable of multiple velocity measurements, in the direction of propagation of the transmitted beam, at ranges much longer than the coherence length of the laser source can be constructed.

Our experiments to date have utilized a He-Ne laser, but this technique should be equally applicable to low cost, low coherence sources such as

high power laser diodes. With further development, this design could reduce the cost and complexity of lidar systems, thereby making them a practical commercial product rather than a limited research tool.

The main problem with the system as it stands is the trade off between the decay of the stored reference pulses, and the storage loop input power required. A significant improvement may be observed if a gain element, such as an erbium doped fibre amplifier (EDFA), were introduced into the storage loop. This would allow the use of high coupling ratios, such as 50/50, because any loss due to coupling to the output can be compensated for by the amplifier. Some work has been done on EDFAs in fibre loops by Harwood (1991) with reference to optical memory devices, and Veen et al. (1998) with reference to communication ring networks, which may be applicable to low coherence lidar.

Further research is required to establish if an EDFA will remain stable, and not break into laser oscillation, and if the reference pulses will remain coherent over a large number of passes through the amplifier.

Chapter 4
Single sideband offset generation

An Acousto-Optic Modulator (AOM) is used in many LDV and lidar systems to generate a frequency offset. This causes a zero velocity reading to correspond to some predefined frequency. Such an offset is useful for direction determination and ease of signal processing.

In addition to the single frequency lasers described in the previous chapter, the AOM is another component that adds to the complexity of lidar and other LDV systems. Eliminating it from the design would help to reduce the cost and size of the lidar systems.

This chapter presents the second part of the research work of this thesis. It describes a new method of generating a frequency offset that does not require the use of an AOM. This method relies on single sideband (SSB) modulation techniques similar to those used for radio communications. The direction discrimination and ease of processing advantages that would normally be obtained with the use of an AOM can now be achieved without the added expense.

4.1. Introduction

As covered in previous chapters, an AOM can be used to shift the frequency of an optical beam up or down the frequency spectrum. This is achieved by passing the light beam through a crystalline medium excited with an acoustic wave. Repeated regions of low and high refractive index are created, forming a diffraction grating. As this grating moves the

diffracted light has a Doppler shift imparted to it in proportion to the frequency of the acoustic wave.

The use of an AOM to generate a frequency offset in LDV and lidar systems is common. Such an offset is useful for determining direction of motion and can assist the Doppler decoding electronics. By shifting the Doppler signal, which is normally centred on DC, up the frequency spectrum where there are significantly more cycles per second, the task of frequency counting or tracking can be performed more easily.

The ability to apply a frequency shift without requiring an AOM and the associated driving electronics could prove very useful in the reduction of cost, size, and complexity of both LDV and lidar systems. Here we present two methods of doing just this, one semi-optical method based on amplitude modulating the laser source in conjunction with simple post processing electronics. The other method utilises fully electronic post processing. Both methods are presented because particular applications may suit the implementation of one method more than the other.

4.2. Single-sideband modulation

Single-sideband modulation is a form of Amplitude Modulation (AM) commonly used in radio frequency applications for conserving bandwidth. Normal AM modulation produces both upper and lower sidebands each carrying the same information. By eliminating one of the sidebands, the information can be conveyed in half the bandwidth, as illustrated in Figure 4.1. In essence, the baseband information is shifted towards the higher end of the RF spectrum.

We have taken the SSB concept as it is applied to RF situations, modified and applied it to an LDV system, in order to generate a frequency shift in the Doppler signal.

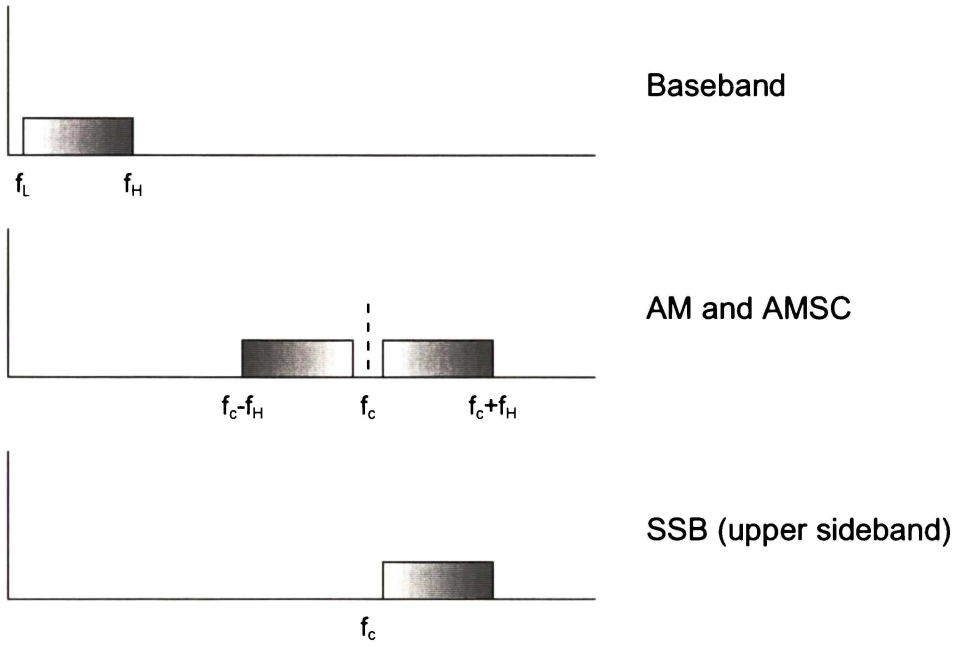

Figure 4.1 – Baseband (information), AM and SSB signals in the frequency domain. For full amplitude modulation (AM) the carrier frequency, broken line f_c, is present, and for suppressed carrier (AMSC) modulation it is absent. With single sideband modulation (SSB), the carrier is never present.

Several methods exist to implement a RF SSB modulator, most of which involve a complicated series of mixing and filtering. In contrast, the "phasing type" method (illustrated in Figure 4.2) is implemented by summing the outputs of two balanced modulators (Zeines 1970). One modulator has the carrier frequency shifted by $\pi/2$ and the other has the baseband signal (or Doppler signal in this case) shifted.

A quadrature modulator is a common circuit in RF communications often used for digital quadrature phase shift keying modulation. Its operation is very similar to an SSB modulator because it utilises two balanced mixers with carrier signals $\pi/2$ out-of-phase. Hence, by the addition of a phase shift on the baseband signal, it can be easily configured as an SSB modulator. Quadrature demodulators operate in a complementary way by converting a modulated RF signal to two baseband signals with the aid of phase shifted carriers.

A balanced modulator is a multiplication circuit, which generates an output that is the analogue product of two inputs. Figure 4.3a shows a

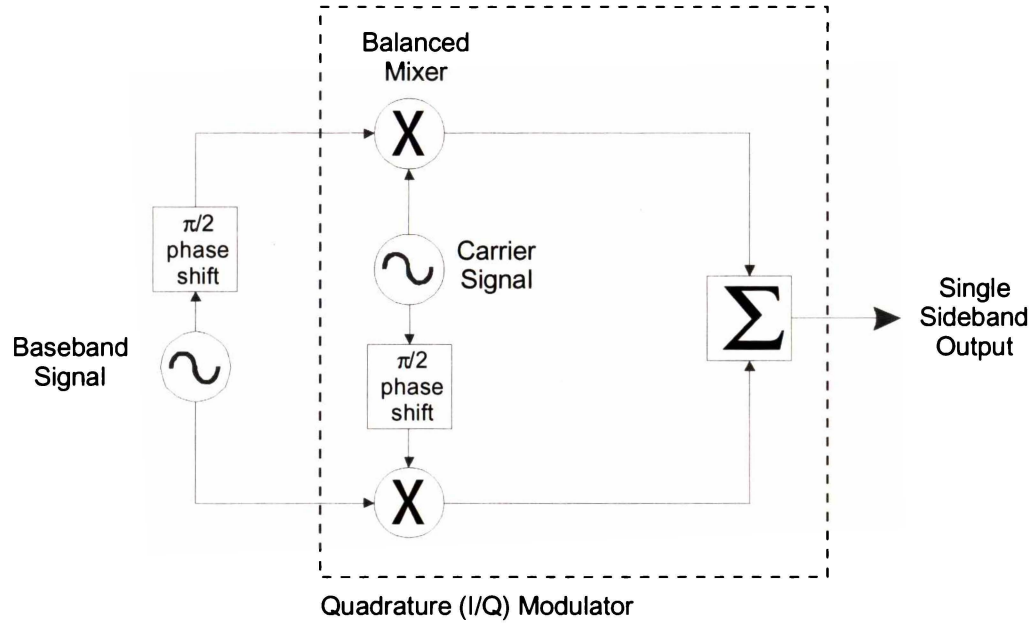

Figure 4.2 – Phasing type single sideband (SSB) modulator, showing the use of a quadrature modulator (containing two balanced modulators) with phase shifted inputs.

modulated signal that is generated by a balanced mixer, and the baseband modulating signal. The product generated is the sum and difference terms in the frequency domain, as illustrated in Figure 4.3b. It is called an Amplitude Modulated Suppressed Carrier (AMSC) signal containing both an upper and lower sideband with no signal at the carrier frequency. If the full description of the signals, including positive and negative frequencies, is considered, multiplication in the time domain corresponds to a convolution in the frequency domain. This is also illustrated in Figure 4.3b, which shows the baseband signal being repositioned and replicated at the positive and negative carrier frequencies (or vice-versa).

The two balanced mixers have either the carrier or baseband signal phase shifted. As a result, either the lower or the upper sideband is out-of-phase between the two mixer outputs, and therefore is cancelled when summed. The other sideband is in-phase, and hence is doubled in amplitude.

To illustrate this operation algebraically consider ω_b as the baseband angular frequency, ω_c as the carrier angular frequency, ϕ is the phase shift and t is time. Then the baseband signal is

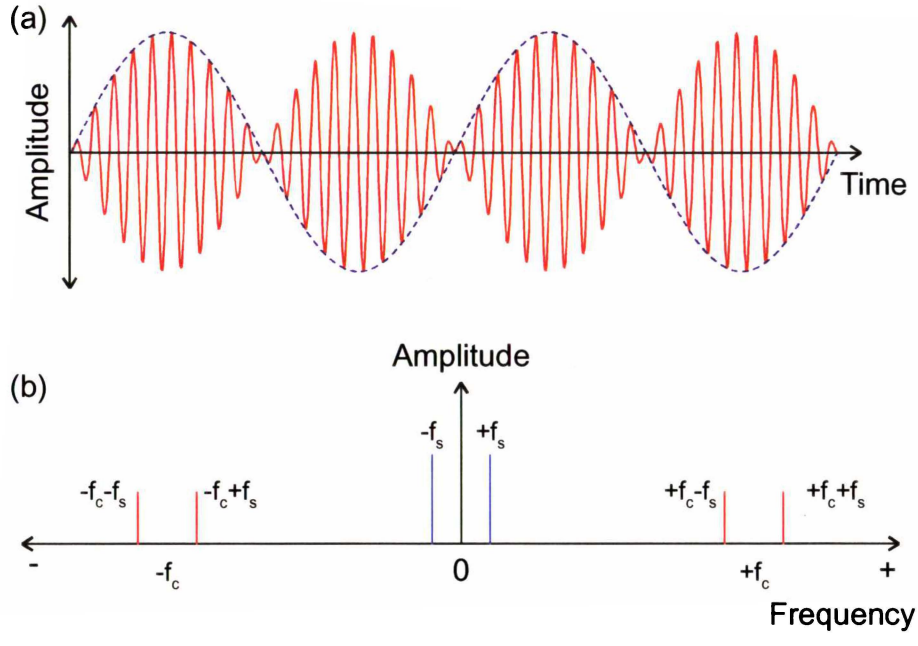

Figure 4.3 – Balanced mixer signal multiplication, in both the time domain (a) and frequency domain (b). The signal frequency is in blue and the modulated result in red.

$$S_b = \sin(\omega_b t + \phi) \tag{4.1}$$

and the carrier signal is

$$S_c = \sin(\omega_c t + \phi) \tag{4.2}$$

Summation of the baseband signal mixed with a phase shifted carrier signal, and a π/2 phase shifted baseband signal mixed with the carrier (as shown in Figure 4.2) produces the SSB signal

$$\begin{aligned} SSB &= \sin(\omega_b t)\cdot\sin\left(\omega_c t + \frac{\pi}{2}\right) + \sin\left(\omega_b t + \frac{\pi}{2}\right)\cdot\sin(\omega_c t) \\ &= \frac{1}{2}\left[\sin(\omega_b t + \omega_c t) + \sin(\omega_b t - \omega_c t) + \sin(\omega_c t + \omega_b t) + \sin(\omega_c t - \omega_b t)\right] \\ &= \sin(\omega_b t + \omega_c t) \end{aligned} \tag{4.3}$$

This result is simply the original baseband signal shifted by the carrier frequency.

4.3. SSB applied to LDV

In this section, both methods of implementing the SSB approach in an LDV application are described. The first is the integrated electronic SSB modulator, and in the second the modulation and phase shifting elements are implemented optically.

4.3.1. Electronic implementation

Electronic SSB modulator components, such as the MAX2450 Quadrature (or I/Q) Modulator/Demodulator integrated circuit (IC), are readily available. These components are commonly used for digital and analogue RF modulation in mobile telephones and other communications equipment.

In order to use a quadrature modulator as an SSB modulation IC, two signal inputs with a phase difference of $\pi/2$ must be generated and applied to the IC. This is not a trivial task for electronic circuits because of the large bandwidth usually required. In an LDV optical set-up however, two-phase quadrature signals can be generated using the two-phase detection methods described in Chapter 2. After detection, the two-phase signals can be passed directly to the SSB modulator IC connected to an RF carrier signal generator. This results in an output that is shifted up by the carrier signal frequency. Figure 4.4 illustrates this method.

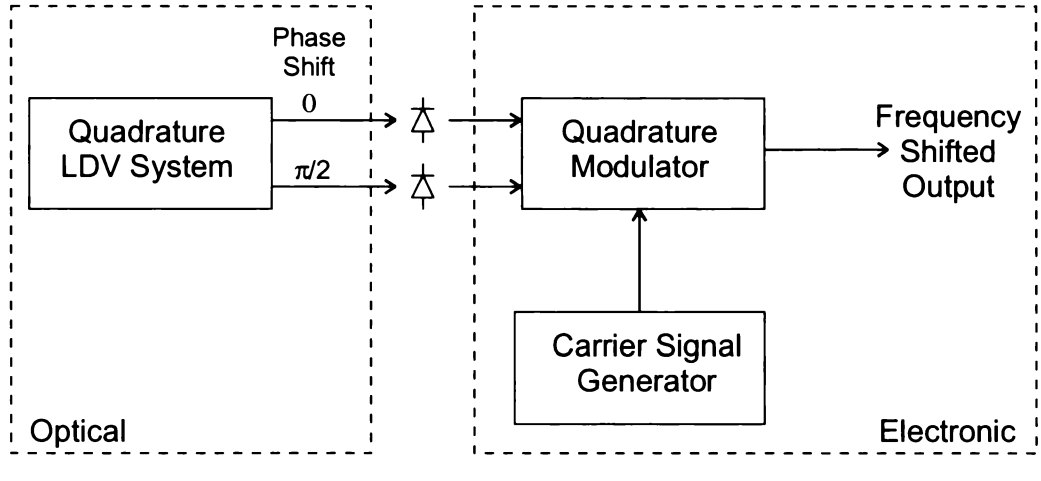

Figure 4.4 – Electronic implementation of SSB based frequency shifting, using an LDV system with a two signal quadrature output and a quadrature modulator.

4.3.2. Optical implementation

The electronic method relies on the use of an integrated circuit to perform the two separate AMSC modulations, phase shifting of the carrier and final summation. This IC can be removed by implementing the modulation and phase shifting optically, leaving only the summation that needs to be performed electronically. The nature of photodetectors, converting incident light into current, makes the summation a simple task of current addition, requiring only the simplest of electronics.

4.3.2.1. Description

An LDV system generates a Doppler signal by interfering two beams usually generated by the same laser, and thus the amplitude of the Doppler signal is dependant upon the output intensity of the laser. If the laser is amplitude modulated, the intensity of the detected Doppler signal will oscillate at this modulation frequency. This signal still contains the same Doppler information, but it is superimposed on the laser modulation signal. Because the intensity modulation has a multiplying effect on the Doppler signal, the result can be described as AM modulated. However, the carrier signal is optical and therefore contains a DC offset. As a result the suppressed carrier modulation is not achieved, but instead a full AM signal containing the carrier signal and both the upper and lower sidebands is produced.

If the LDV system is capable of producing a full quadrature output that contains four signals each with a phase difference of $\pi/2$, then the full AM output can be converted to the AMSC signal required for part of the SSB modulation process. To achieve these quadrature signals a beam combiner such as a 4x4 (or 2x4) planar wave-guide coupler could be used (Niemeier and Ulrich 1986, and Lang et al. 1998). All optical mixing occurs in the beam combiner, and hence optical phase is only critical at this point. Any delays experienced in the fibre optic cable after the beam combiner only affect the intensity variations, such as the carrier signal and Doppler signals.

Figure 4.5 shows the beam combiner and the optical and electronic processing required to perform a semi-optical SSB modulation. The signals at each point are depicted in the frequency domain with negative signals indicating a π phase shift.

Because the laser modulating signal is common to all of the outputs, the quadrature phase difference is only apparent on the Doppler information (AM sidebands), leaving the intensity modulated signal in-phase across all four outputs. Differencing two output signals that are π out-of-phase after detection cancels the in-phase carrier signal and preserves the out-of-phase sideband signals, thus providing an AMSC output. Hence, the full balanced modulated Doppler signal has been produced optically without the use of an electronic modulator.

Two of the four quadrature outputs have been used to create one of the AMSC signals required. The remaining two quadrature signals, are also π out-of-phase with each other, and therefore can be used to create another AMSC signal with a phase difference of $\pi/2$ in comparison to the previous one. Similarities can be seen between a Single Sideband Modulator (shown

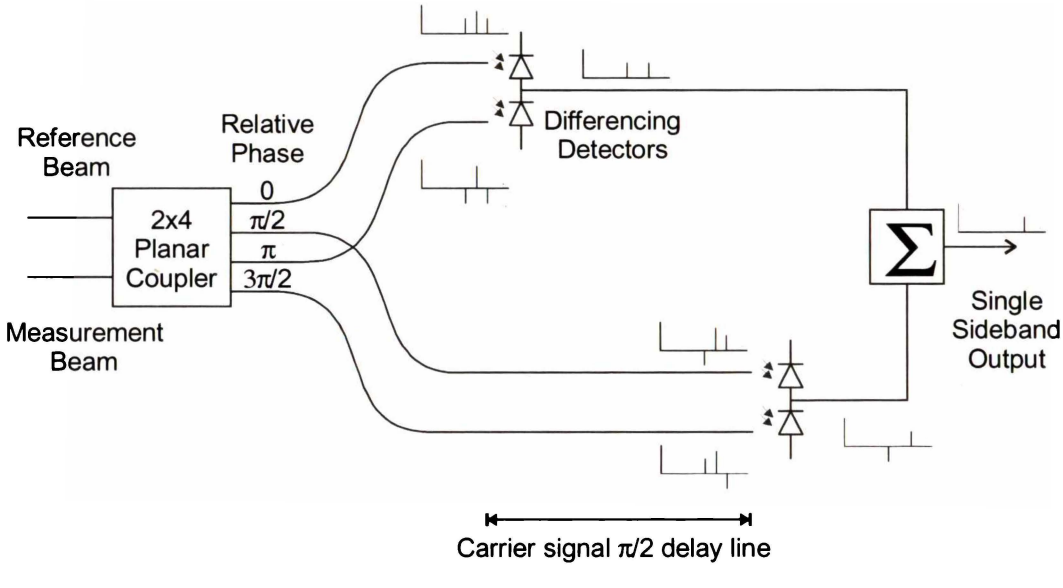

Figure 4.5 – Optical configuration for SSB type frequency shifting, shown in a fibre optic implementation. Also shown are the signals at each point in the frequency domain. Negative frequency lines indicate a π out-of-phase signal.

in Figure 4.2) and the Doppler signal processing so far. The differences between this and an electronic SSB modulator is the $\pi/2$ phase shift in the carrier signal, and the summation. A delay line of optical pathlength equal to one quarter of the carrier signal's wavelength can be used as a phase shift. The final step is to electronically perform the summation, resulting in a Doppler signal shifted by the frequency of the laser modulation.

4.3.2.2. Algebraic illustration

To illustrate this process algebraically, first consider the modulated (reference) laser beam as a spectral line at the laser frequency plus two sidebands. The complex wavefunction is then

$$\begin{aligned} U_r(t) = {} & a \cdot \exp\left[j(\omega t) \right] \\ & + \frac{1}{2} ab \cdot \exp\left[j(\omega t + \Omega t) \right] \\ & + \frac{1}{2} ab \cdot \exp\left[j(\omega t - \Omega t) \right] \end{aligned} \qquad 4.4$$

where a is the amplitude of the modulated laser, b is the modulation index (or depth), ω is the laser frequency, and Ω is the modulation frequency. The Doppler shifted beam can be expressed as

$$\begin{aligned} U_d(t) = {} & c \cdot \exp\left[j(\omega t + \Delta\omega t + \Delta\varphi) \right] \\ & + \frac{1}{2} cb \cdot \exp\left[j(\omega t + \Delta\omega t + \Omega t + \Delta\varphi) \right] \\ & + \frac{1}{2} cb \cdot \exp\left[j(\omega t + \Delta\omega t - \Omega t + \Delta\varphi) \right] \end{aligned} \qquad 4.5$$

where c is the amplitude of the Doppler shifted beam, $\Delta\omega$ is the Doppler shift, and $\Delta\varphi$ is the optical phase shift.

Including the reference beam and the Doppler shifted beams, there are six spectral lines. To find the beat signal produced when these beams are mixed on a detector, the superposition of each of these lines interfering with each other line must be calculated, as described in Appendix I. This gives us the total expression for interference of these two beams, which

simplifies to seven terms (ignoring the DC component). These terms can be separated into three categories:

1) Baseband Doppler signal

$$ac\left(2+b^2\right)\cos(\Delta\omega t+\Delta\varphi) \tag{4.6}$$

2) Modulating frequency and Doppler sidebands:

$$\begin{aligned} &2b\left(a^2+c^2\right)\cos(\Omega t)\\ &+2abc\cos\left(\Omega t+\Delta\omega t+\Delta\varphi\right)\\ &+2abc\cos\left(\Omega t-\Delta\omega t-\Delta\varphi\right) \end{aligned} \tag{4.7}$$

3) Twice the modulating frequency and Doppler sidebands:

$$\begin{aligned} &\frac{1}{2}b^2\left(a^2+c^2\right)\cos(2\Omega t)\\ &+\frac{1}{2}ab^2c\cos\left(2\Omega t+\Delta\omega t+\Delta\varphi\right)\\ &+\frac{1}{2}ab^2c\cos\left(2\Omega t-\Delta\omega t-\Delta\varphi\right) \end{aligned} \tag{4.8}$$

For simplicity, from here on we will consider only the frequencies of interest, which is the second category in the above list (Equation 4.7). This is the frequency at which the laser was originally modulated, plus two sidebands containing the Doppler signal. Hence, we will now call the laser modulating frequency the carrier, and the Doppler signal the sidebands.

If one signal was significantly weaker than the other, say the Doppler shifted beam (whose amplitude is represented by c), the resulting carrier amplitude, $2b(a^2+c^2)$, will not be adversely effected. However, the sidebands (or shifted Doppler signals) with the amplitude $2abc$ are directly affected, and will experience a drop in amplitude. The net result is a carrier signal that is very large in amplitude in comparison to the sidebands. This is an undesirable situation because it can be difficult to decode the small Doppler signal, which could easily be swamped by the large carrier signal.

From expression 4.7 it can be seen that the phase of the sidebands are affected by the laser phase ($\Delta\varphi$) and hence are different for each output of the beam combiner. However, the carrier is not affected and is therefore the same phase at all outputs. As a result, differencing the outputs of the beam combiner that have a relative sideband phase change of π (outputs 0 and π), causes the carrier to cancel and the sidebands to double in amplitude. It also has the convenient effect that any stray light or incoherent unwanted signals are also cancelled, as they are common to both outputs. We now have the signal

$$DSB_1 = 4abc\cos(\Omega t + \Delta\omega t) + 4abc\cos(\Omega t - \Delta\omega t) \qquad 4.9$$

which can be described as a double sideband suppressed carrier signal.

The inconvenient carrier signal has now been removed, but we still have no way of determining direction of motion. The other two outputs of the beam combiner ($\pi/2$ and $3\pi/2$) also have a relative phase change of π, so their carrier signal can also be cancelled. The expression for the resulting signal is

$$DSB_2 = 4abc\cos\left(\Omega t + \Delta\omega t + \frac{\pi}{2}\right) + 4abc\cos\left(\Omega t - \Delta\omega t - \frac{\pi}{2}\right) \qquad 4.10$$

Adjusting equation 4.10 to account for the inserted delay line requires a phase shift in the carrier signal. Subtracting $\pi/2$ provides the new expression

$$DSB_2' = 4abc\cos(\Omega t + \Delta\omega t) - 4abc\cos(\Omega t - \Delta\omega t) \qquad 4.11$$

Finally, taking the sum of equation 4.9 (the 0 and π signal) and equation 4.11 (the phase shifted $\pi/2$ and $3\pi/2$ signal), causes one sideband to be cancelled, while the other is enhanced, resulting in the single sideband signal

$$SSB = 8abc\cos(\Omega t + \Delta\omega t) \qquad 4.12$$

If the target is moving in the opposite direction, the opposite sideband would cancel resulting in a decrease rather than an increase from the carrier frequency. In other words, this system is direction discriminating.

This cancellation of one sideband will not be as efficient as it first appears. In our implementation, the $\pi/2$ phase shift of the carrier will also cause a phase shift in the sideband information, which has not been accounted for in the above derivation. A more rigorous derivation considers the delay line as a time delay rather than a phase change, and equation 4.11 becomes

$$\begin{aligned} DSB_2' = {} & 4abc\cos\left(\Omega(t-\Delta t)+\Delta\omega(t-\Delta t)+\frac{\pi}{2}\right) \\ & +4abc\cos\left(\Omega(t-\Delta t)-\Delta\omega(t-\Delta t)-\frac{\pi}{2}\right) \end{aligned} \tag{4.13}$$

where Δt is the time delay. This simplifies to

$$\begin{aligned} DSB_2' = {} & 4abc\cos\left(\Omega t+\Delta\omega t+\frac{\pi}{2}-\phi_1\right) \\ & +4abc\cos\left(\Omega t-\Delta\omega t-\frac{\pi}{2}-\phi_2\right) \end{aligned} \tag{4.14}$$

where the phase shifts are

$$\phi_1 = \Delta t(\Omega+\Delta\omega) \tag{4.15}$$

and

$$\phi_2 = \Delta t(\Omega-\Delta\omega) \tag{4.16}$$

The time delay is fixed at one quarter of the carrier signal's period:

$$\Delta t = \frac{\pi}{2\Omega} \tag{4.17}$$

and therefore, the phase shifts become

$$\phi_1 = \frac{\pi}{2}\left(1+\frac{\Delta\omega}{\Omega}\right) \qquad 4.18$$

and

$$\phi_2 = \frac{\pi}{2}\left(1-\frac{\Delta\omega}{\Omega}\right) \qquad 4.19$$

For purposes of discovering cancellation efficiency, consider only the cancelled sideband of equation 4.9 and equation 4.14 at time t=0. Normalising the amplitude for convenience, the sum of these sidebands becomes

$$SB_2 = 1+\cos\left(-\frac{\pi}{2}-\phi_2\right) \qquad 4.20$$

This value approaches zero for complete cancellation and 1 for no cancellation, so the cancellation efficiency can be found as 1-SB_2, which expands to

$$C = -\cos\left(\pi\left(1+\frac{\Delta\omega}{2\Omega}\right)\right) \qquad 4.21$$

If a ratio of carrier to maximum Doppler frequency of 10 is maintained, the worst case cancellation efficiency would be 80%. For a ratio of 100, the cancellation efficiency is 99.8%. At this level, amplitude mismatches would provide the most significant threat to cancellation efficiency.

4.4. FM receiver as Doppler decoder

Frequency Modulated (FM) radio signals convey information by shifting the carrier signal's frequency from its centre location in proportion to the modulating voltage as shown in Figure 4.6a. FM signals can be DC coupled with an increase in carrier frequency indicating a positive modulation voltage and a decrease indicating a negative voltage.

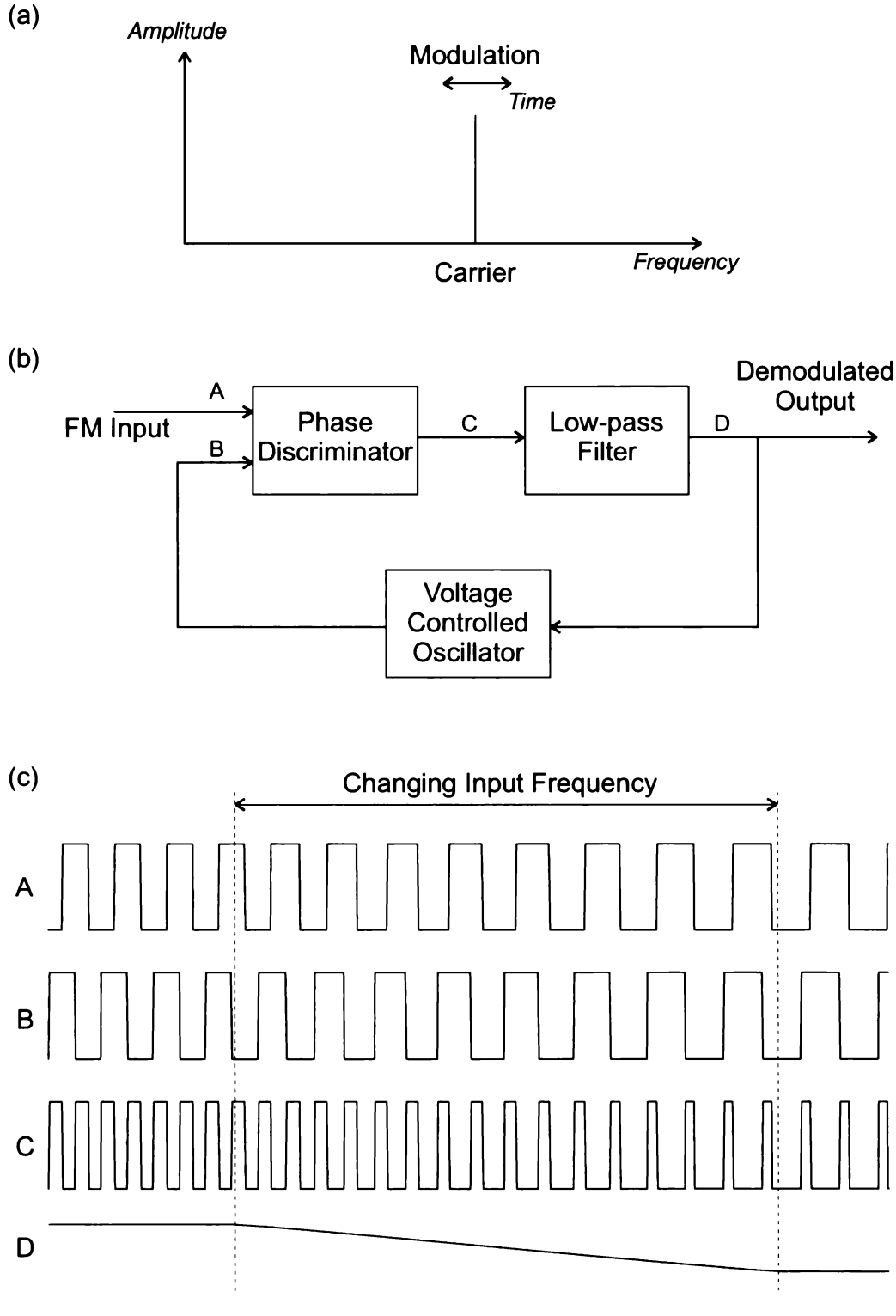

Figure 4.6 – FM Demodulation. (a)FM signal in the frequency domain, (b) Phase-Lock-Loop FM demodulator block diagram, and (c) Simulated FM signals in time domain.

Such signals are commonly decoded with a Phase-Lock-Loop (PLL) circuit, which tracks the changing radio frequency and produces a proportional output voltage, thereby reproducing the original modulating signal. Although a PLL is used to track frequency changes, it actually, as the name suggests, tracks phase changes in a feedback loop configuration as shown in Figure 4.6b.

A basic configuration utilises an "exclusive or" (XOR) type logic gate as a phase discriminator and locks the FM input signal and a generated reference signal at a phase difference of $\pi/2$. This results in a 50% duty cycle phase discriminator output that provides a half voltage DC level when low-pass filtered. This is passed to a voltage controlled oscillator (VCO) which generates the reference signal. The VCO is designed to produce a signal at the carrier frequency of the FM signal given a half voltage input. Any change in FM input frequency causes a different phase relationship between the reference and FM signals, resulting in a deviation of the low-pass filter output voltage. This in turn causes the VCO to adjust the reference frequency to match the new FM input signal and maintain the new phase difference. The demodulated signal can therefore be taken directly from the low-pass filter output.

Figure 4.6c illustrates the PLL operation though simulated time domain signals. This FM signal to be demodulated, illustrated as signal 'A', is first voltage limited to reduce interference from amplitude fluctuations. Signal 'B' is the reference VCO output, which is XORed with the input to produce signal 'C'. This is then low-pass filtered producing the demodulated output (and VCO control) signal 'D'.

The task of a Doppler signal decoder is very similar to an FM decoder in that it must convert an input frequency into an indication of velocity. This is particularly true when the velocity fluctuates and a frequency offset is applied.

Frequency tracking Doppler demodulators as described by Drain (1980) and Follett (1981) are not new, but in recent times have been overlooked in

favour of digital systems. Digital systems, however, are limited by the maximum sampling and data rates, and for real time measurement by the processing power available. This limits their usefulness in situations of high offset frequencies and rapidly changing Doppler signals, as well as small displacement and high frequency vibrometers (Dorrington and Künnemeyer 1998).

One example is the experimental results obtained in the previous chapter where only 64 data points were sampled per Doppler burst, and difficulty arose in determining accurate velocity estimates.

In an applied situation, this lidar arrangement would produce an almost continuous Doppler signal. It would have an offset frequency of 260 MHz and could change frequency at a rate of up to 30 MHz (for 30 ns pulses). Processing this signal digitally would provide a serious challenge, but a frequency tracker could follow the changing frequency and provide an output signal proportional to velocity.

Another example is a high frequency small displacement vibrometer. Small displacement signals are characterised by non-sinusoidal waveforms because the target does not move a full wavelength of light, and therefore a cyclic Doppler signal is not produced as illustrated in Figure 4.7. This is

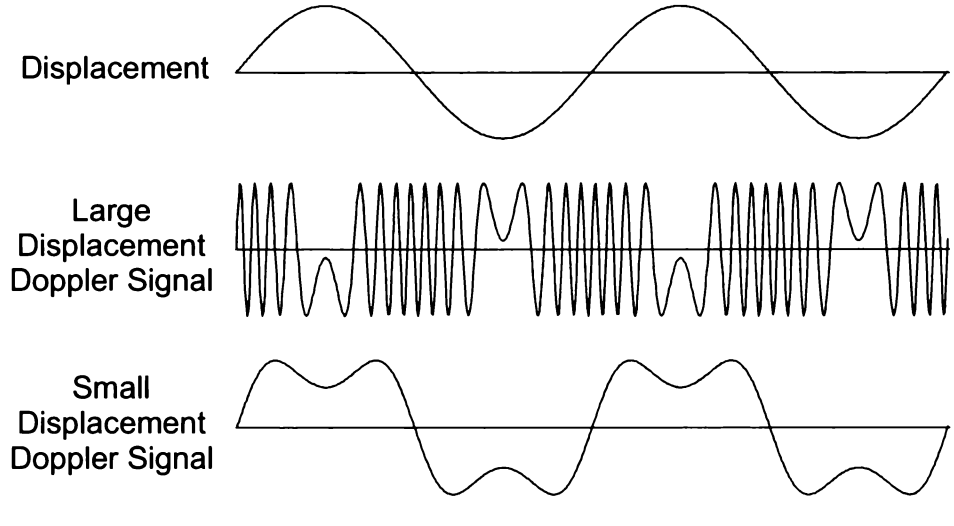

Figure 4.7 – Simulated Doppler signals showing the difference between large displacement (more than several wavelengths) and small displacement (less than a wavelength).

different to 'normal' Doppler signals, which usually have many cycles that can be counted to establish frequency before the velocity, and hence the frequency of the signal changes. Decoding these small displacement signals is usually done digitally (Müller et al. 1997), but if the Doppler frequency becomes too high, digital processing becomes prohibitive. The upper limit of digital processing depends on the available sampling and processing equipment, but is in the range from hundreds of kilohertz to hundreds of megahertz. In this situation, Frequency shifting and FM demodulating may provide a simple and effective method of decoding velocity.

The similarities of Doppler signals and FM radio signals can be seen algebraically by comparing the interference expression for sinusoidal displacement with the expression for sinusoidal FM modulation. This interference expression is equivalent to the Doppler signal and is a modified version of that given by Saleh and Teich (1991)

$$I = 2I_0\left[1+\cos\left[\frac{2\pi}{\lambda}D\cdot\cos(2\pi f_d t)\right]\right] \qquad 4.22$$

where I is intensity, λ is wavelength, D is maximum displacement, and f_d is displacement oscillation frequency. The expression for sinusoidal FM modulation is given by Zeines (1970) as

$$V = V_0\cos\left[2\pi f_c t+\frac{\Delta f}{f_m}\cos(2\pi f_m t)\right] \qquad 4.23$$

where f_c is the carrier frequency, f_m is the modulation frequency and Δf is the deviation. Ignoring the DC offset it can be seen that in terms of a FM signal the Doppler signal has a carrier frequency of 0 Hz, a modulation frequency equal the displacement frequency, and a deviation of

$$\Delta f = \frac{2\pi}{\lambda}f_d D \qquad 4.24$$

Deviation in terms of FM signals is a measure of the modulation depth and, more specifically, the frequency change due to modulation.

It is not practical to decode an FM signal with a carrier frequency of 0 Hz. However, in the case of a frequency offset Doppler signal, f_c would equal the offset frequency. Hence, a PLL can be used as a Doppler signal decoder producing a voltage output proportional to velocity.

4.5. Simulations

To test the new SSB modulation techniques numerically, both the electronic and semi-optical implementations were simulated in software (Mathcad 2000 Professional, Mathsoft Inc., Cambridge, USA). The input parameters where kept the same for both simulations to aid comparison of the two techniques. These input parameters are:

- Doppler frequency
- Modulation frequency
- Sample rate
- Simulation time period

A total of 8192 samples were used to represent a time period of 81.92 ms. The time domain graphs that follow do not show all of these points, because only the first few hundred points are required to illustrate the waveform. However, the simulated results are also shown in the frequency domain through graphs of the Fourier transformed data. In these transforms the 8192 point time period provides a resolution of approximately 12.2 Hz per bin, while maintaining a short computation time. The Mathcad documents are included in Appendix VIII.

4.5.1. Electronic implementation

The phasing method of SSB generation requires two inputs with phase difference of $\pi/2$. In the electronic implementation, these signals are generated by an optical interferometer, and high-pass filtered before being passed to the quadrature modulator. To simulate this arrangement, two Doppler signals were generated with the expression

$$Sig_n(i) = \cos\left(2\pi f_d \frac{i}{N} + \phi\right) \quad 4.25$$

where ϕ is the phase difference; f_d is the Doppler frequency of 305 Hz (25 cycles in the 81.92 ms simulation period); i is the sample number; and N is the total number of samples in the period. These signals are illustrated in Figure 4.8.

Also generated internally inside the quadrature modulator are two carrier signals with a $\pi/2$ phase difference. These carrier signals were generated in a similar fashion to the Doppler signal, except f_d is replaced with f_m which represents the modulation frequency

$$Carrier_n(i) = \cos\left(2\pi f_m \frac{i}{N} + \phi\right) \quad 4.26$$

In order to facilitate effective illustration of the modulated signals, the carrier was deliberately set to the relatively low frequency of 6.1 kHz, or 500 cycles in the simulation period.

Each Doppler signal was then mixed with the corresponding carrier signal

$$Mod_n(i) = Signal_n(i) \cdot Carrier_n(i) \quad 4.27$$

to produce two double sideband suppressed carrier modulated signals, illustrated in Figure 4.9. Note that when comparing these two signals, a $\pi/2$ phase difference can be observed in both the Doppler signal envelope, and the carrier signal itself.

Applying the two modulated signals to a summing amplifier, with the expression

$$SSB = Mod_1 + Mod_2 \quad 4.28$$

produces the desired Single Sideband (SSB) modulated signal, illustrated in Figure 4.10. To illustrate further, consider the two double sideband signals in the frequency domain, as shown in Figure 4.11. In order to show the

phase relationships these signals have been given a negative amplitude to depict a π phase change. This graph illustrates more intuitively the adding and cancelling of sidebands producing the single sideband result.

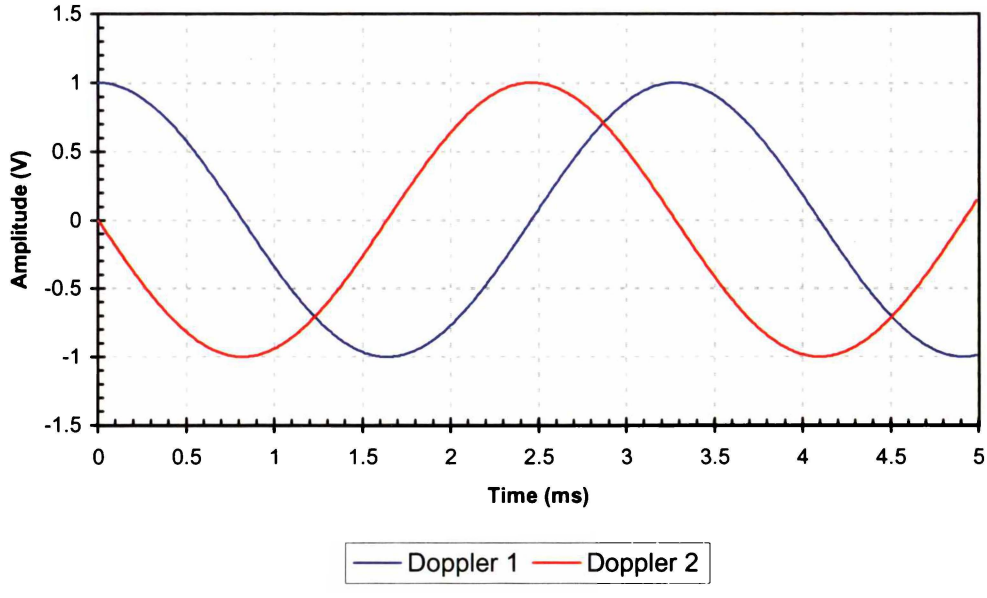

Figure 4.8 – Simulated Doppler signals with a π/2 phase difference, in the electronic implementation.

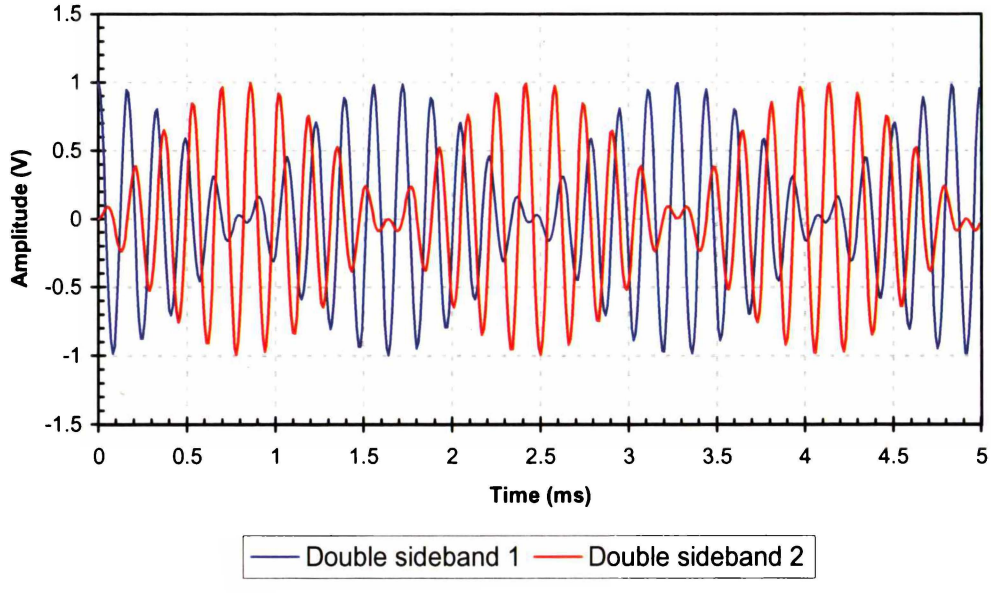

Figure 4.9 – Simulation of the modulated signals inside the phasing type single sideband modulator.

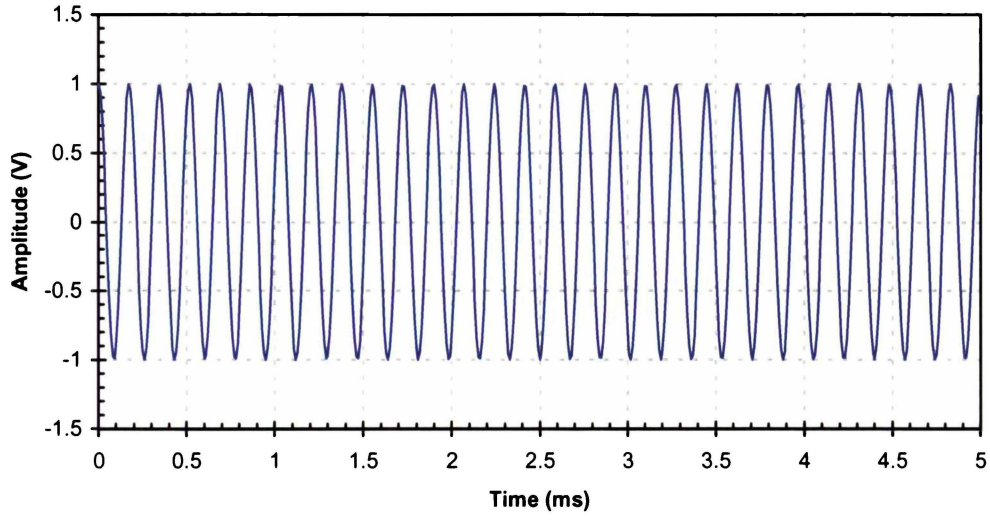

Figure 4.10 – Single sideband output generated by the electronic implementation simulator.

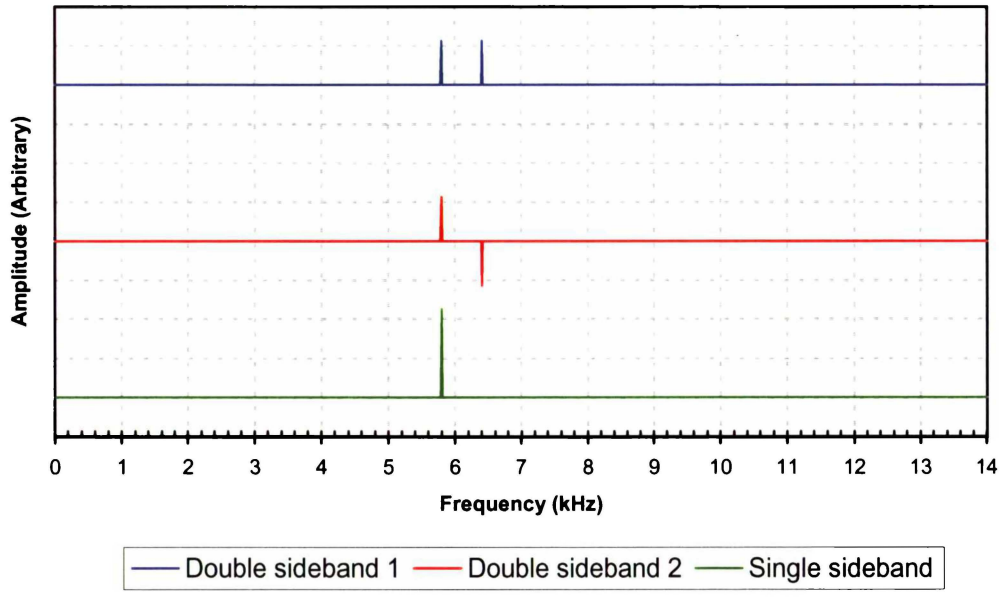

Figure 4.11 – Simulated signals of the electronic implementation in the frequency domain. Blue and red traces illustrate the two double sideband signals, which produce the single sideband signal shown in green when summed.

4.5.2. Semi-optical implementation

The simulation of the semi-optical implementation is more complex because of the interaction between the laser's intensity modulation and the Doppler beat signals on the detector. The Doppler signal is effectively an intensity modulation and therefore is always positive, and often does not

approach zero. Accordingly, a DC offset of 2 (represented by α) was applied to the simulated Doppler signal

$$Sig_n(i) = \cos\left(2\pi f_d \frac{i}{N} + \phi\right) + \alpha \qquad 4.29$$

For this implementation four signals were generated with phase shifts in multiples of $\pi/2$ as illustrated in Figure 4.12.

The intensity modulation applied to the laser is sinusoidal, but when this beam is incident on a detector the resulting signal contains more than just the modulating component. In Chapter 2, the mixing of two constant intensity laser beams was described, but now this must be expanded to include an intensity modulated source.

To calculate the intensity modulation at the detector we need to consider only one incident beam. The complex wave function (with the spatial dependence suppressed for convenience) of this beam is

$$U(t) = \alpha \exp(j\omega_l t)(\beta + \cos(\omega_m t)) \qquad 4.30$$

where ω_l and α are the is the laser's angular frequency and amplitude; ω_m and β are the modulating angular frequency and DC offset, and t is time. Finding the magnitude squared of expression 4.30 reveals the detected signal, which simplifies to

$$I(t) = \alpha^2\beta^2 + 2\alpha^2\beta\cos(\omega_m) + \alpha^2\cos^2(\omega_m) \qquad 4.31$$

Hence, the simulated carrier signal is generated with the expression

$$Carrier_n(i) = \alpha^2\beta^2 + 2\alpha^2\cos\left(2\pi f_m \frac{i}{N} + \phi\right) + \alpha^2\cos^2\left(2\pi f_m \frac{i}{N} + \phi\right) \qquad 4.32$$

with α=1 and β=2. In this situation, only one carrier signal is required because it is applied at the laser source and not in an electronic mixing process as before. To derive the detected optical signals the Doppler signal is multiplied by the carrier signal, providing

$$Mod_n(i) = Sig_n(i) \cdot Carrier(i) \tag{4.33}$$

producing the signals illustrated in Figure 4.13. Once again, note that each Doppler envelope is π/2 out-of-phase, but the carrier signals are all in-phase.

In order to achieve the phase difference required in the carrier signal, an optical delay is employed, which is simulated with the expression

$$ModDelayed_e(i) = Mod_e\left(i - \frac{1}{4}\frac{N}{f_m}\right) \tag{4.34}$$

where the subscript *e* indicates even numbered signals, and N/f_m is the wavelength of the modulating signal.

As described in the section 4.3.2.2 above, these signals contain both sidebands and the carrier frequencies. To remove the carrier frequency the two signals with a Doppler envelope phase difference of π are differenced causing the in-phase carrier signal to be cancelled. This is simulated with the expressions

$$DSB_1(i) = Mod_1(i) - Mod_3(i) \tag{4.35}$$

and

$$DSB_2(i) = ModDelayed_2(i) - ModDelayed_4(i) \tag{4.36}$$

resulting in the signals illustrated in Figure 4.14.

It can be seen from this graph that the Doppler envelope and the carrier signal are π/2 out-of-phase. These signals vary from their counterparts in the electronic implementation, of Figure 4.9, by the addition of a baseband Doppler signal superimposed on the modulated carrier.

The removal of the carrier signal can be illustrated further in the frequency domain, as shown in Figure 4.16. Between the two signals, the sidebands are out-of-phase while the carrier is in-phase, causing its cancellation when

differenced. The baseband Doppler signals, the $2f_m$ carrier, and sideband signals are also observable.

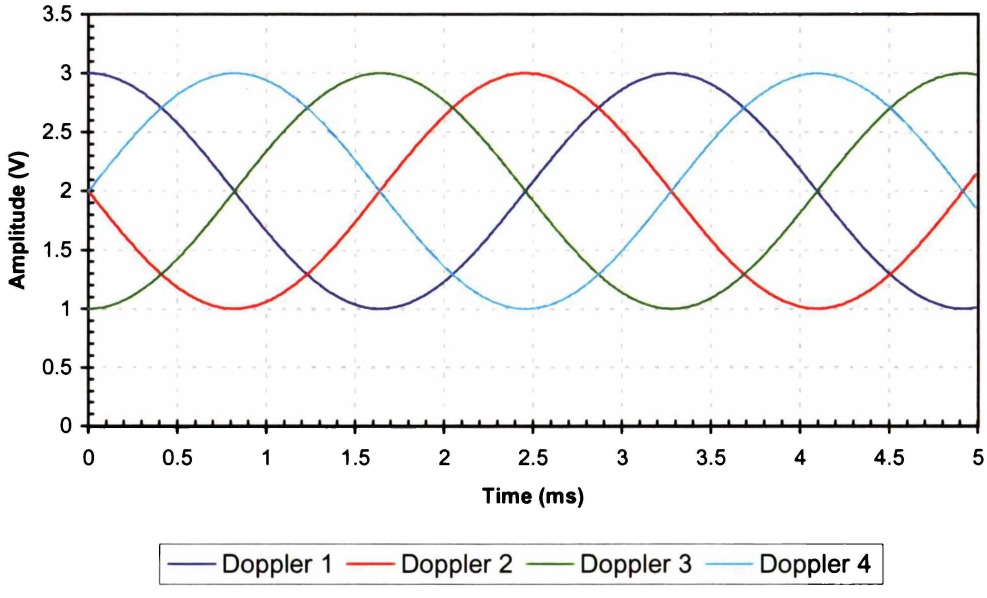

Figure 4.12 – Simulated Doppler signals for semi-optical implementation.

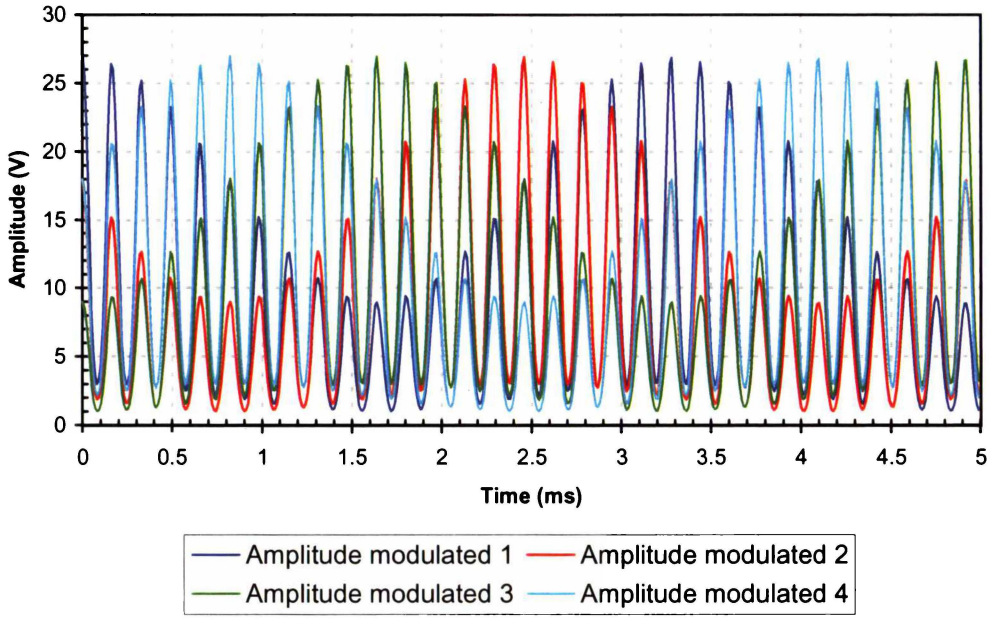

Figure 4.13 – Simulated Doppler signals detected in the semi-optical implementation.

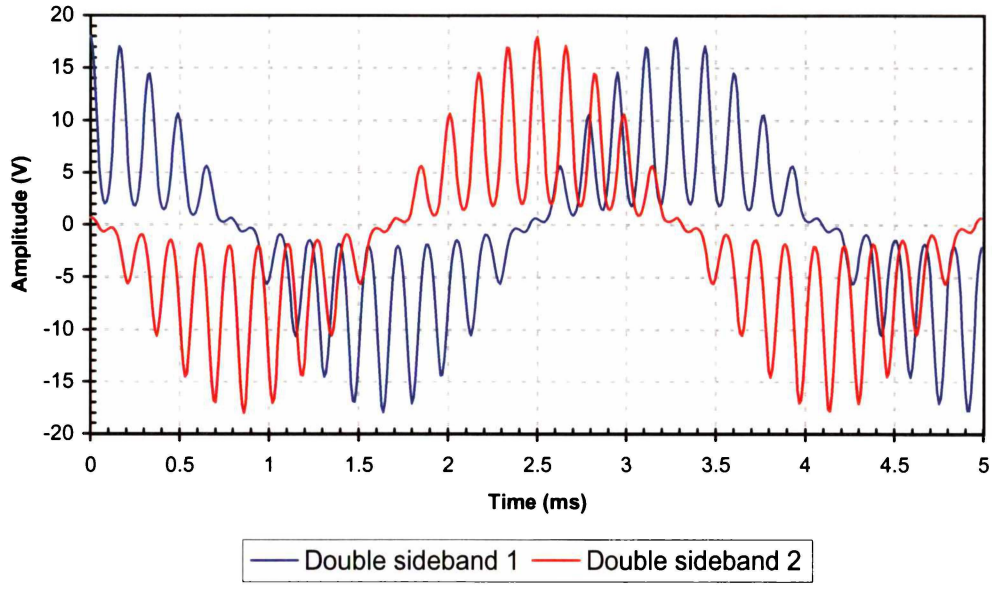

Figure 4.14 – Double sideband signals produced by semi-optical implementation simulation.

Now that two double sideband suppressed carrier signals have been obtained, they are then summed

$$SSB(i) = DSB_1(i) + DSB_2(i) \qquad 4.37$$

to produce the desired single sideband signal, illustrated in Figure 4.15.

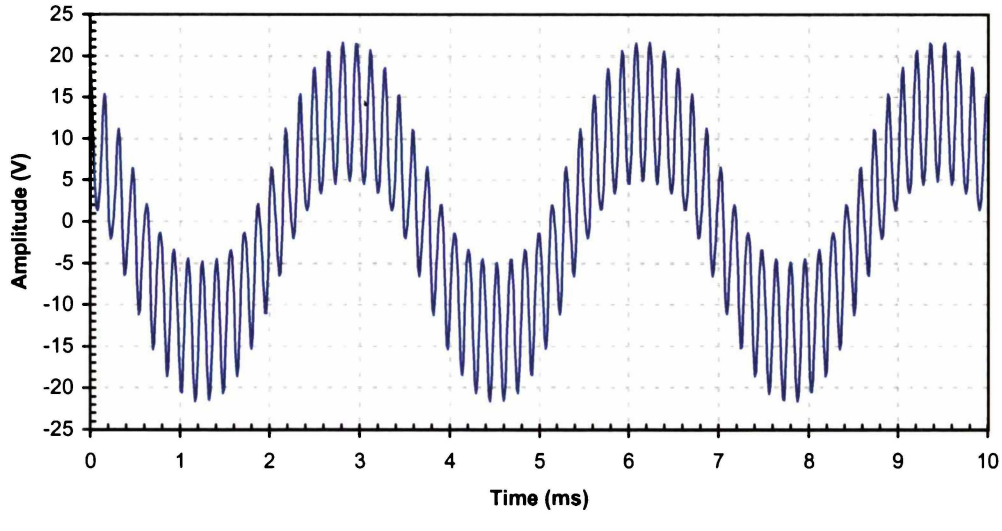

Figure 4.15 – Single sideband signal produced by the semi-optical implementation simulation.

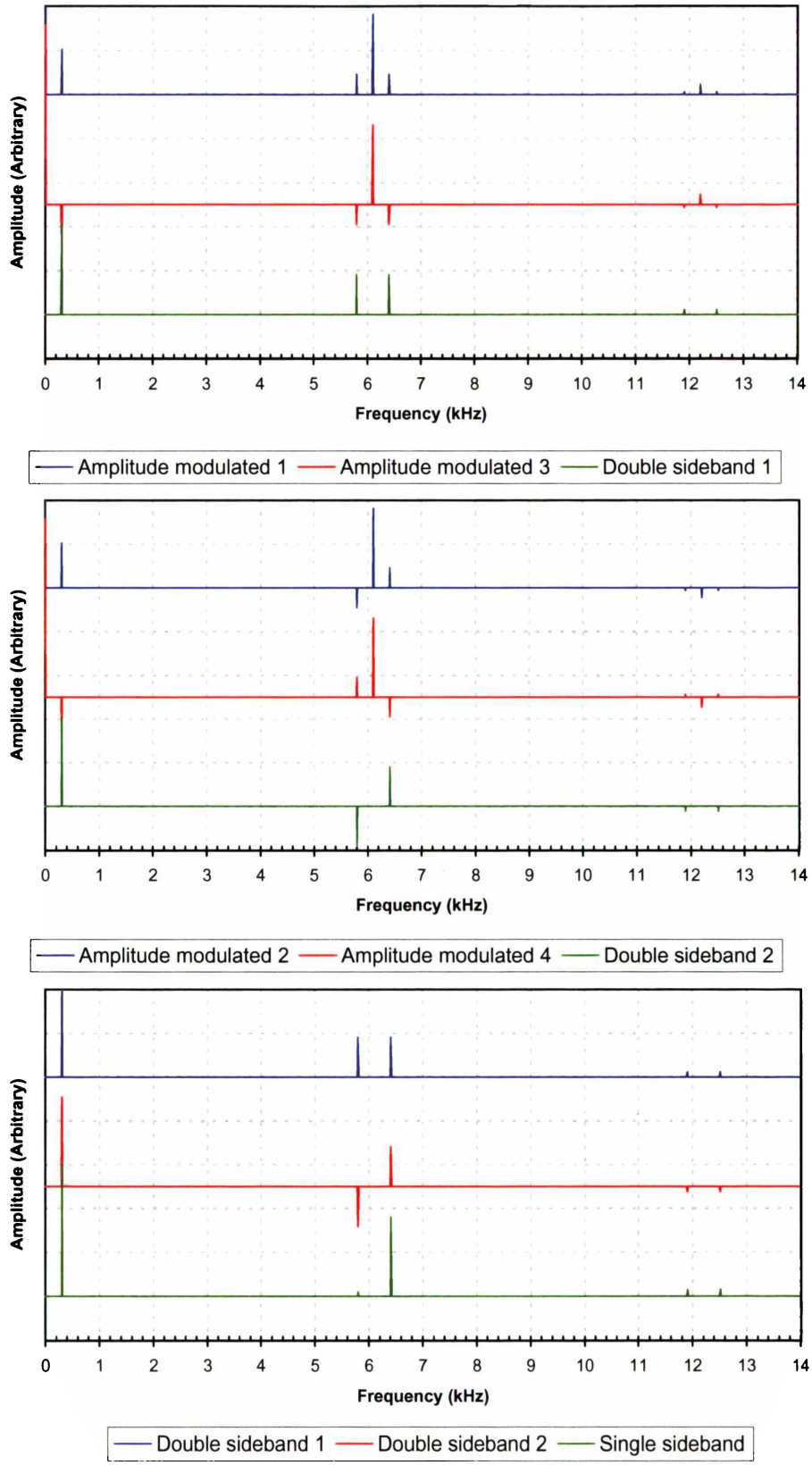

Figure 4.16 – Simulated amplitude modulated, double sideband, and single sideband signals from the semi-optical implementation in the frequency domain.

Once again, this process can be illustrated, as in Figure 4.16, in the frequency domain. As discussed in the theory section above, the unwanted sideband is not cancelled completely because the delay line used to phase shift the carrier, also applies a phase shift to the Doppler envelope. Expressed as a fraction of wavelength, this shift is small in comparison to the shift applied to the carrier signal, however, the Doppler envelope is no longer exactly $\pi/2$ out-of-phase.

4.6. Experimental validation

To test the LDV offset methods described above, an experiment was developed to prove the following concepts:

- SSB frequency shifting, electronic implementation
- SSB frequency shifting, semi-optical implementation
- FM receiver as Doppler decoder

4.6.1. Experimental set-up

A piezo-mounted mirror in a Michelson interferometer was used to generate the quadrature Doppler signals, which were then processed with the SSB methods, to derive the velocity of the mirror. This set-up is illustrated schematically in Figure 4.17a, and photographically in Figure 4.18.

4.6.1.1. Optical arrangement

A 660 nm, 35 mW laser diode (HL6501MG, Hitachi Ltd., San Jose USA), mounted in a laser diode driver module (LDC500, TCLDM9 & TEC2000, Thor Labs Inc., Newton USA) was used as the light source. One of the interferometer mirrors was tilted slightly creating a vertical interference pattern, which was incident on four cleaved multimode fibres arranged in a horizontal bundle as illustrated in Figure 4.17b, and Figure 4.19. The fringe spacing was adjusted to match the total distance across all four fibres, thereby creating a four-signal quadrature output as an interference fringe passes across the bundle. The elliptical nature of the laser diode output was utilised by aligning the fibre bundle along the major axis of the

beam. A cylindrical lens focused the minor axis on the bundle, aiding coupling efficiency.

In order to place the entire fibre bundle in one fringe required a bundle of approximately 1 mm in width, meaning a fibre with cladding size in the order of 250 μm. The 3M fibre FT-200-URT (Thor Labs Inc., Newton USA) was used because of its high numerical aperture (0.48), large 200 μm core, and 225 μm cladding diameter.

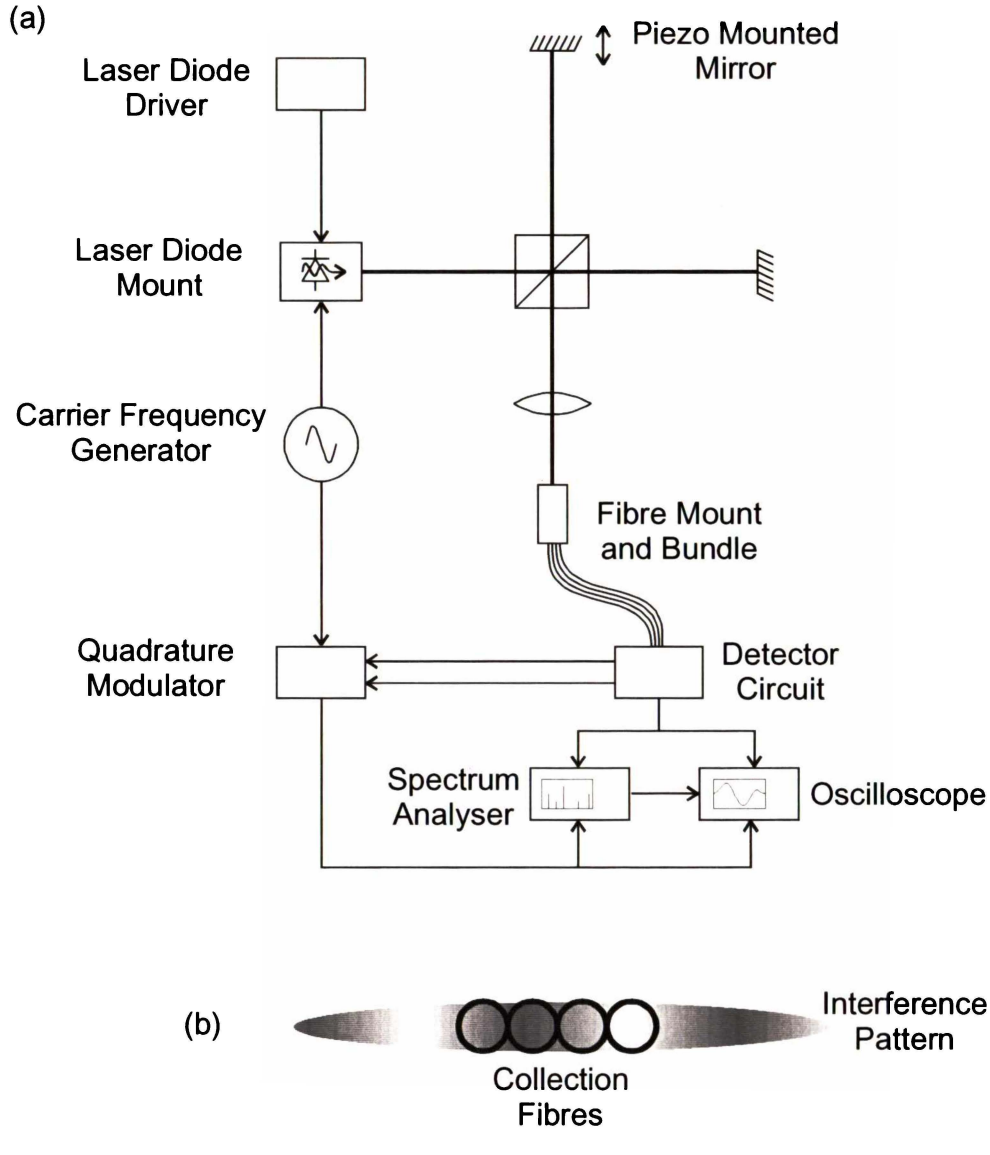

Figure 4.17 – Set up for single sideband frequency shifting experiments. (a) Optical set-up schematic. Note: not all connections are used simultaneously. (b) Fibre collection bundle positioned in the interference pattern.

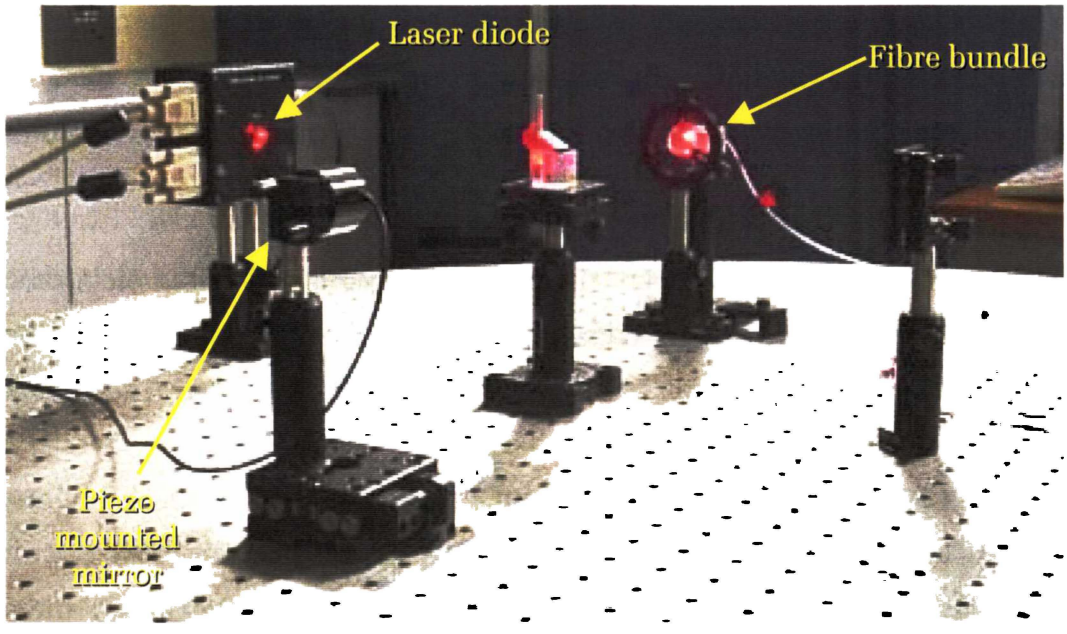

Figure 4.18 – Photograph of single sideband frequency shifting optical set-up.

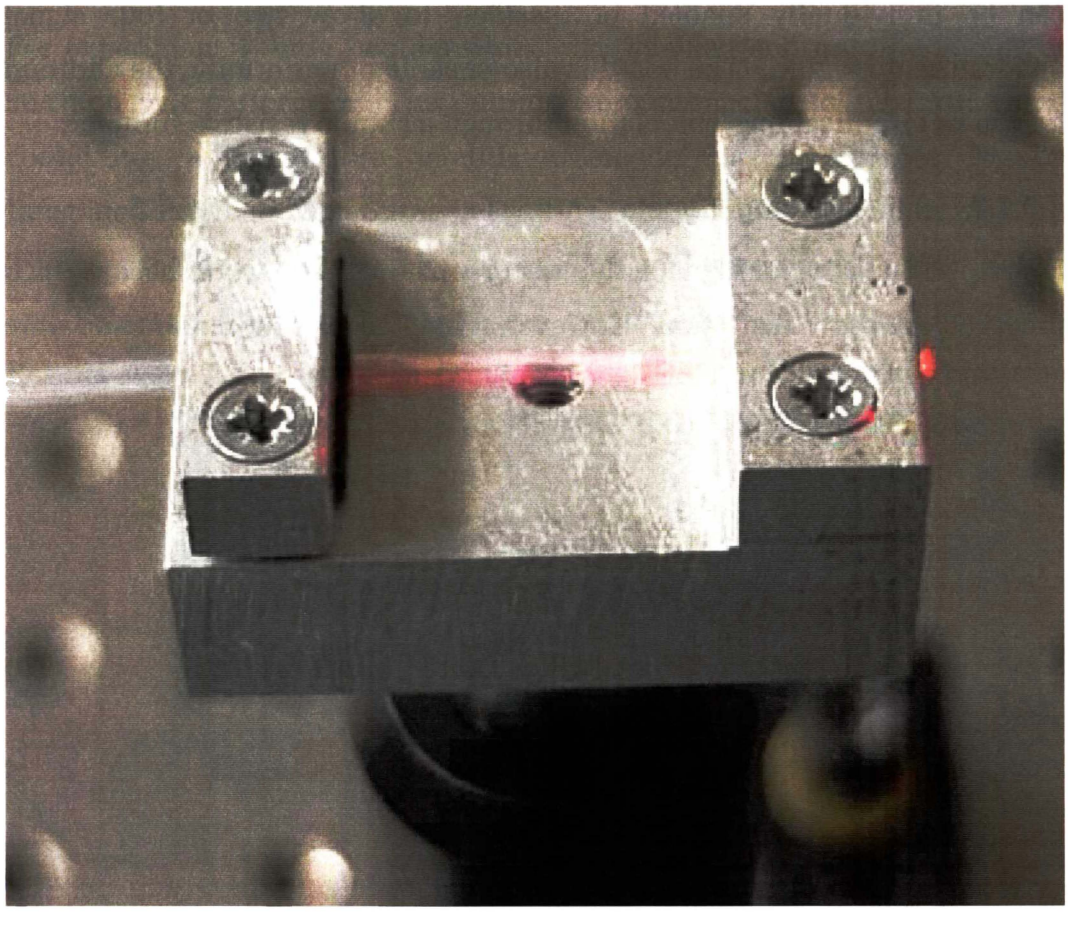

Figure 4.19 – Photograph of fibre bundle head arrangement in single sideband frequency shift experiment.

This arrangement is not very efficient, but acceptable for the purposes of the experiment. The fibre-optic cables were terminated in SMA connectors and attached to the detection electronics.

4.6.1.2. Processing electronics

Two separate experiments were performed to validate both the electronic and semi-optical methods. Common to both experiments was the photodetector board containing four 125 MHz analogue amplified photodetectors (HFBR-2406, Agilent Technologies, Santa Clara USA) and two high speed operational amplifiers (CLC425, National Semiconductors, Santa Clara USA). This board is shown in Figure 4.20, and full circuit diagrams and PCB layouts are included in Appendix VII. The amplifiers were configured to perform the differencing operation as well as provide 23 dB of gain, while maintaining the 125 MHz bandwidth. Each detector can be individually enabled or disabled to allow two or four signal quadrature operation. The board is also capable of performing the addition for the semi-optical implementation through a simple resistive summer.

4.6.1.3. Driving signals

For capturing Doppler signals, the mirror was driven at 1 kHz because this provided the best illustration. However, when velocity measurements were

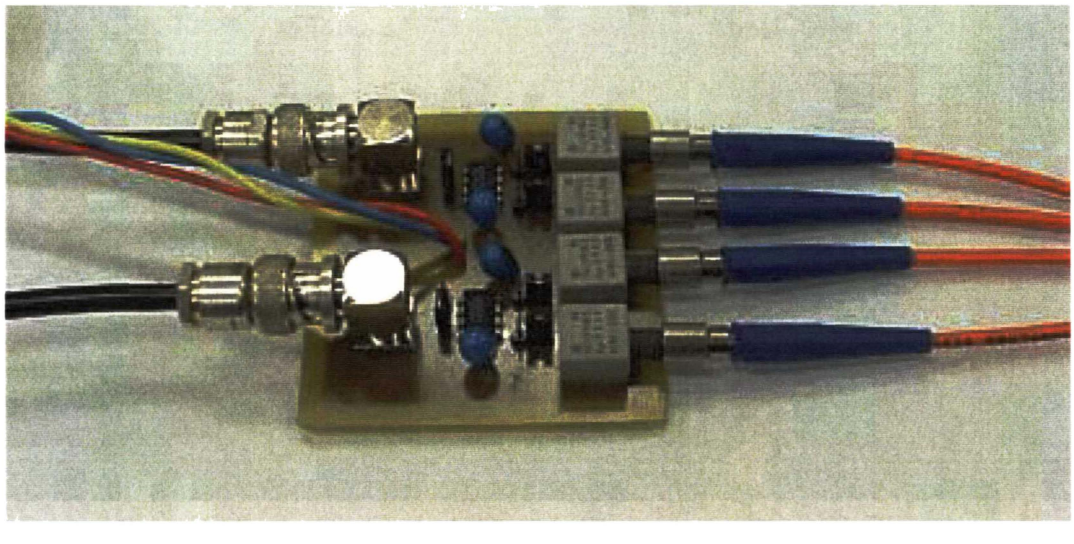

Figure 4.20 – Photograph of detector electronics for single sideband frequency shift experiment.

made, it was driven at 400 Hz. In the large displacement case the mirror was driven with a 10 V peak signal and for small displacement with 750 mV.

A 30.25 MHz carrier frequency was chosen for two reasons. Firstly, the optical pathlength of the carrier delay line in the optical implementation corresponded to a quarter-wave at approximately 30 MHz. Secondly, the oscilloscope was not capable of capturing one cycle of the Doppler signal without aliasing the carrier signal. To overcome this problem the oscilloscope was set to a sampling rate of 1 Msps, and the aliasing was used to transform the carrier signal to an apparent 250 kHz. This was done for observation purposes only, providing a convenient way to monitor both the Doppler and carrier signals simultaneously.

4.6.1.4. Experimental configurations

For experiment 1, only two detectors were enabled and no differencing or addition was performed. The outputs were connected to a second board containing a quadrature modulator/demodulator (MAX2450, Maxim Integrated Products Inc., Sunnyvale USA) configured as an SSB modulator. The carrier signal was provided by an RF signal generator (SYM02, Rohde and Schwarz, Munich Germany) and connected to the modulator input. Results were taken using an oscilloscope (TDS360, Tektronix, Beaverton USA) and spectrum analyser (R3131, Advantest, Tokyo Japan) configured as an FM receiver.

Experiment 2 utilised only the detector board with all four inputs, differencing and addition enabled. The carrier frequency generator was this time connected to the laser diode's RF modulation input. Once again, results were recorded on the oscilloscope and spectrum analyser.

4.6.2. Results

Firstly, results from arctangent digital processing algorithm, which is commonly used in the literature, are presented. This forms a basis with which the FM decoded signals can be compared. The FM decoded results are presented as modulated and unmodualted Doppler signals, and as

graphs of the mirror driving signals and decoded mirror velocity. In all following graphs both the drive voltage and the velocities have been normalised to 1 V peak for ease of illustration.

The mirror was driven with sine, square and triangle signals, which approximately represent the mirror displacement. Because the measured velocity is the differential of displacement, the decoded velocity waveforms produced are sinusoidal, spike, and square respectively.

Measurements were taken for both double sideband and single sideband modulated signals, which clearly illustrates the ability for direction determination in single sideband mode. Results were also taken at large (several wavelengths of light) and small (less than one wavelength) mirror displacements, to illustrate the potential for these techniques in small displacement regimes.

4.6.2.1. Arctangent processing

In order to establish the relationship between the mirror drive signal and the actual mirror displacement, Doppler signals were sampled and processed with the standard approach. The arctangent algorithm (Czarske et al. 1993) was chosen for its simple implementation in software.

The phase change signal, which relates directly to displacement, was calculated as

$$\phi(t) = \tan^{-1}\left(\frac{S_1(t)}{S_2(t)}\right) \qquad 4.38$$

where S_1 and S_2 are two Doppler signals with a $\pi/2$ phase difference. Care must be taken to ensure that these Doppler signals have the same amplitude. Unfortunately, the phase change signals (illustrated in Figure 4.21) never exceeds $\pi/2$ or $-\pi/2$, and hence the resulting signal is "wrapped" about zero. To compensate, an offset signal was generated by considering any phase change of more than 1.2 radians in one sample to be

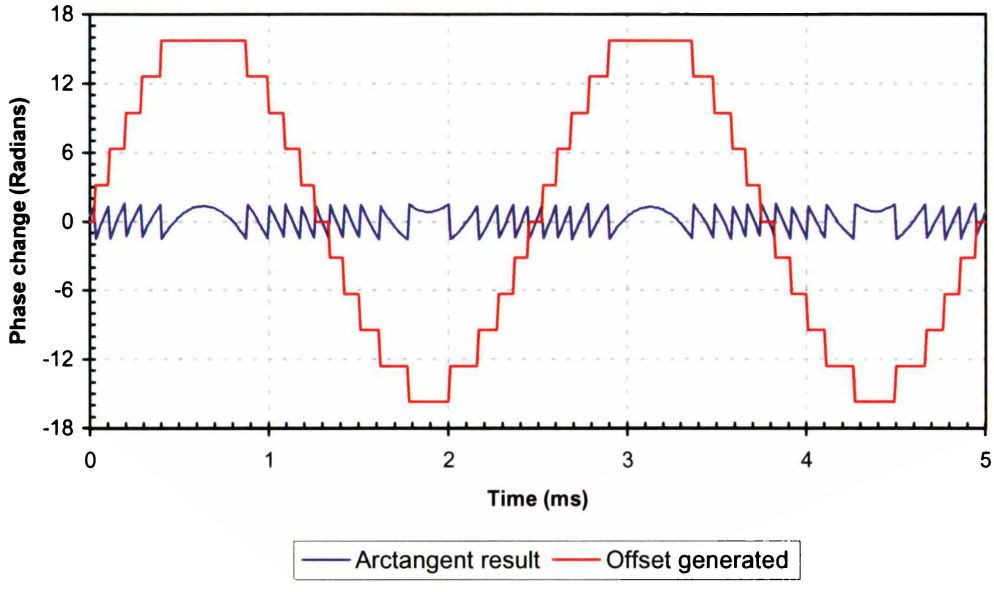

Figure 4.21 – Signals generated during arctangent processing. Raw arctangent result "wrapped" and generated offset signal

a transition across a $\pi/2$ boundary. The offset signal was increased or decreased by π depending on which boundary was crossed.

A calculated velocity signal can also be derived as the numerical differential of the phase change signal. This provides a useful baseline comparison for the results obtained in the experiments. The Matlab code used to perform this processing is included in Appendix V.

Figure 4.22 shows the drive waveform, phase change signal and calculated velocity produced with a sinusoidal, square, and triangle drive of 400 Hz at 10 V. The sinusoidal drive and displacement wave shapes match well, indicating that the drive signal is a good approximation of the displacement for a sinusoidal drive. Because the displacement is calibrated in radians, and a displacement of 2π radians corresponds to one wavelength of the illuminating laser, the actual displacement can be calculated. The peak-to-peak phase change is 31.8 radians, which equates to a total displacement of 3.33 μm because the laser emits at 658 nm (at 25°C according to the data sheet).

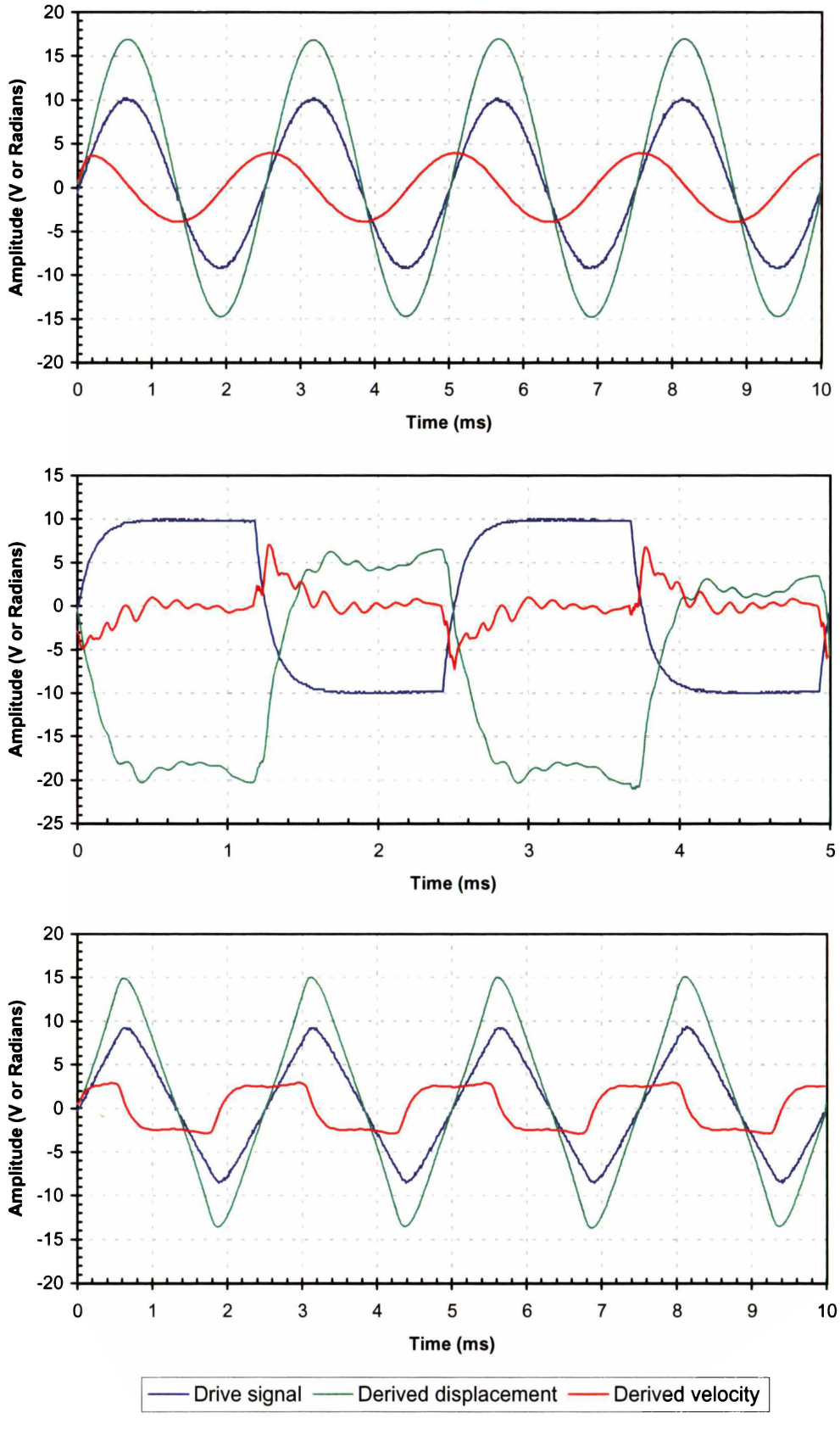

Figure 4.22 – Drive, displacement, and velocity signals obtained from the arctangent algorithm for a sinusoidal, square and triangle drives.

For the square wave drive signal the sampled time fame had to be shortened because during the fast transitions the Doppler signal was of sufficiently high frequency to cause aliasing on the oscilloscope. Another option would have been to employ a more sophisticated measurement tool that was capable of storing more points, therefore allowing the same time period to be sampled at a higher rate. This highlights one of the shortcomings of digital processing methods, which could be overcome with the new SSB methods being presented here.

The actual displacement with a square wave drive does not agree with the drive signal particularly well. It appears that the mirror dynamics cause some oscillations during the flat periods of the drive waveform.

The triangle drive signal and the displacement it causes correlate fairly well. However, the velocity waveform shows that the mirror dynamics still have an effect, especially at the direction reversal point where the mirror must be decelerated, and then accelerated in the opposite direction.

4.6.2.2. Electronic implementation

As mentioned previously, two Doppler signals are required as inputs to the quadrature modulator. The signals produced by the experiment are illustrated in Figure 4.23.

The quadrature modulator produces the single sideband signal by summing two double sideband signals. Therefore, when only one Doppler signal is applied, one of the double sideband signals is missing, resulting in the other as an output. Both the double and single sideband modulated signals are illustrated in Figure 4.24.

Breaking this data into eight equal time intervals (or time slots) and performing an FFT on each of these intervals produces a frequency domain representation of these modulated signals against time. Figure 4.25 shows the frequency domain plots for both the double sideband data and the single sideband data. This processing was performed in Matlab using the code included in Appendix IV. The direction can not be discriminated in

the double sideband case, but the shift from negative to positive velocity is clearly visible in the single sideband signal.

Figure 4.26 shows the mirror drive voltage and decoded velocity for both the single and double sideband signals with sine, square, and triangle drive waveforms. Again, the direction can not be derived for the double

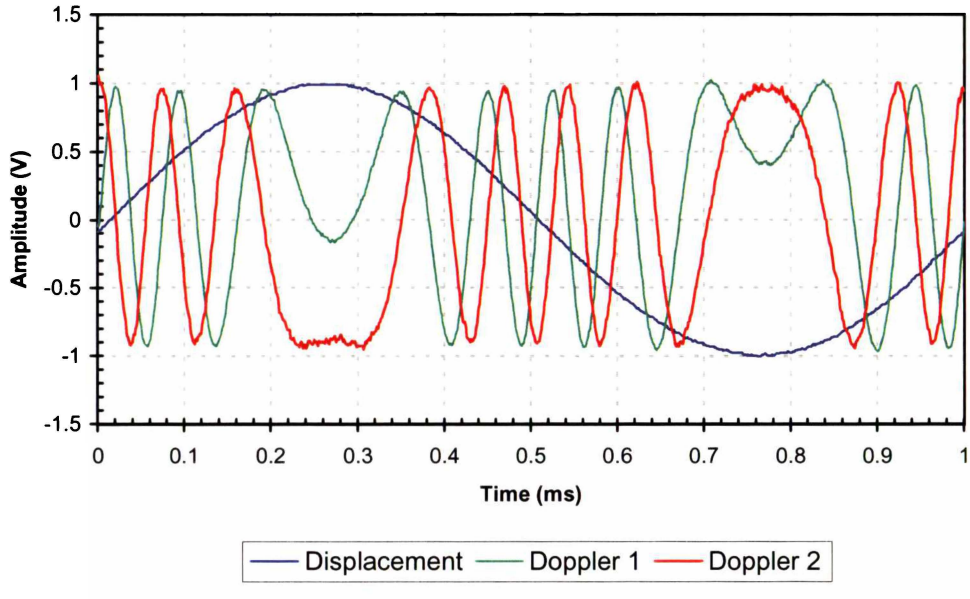

Figure 4.23 – Displacement and Doppler signals produced by the experimental set-up configured for the electronic implementation.

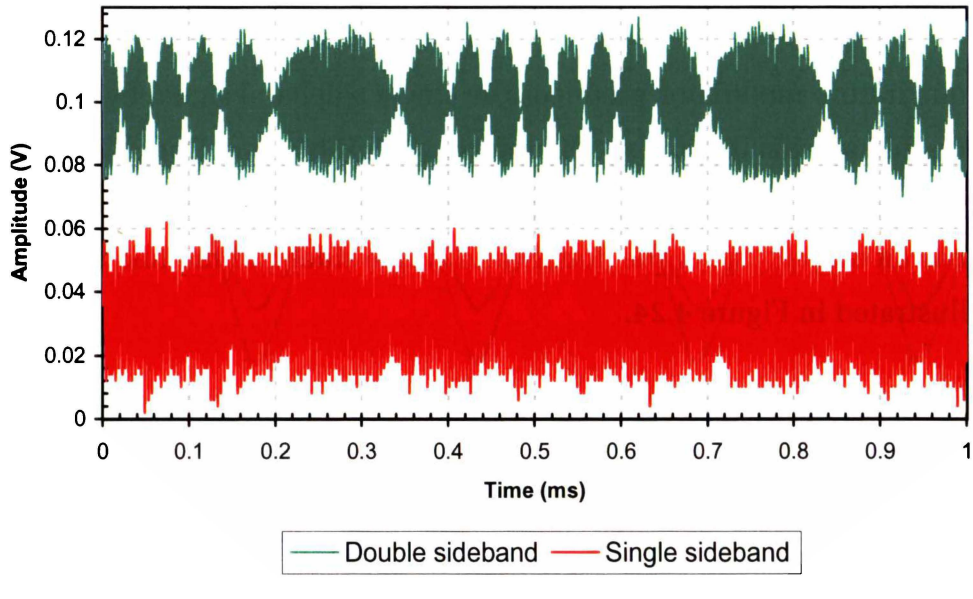

Figure 4.24 – Double and single sideband signals from quadrature modulator in the electronic implementation.

sideband signal but can be from the single sideband signal.

As expected, the decoded velocity is the differential of the driving signal within bandwidth limits of the FM demodulator. The velocity obtained for a sinusoidal displacement agrees with the results obtained with the arctangent method. For the square displacement however, the higher frequency oscillations are not present showing the lack of frequency response of the FM demodulator. Also, some overshoot is observable for both the square and triangle drive, again probably due to the FM demodulator.

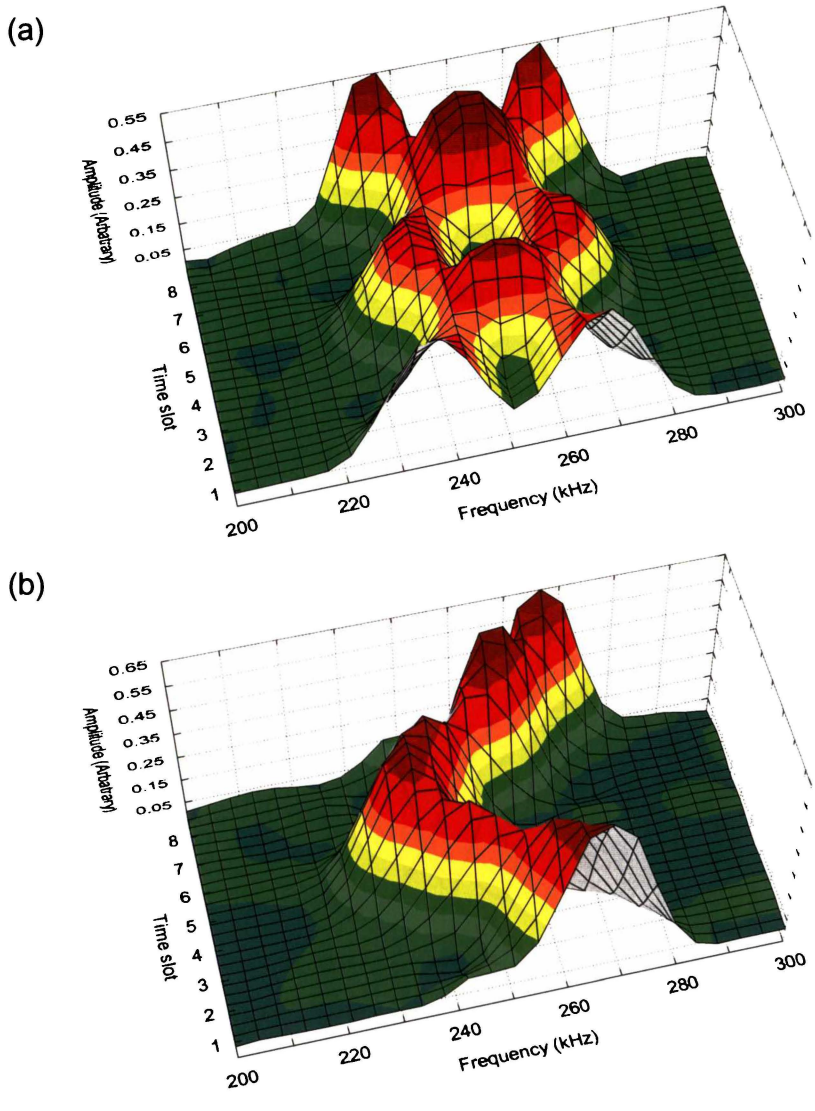

Figure 4.25 – Frequency domain plots from electronic implementation. (a) Double sideband data. (b) Single sideband data.

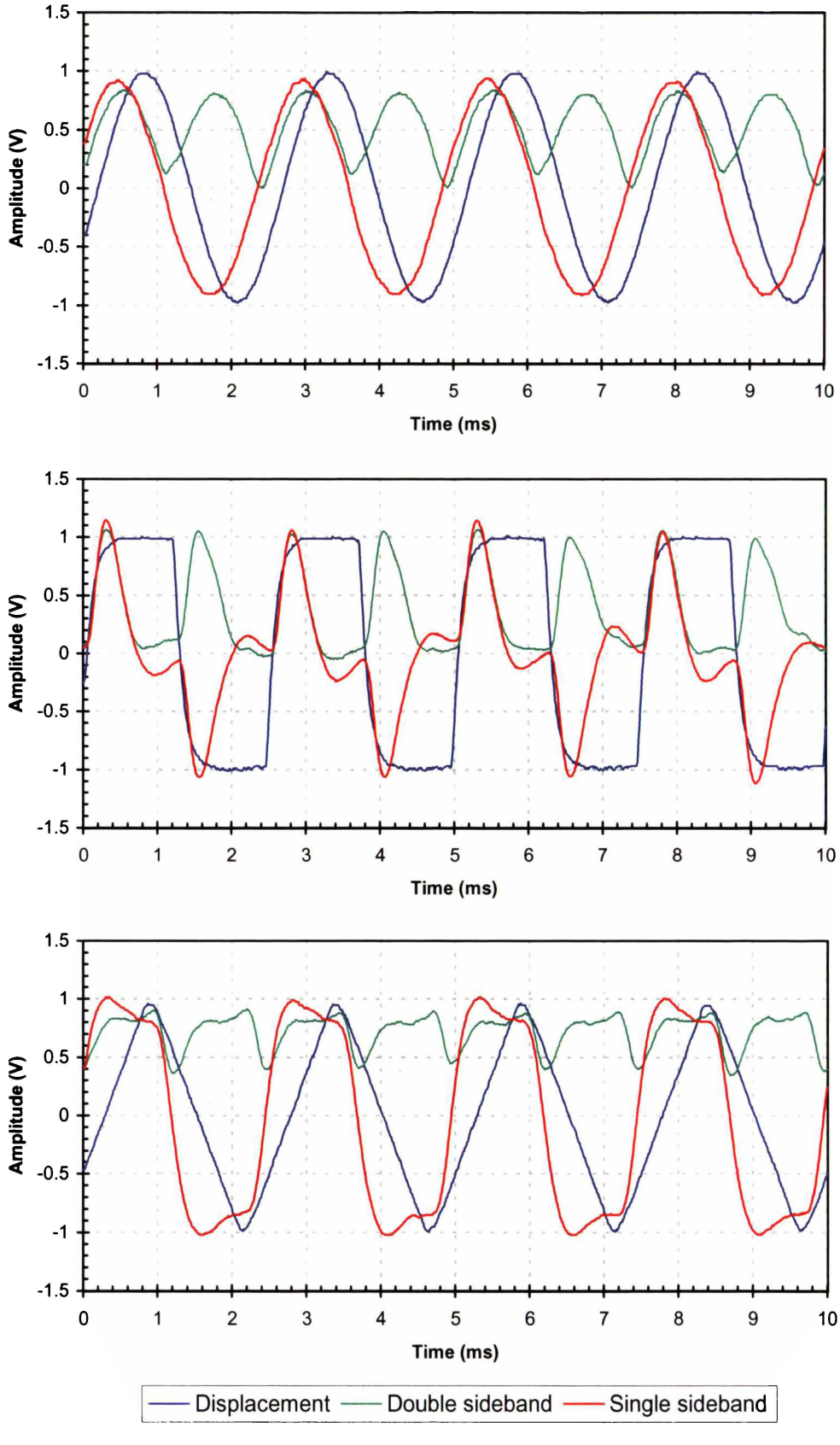

Figure 4.26 – Displacement and decoded velocity waveforms of double and single sideband signals for sine, square, and triangle drives in the electronic implementation.

Results were also obtained with the small displacement mirror drive, for displacements less than one wavelength of light. This time however, the Doppler signals were significantly different, as illustrated in Figure 4.27. Despite the lack of any full cycles from which frequency and hence velocity can be derived, velocity information is still contained within the signal and measurements were still obtainable. In this experiment a poor signal-to-noise ratio was experienced and therefore the results were averaged 32 times on the oscilloscope. These measurements shown in Figure 4.28.

The decoded velocity corresponds to the expected results poorly. These inconsistencies are caused by the AC coupled inputs of the quadrature modulator. Large displacement signals are centred on DC, but this is not always the case for the small displacement situation, and consequently the important DC offset is lost (in the AC coupling).

Currently, the modulator circuit is AC coupled and therefore this electronic implementation is not suited for the small displacement regime. Changes could be made to the electronics to accommodate DC coupled Doppler signals. However, the semi-optical method described in the next section is DC coupled and can decode small displacement signals successfully.

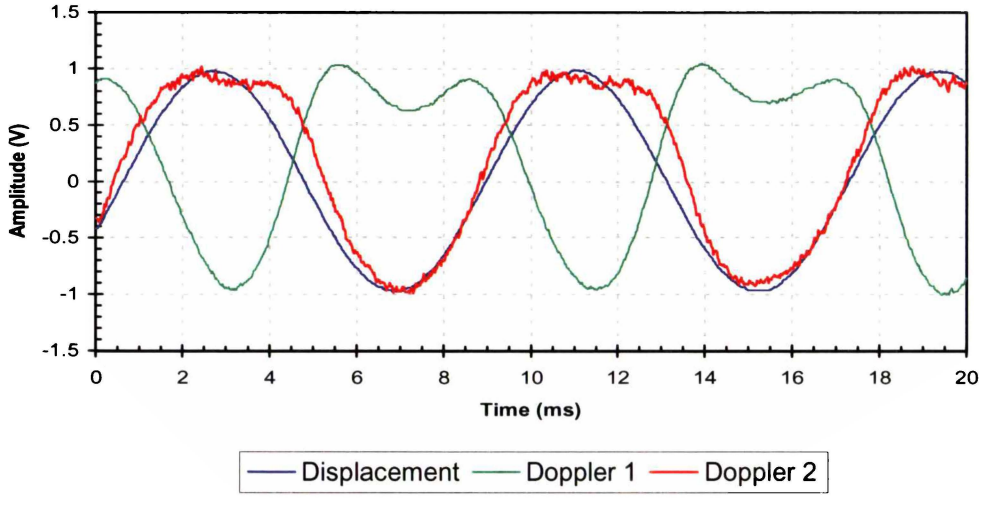

Figure 4.27 – Small displacement Doppler signals obtained from the electronic implementation.

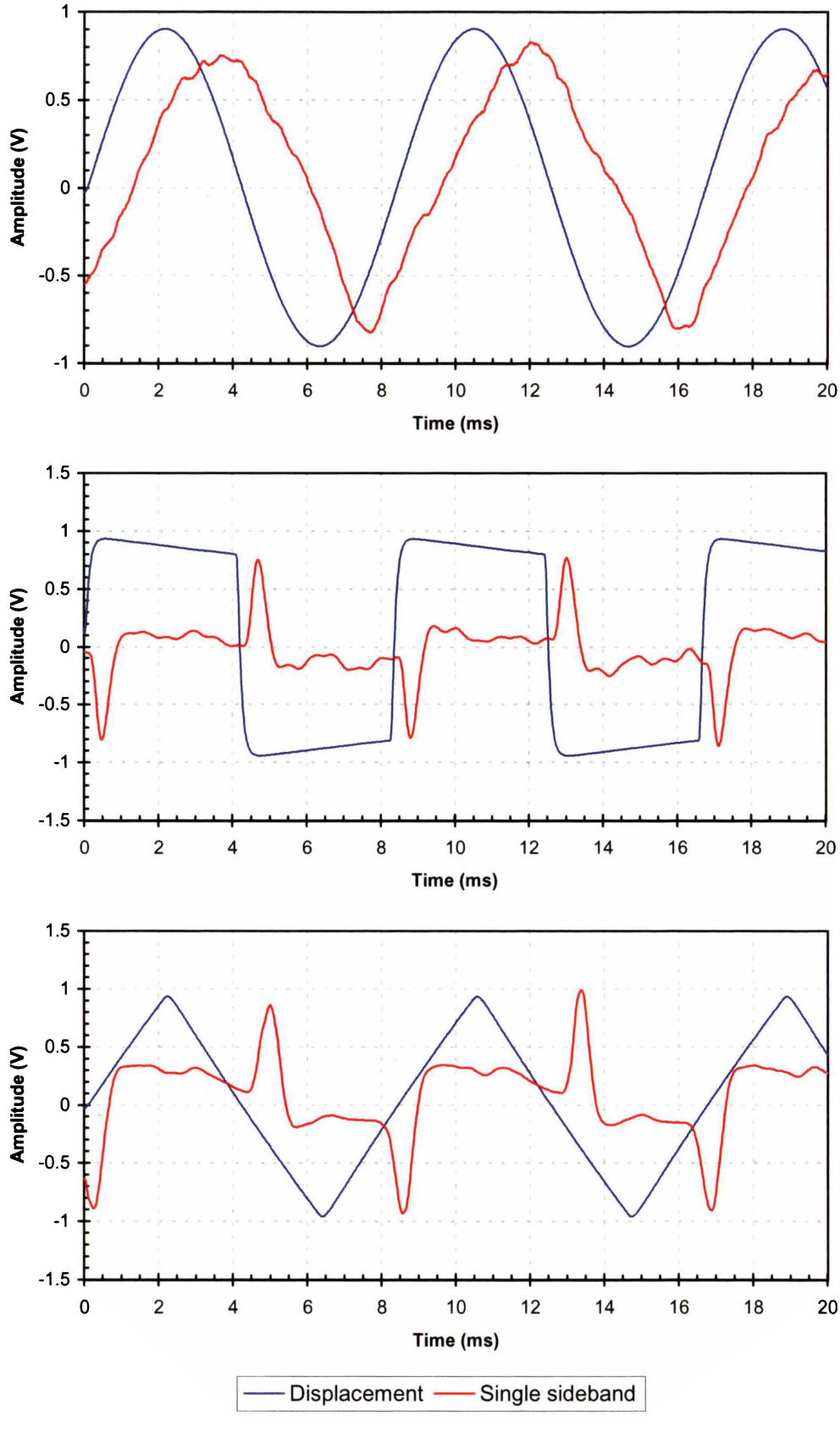

Figure 4.28 – Displacement and decoded velocity waveforms for small displacement sine, square and triangle drives in the electronic implementation.

4.6.2.3. Optical implementation

The optical implementation produces four quadrature Doppler signals, which are illustrated in Figure 4.29. When the modulation is applied to the laser diode the detected signals have this modulation signal superimposed.

Figure 4.30 shows the amplitude modulated signal produced when only one detector is enabled. Also shown here is the double sideband signal generated by differencing two detector outputs, and the single sideband signal produced by summing the two double sideband signals.

Figure 4.31 shows the time sliced modulated signals in the frequency domain. The spectrum of the amplitude modulated signal clearly shows the carrier as the dominant feature. The sidebands are also visible at a lower amplitude, and during time slot 7 are out-of-phase with the carrier causing some cancellation.

In the double sidebands signal the carrier has been cancelled revealing the sidebands, which are also now visible in time slot 7. The spectrum of the single sideband signal once again illustrates direction discrimination, but some of the cancelled sideband is still visible, particularly in time slot 1 and 8. As explained previously in the theory section, the delay line phase shifts the Doppler envelope as well as the carrier signals causing inefficient sideband cancellation. However, in this situation a more likely cause is an imbalance in the double sideband signal amplitudes.

The decoded velocity signals are illustrated in Figure 4.32. These agree with the results obtain with the electronic method, and highlight the same shortcomings of the FM demodulator when compared to the arctangent results.

Like the electronic implementation, small displacement velocity measurements can also be obtained with the optical implementation. However, the DC level is maintained in this method, providing accurate velocity decoding. During the initial differencing any DC offset due to background illumination is cancelled, but the DC associated with the

Doppler signal is preserved. Again, the signals had to be averaged to make them distinguishable from the noise.

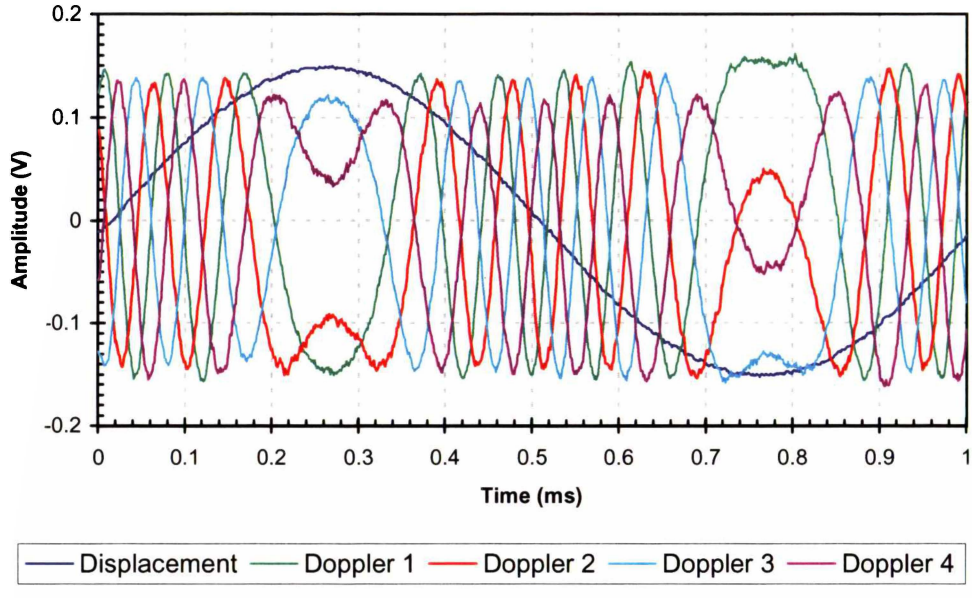

Figure 4.29 – Displacement and Doppler signals produced by the semi-optical implementation.

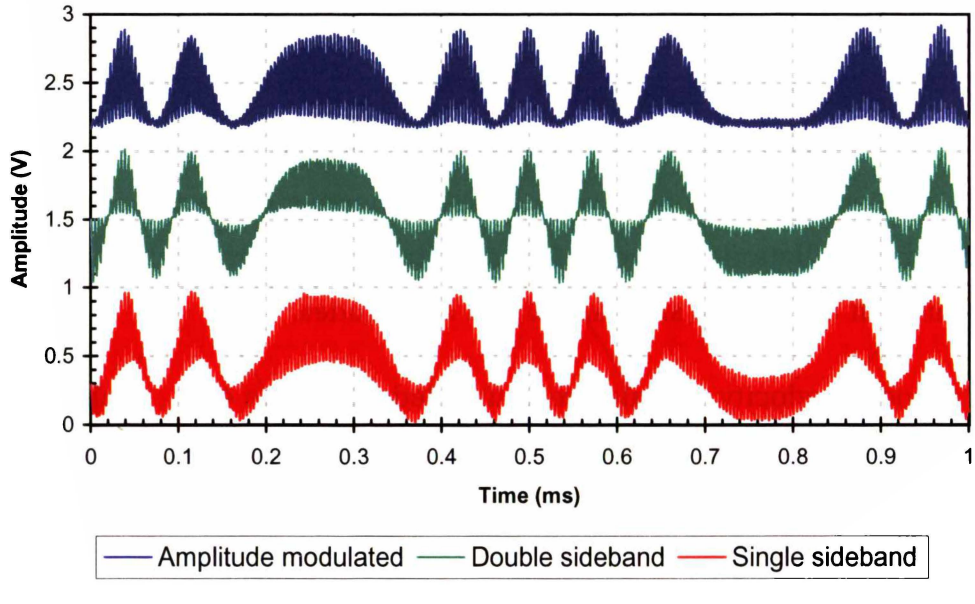

Figure 4.30 – Modulated signals produced by the semi-optical implementation.

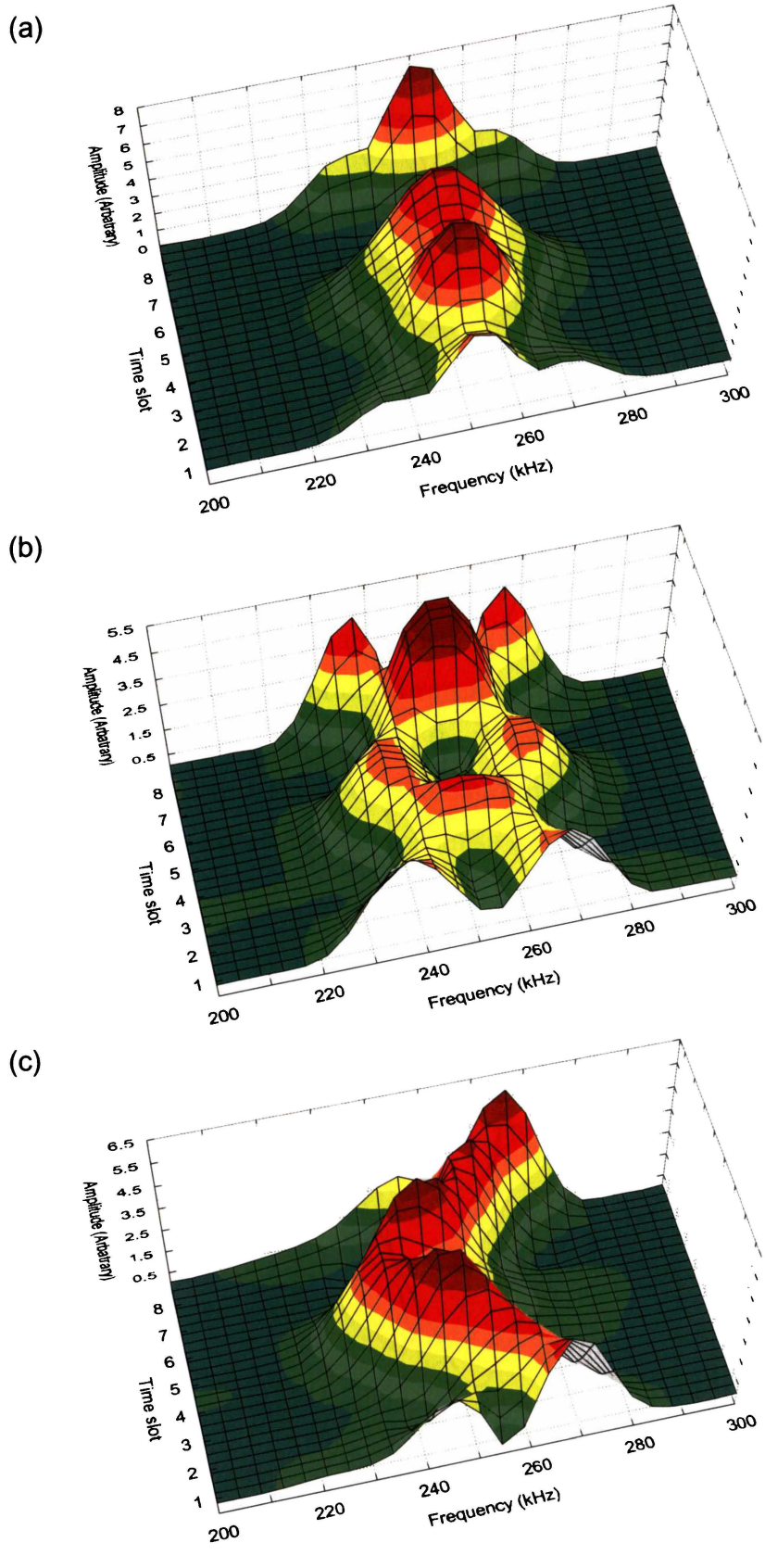

Figure 4.31 – Frequency domain plots from the semi-optical implementation. (a) Amplitude modulated output. (b) Double sideband output. (c) Single sideband output

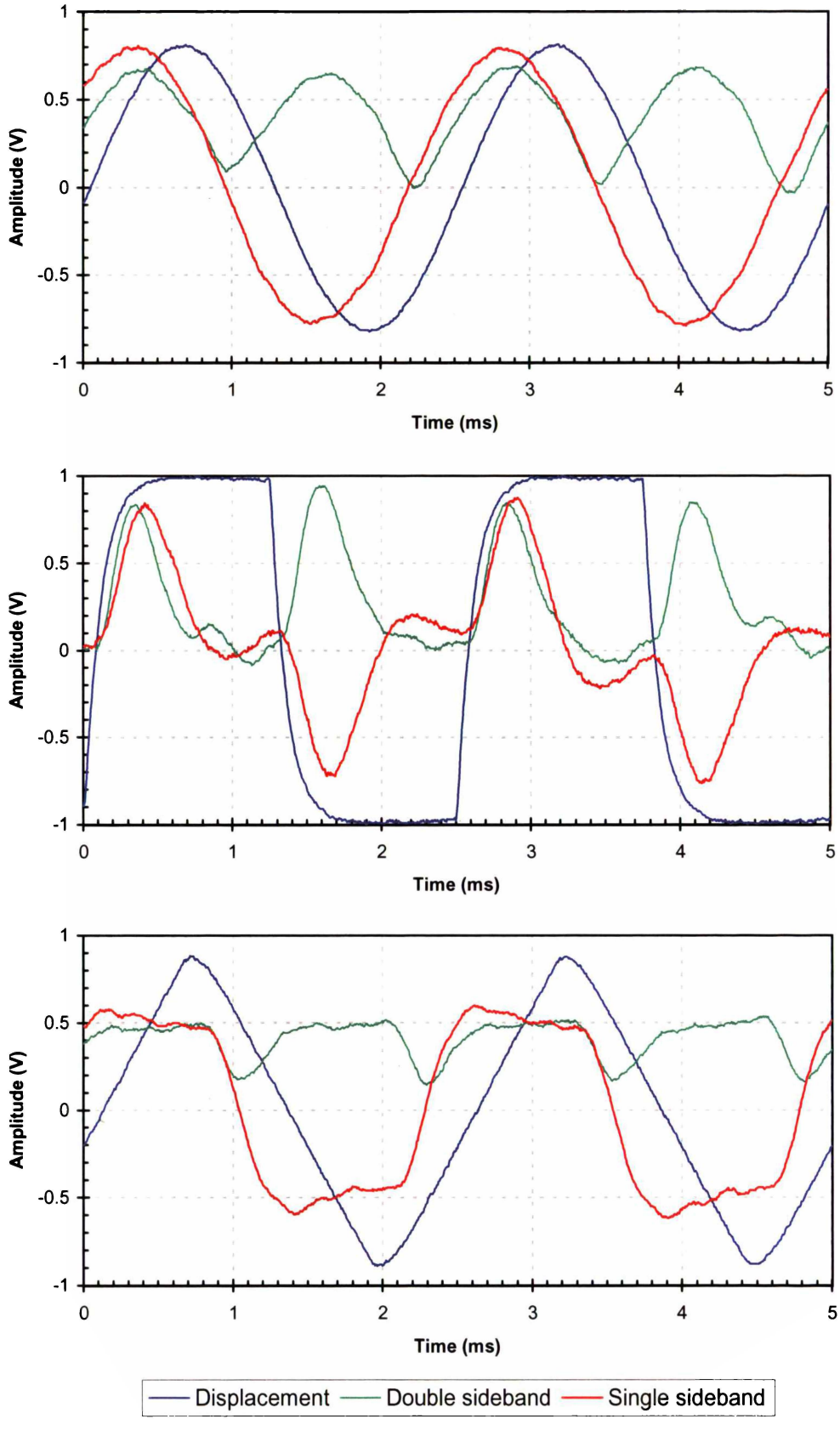

Figure 4.32 – Displacement and decoded velocity for sine, square, and triangle drives signal in the semi-optical implementation.

Two of the four Doppler signals produced by the experiment are shown in Figure 4.33, and the measured results are shown in Figure 4.34. As for the large displacement results, these decoded velocities agree with the electronic implementation.

4.6.2.4. Derived velocity

For the clearest decoded signal, the spectrum analyser used as the FM receiver needed to be adjusted from reading to reading, with the most significant adjustments required for the small displacement signals. The main adjustment was the frequency span, which in terms of FM demodulator operation affects the FM bandwidth and expected deviation.

These adjustments were required because the spectrum analyser is not optimised as an FM receiver, and particularly not for this situation. As a result, the output is not calibrated from measurement to measurement, but for the purposes of this experiment, this does not detract from the results and the concept is still validated. We can however examine one particular situation and calculate the system response in that instance.

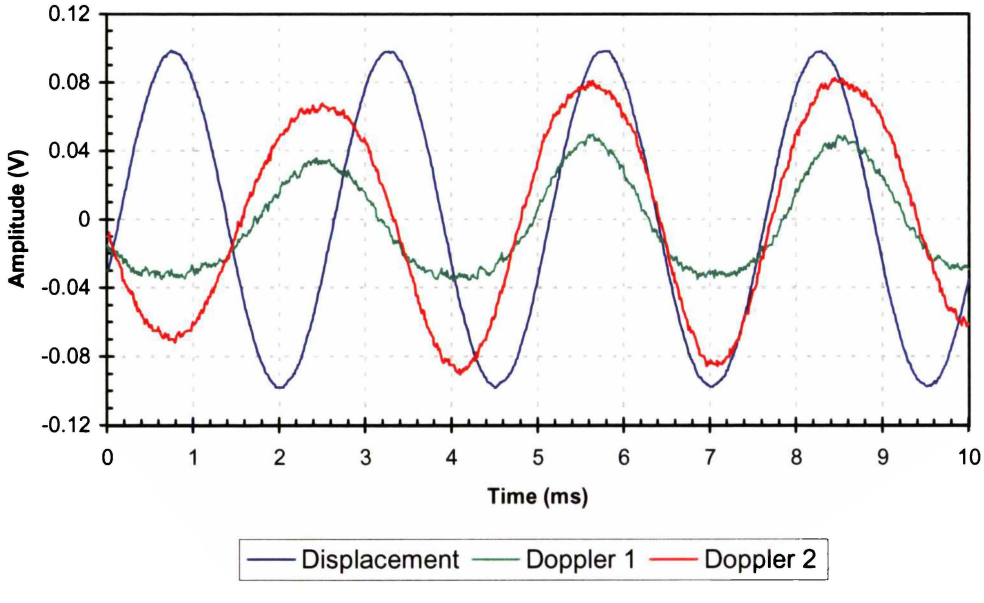

Figure 4.33 – Displacement and small displacement Doppler signals in the semi-optical implementation.

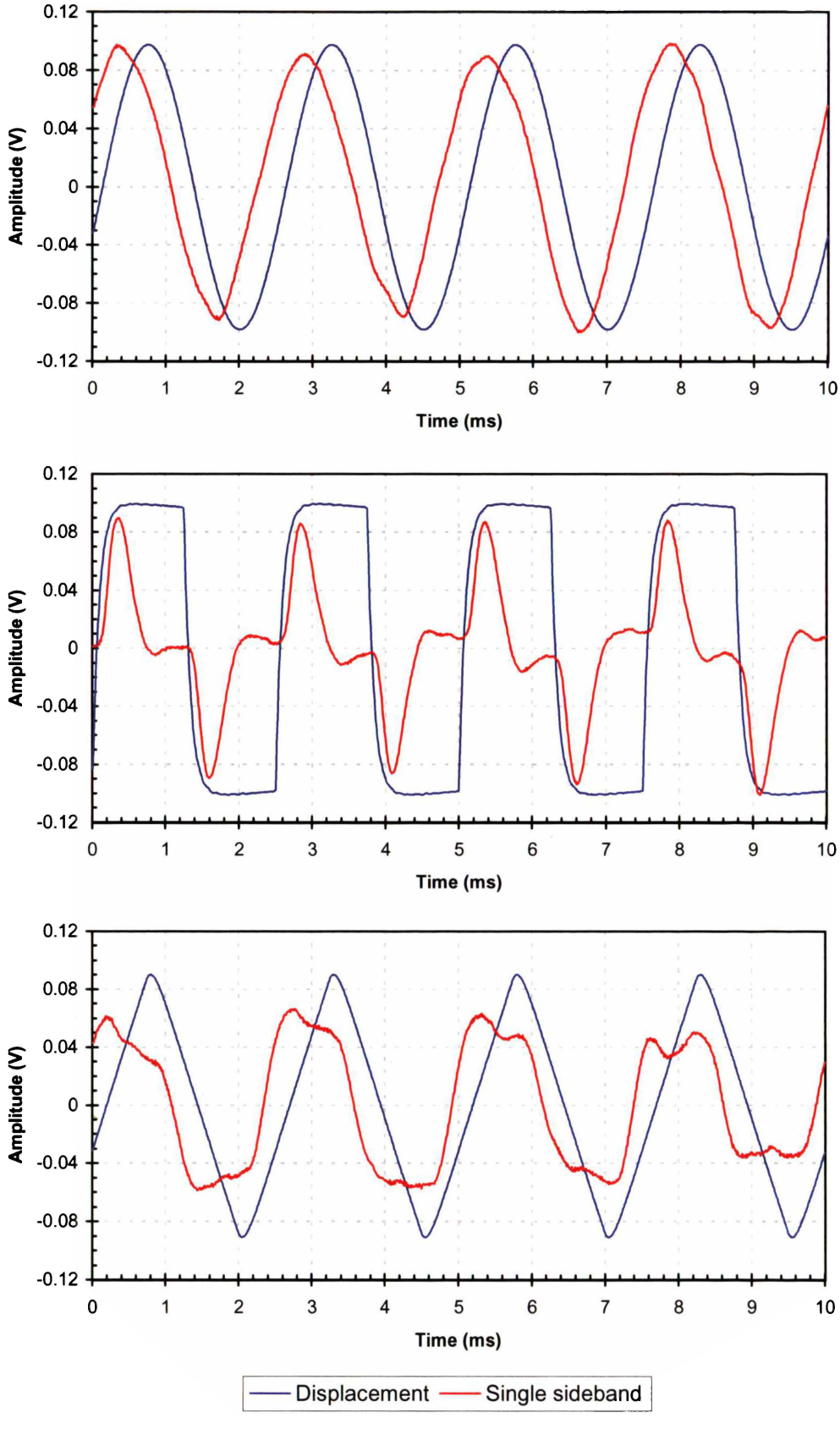

Figure 4.34 – Displacement and averaged decoded velocity for a small displacement sine, square, and triangle drives in the semi-optical implementation.

Consider Figure 4.23 where it can be seen that the Doppler signal completes approximately 4.5 cycles between the positive and negative maximum displacements. Each of these cycles represents one interference fringe and therefore corresponds to a displacement of one wavelength of laser light. The laser diode was temperature stabilised at 25°C causing it to, according to the datasheet, emit at 658 nm. Therefore, the total displacement of the mirror, for a driving signal set to 1 kHz, 10 V, is 2.96 μm.

The actual driving signal on the mirror is less than the set voltage because the signal generator has a 50Ω output. It was measured as 16.6 V peak-to-peak, therefore, the mirror displacement for a given applied voltage is 178 nm/V.

To find the mirror velocity, we need to first consider the driving signal

$$D = A\sin(2\pi ft) \tag{4.39}$$

where A is driving amplitude, f is the driving frequency and t is time. The slew rate, or rate of change of voltage, is the differential of this driving signal with respect to time

$$SR = \frac{dD}{dt} = A\cos(2\pi ft)2\pi f \tag{4.40}$$

At time t=0, a zero crossing occurs corresponding to maximum mirror velocity. The slew rate of the driving signal at this point is

$$SR = 2A\pi f \tag{4.41}$$

For the case in Figure 4.23, the amplitude is 8.3 V peak, and frequency 1 kHz. This causes a slew rate of 52.2 $kV{\cdot}s^{-1}$, which relates to a mirror velocity of 9.29 $mm{\cdot}s^{-1}$ (because the mirror moves 178 nm for every volt applied). At this velocity, the Doppler signal has a frequency of 14.1 kHz, because one cycle is produced for a displacement of one wavelength, and therefore a time period of 70.9 μs. This calculated time period agrees well

will the measured Doppler signal (at a zero crossing of the drive signal) shown in Figure 4.23.

In the case of the 400 Hz sinusoidal drive signal, illustrated in Figure 4.26, the voltage across the mirror is 9.5 V peak. This means the slew rate at zero crossing is 23.9 $kV \cdot s^{-1}$, and the mirror velocity is 4.25 $mm \cdot s^{-1}$. The maximum voltage of the decoded Doppler signal was approximately 1.8 V (scaled in the illustration by 0.5 for convenience), which means the system response is 2.36 $mm \cdot s^{-1} \cdot V^{-1}$.

4.6.3. Limitations

The main factor limiting the accuracy of the decoded velocity measurements is the FM receiver. The spectrum analyser used has a FM demodulation function designed for monitoring radio signals, and as such has a relatively poor quality and bandwidth.

It did however provide a convenient FM receiver that could be tuned to any carrier frequency and adjusted for a variety of frequency deviation levels. A purpose built FM receiver would provide greatly improved velocity output, but would not have the flexibility required for these concept validation experiments.

Another limiting factor is the frequency and mechanical response of the piezo-mounted mirror. The drive frequency had to be kept relatively low, at 400 Hz, to allow the mirror to follow the shape of the driving signal. For example, at higher frequencies no distinction could be made between the results obtained from the sinusoidal and triangular drive signals.

4.7. Conclusion

We have developed a new single sideband modulation method for applying a frequency shift in an LDV system. Two separate implementations of this method, one electronic and one semi-optical, have been presented. Both of these implementations have been explained algebraically, illustrated though numerical simulations, and validated experimentally. For the

experiments, a differencing and summing photodetector circuit, and a quadrature modulator circuit have been designed and constructed. Results were recorded and processed both digitally with the arctangent algorithm, and by analogue electronics with an FM receiver.

The use of an AOM is currently the most common method of generating an offset, as described in Chapter 2. Another modern technique is the use of FM modulated lasers and optical delay lines. The work presented above is the first time that quadrature modulation has been considered as an alternative to these methods. It has the advantages of being applicable to pulsed systems, where FM modulated sources are not suitable, and is much smaller and cheaper to implement than an AOM.

Quadrature demodulation techniques (very similar to quadrature modulation used in single sideband generation) are used as a method of generating two-phase Doppler signals. However, they required a frequency offset to be applied before demodulation and therefore do not provide any size or cost benefits.

Concept validation experiments have been conducted that measure the velocity of a moving mirror in a Michelson interferometer utilising the new single sideband offset generation techniques. These experiments also show how a FM radio receiver can be utilised as a frequency tracking Doppler decoder.

Although frequency tracking techniques are not new, advancing technology has the potential to make such circuits smaller, cheaper and more effective than before. This new technology is in the form of integrated circuits designed to meet the demands of the cellular telephone (and other radio communications) industry.

Despite the inefficiencies of the interferometer collection optics, and limited capabilities of the FM demodulator, velocity measurements have been obtained. These measurements compare favourably to results obtained with the more traditional arctangent method described in the

literature, and prove the validity of the concept. This is true for displacements of several wavelengths (of laser light), and down to less than a wavelength.

With improvements, including a more efficient quadrature mixer such as a 4x4 planar waveguide coupler and the design of a custom FM receiver, these new techniques could be applied to a practical velocimeter. Accurate and reliable velocity measurements of rapidly changing velocity flows could therefore be made cheaply and easily.

Chapter 5
Conclusion

Current designs of lidar systems use expensive and bulky single frequency lasers and acousto-optic modulators, limiting their commercial viability and making them only practical as atmospheric research tools. Two techniques have been presented in this thesis that allow the replacement of the most expensive components with low cost alternatives, leading to lidar systems that are a commercially viable product.

In Chapter 3 a new technique was presented that allows the use of a low coherence laser source for long-range velocity measurements. This technique relies on sampling the transmitted measurement beam and storing it in a ring resonator loop to preserve coherence. A pulse train output is generated, providing the ability to measure velocity at many discrete intervals along the line of measurement beam propagation.

Applied to pulsed Doppler lidar, a storage loop replaces the currently favoured and significantly more expensive injection-locked reference laser. An experimental set-up showed that a Doppler shifted measurement beam can be optically mixed with multiple stored reference pulses. Velocity measurements were obtained that agree with the reference measurements within measurement errors, provided a suitably strong signal was available. These measurements proved the viability of the storage loop concept despite limitations on equipment and time.

The second part of this research, as presented in Chapter 4, showed how a novel application of radio frequency single sideband modulation techniques can be used to provide a frequency offset in an LDV system.

This technique was demonstrated in both electronic and semi-optical implementations. The electronic implementation employs a quadrature modulator circuit, commonly used in radio communications, to shift the Doppler signal from the baseband to a higher frequency band. In the semi-optical implementation, the laser source is amplitude modulated, and the SSB modulation is achieved with a quadrature interferometer, optical delays, and simple differencing and summing electronics. This technique can be used to replace the AOM in both continuous wave, and pulsed velocimetery applications. It has the advantages of being simpler, cheaper, and smaller than an AOM.

In addition, an FM demodulator has been applied as a Doppler signal decoder. Other frequency tracking techniques have been used in the past, but readily available high quality radio frequency componentry has made this type of Doppler processing more attractive than before.

An experiment was performed measuring the velocity of a piezo mounted mirror in a Michelson interferometer. Results obtained with both the electronic and semi-optical methods were compared to results from the standard arctangent processing algorithm. It was shown that the new techniques were capable of determining velocity and direction of motion within the limits of the available equipment. The system was found to respond at $2.36\ \mathrm{mm \cdot s^{-1} \cdot V^{-1}}$, which changed depending on the FM demodulator configuration,

A new lidar design philosophy incorporating some, or all, of the novel techniques presented here would offer significant complexity, cost, size, weight, and power consumption benefits. As a result, lidars could become a commercially viable product for many applications, including early warning systems for clear air turbulence and wind shear detectors. Advanced warning of these phenomena would considerably reduce the risk posed to aircraft and passengers, and hopefully minimise injuries and deaths.

Appendix I Modulated beams mixed on a detector

A sinusoidaly intensity modulated laser beam contains three lines in the frequency spectrum, one at the laser frequency, plus the upper and lower sidebands. When two of these beams mix there are a total of six lines, which produce very lengthy expressions when solving for the detected signal. To avoid this, a new method to derive the detected signal from multiple laser lines incident on a detector was developed. Consider the following 3 lines interfering on a detector

$$a_1 \cdot \exp\left[j(\omega_1 t)\right] + a_2 \cdot \exp\left[j(\omega_2 t)\right] + a_3 \exp\left[j(\omega_3 t)\right]$$

where t is time, a is the amplitude, and ω is the frequency of each line.

Finding the magnitude squared (with a little help from Mathcad) produces the detected phtotcurrent

$$\begin{aligned} &a_1^2 + a_2^2 + a_3^2 + 2a_1a_2\cos(\omega_1 t)\cos(\omega_2 t) + 2a_1a_2\sin(\omega_1 t)\sin(\omega_2 t) \\ &+2a_1a_3\cos(\omega_1 t)\cos(\omega_3 t) + 2a_1a_2\sin(\omega_1 t)\sin(\omega_3 t) \\ &+2a_2a_3\cos(\omega_2 t)\cos(\omega_3 t) + 2a_2a_3\sin(\omega_2 t)\sin(\omega_3 t) \end{aligned}$$

With the aid of simple trigonometric identities, this simplifies to

$$a_1^2 + a_2^2 + a_3^2 + 2a_1a_2\cos(\omega_1 t - \omega_2 t) + 2a_1a_3\cos(\omega_1 t - \omega_3 t) + 2a_2a_3\cos(\omega_2 t - \omega_3 t)$$

Notice that the DC component is the sum of each individual amplitude squared, and the time varying components are the beat between each individual line with each other line once.

The same result can therefore be achieved by summing:

- the square of the amplitudes,

$$a_1^2 + a_2^2 + a_3^2$$

- line 1 beating with line 2,

$$2a_1a_2\cos(\omega_1 t - \omega_2 t)$$

- line 1 beating with line 3,

$$2a_1a_3\cos(\omega_1 t - \omega_3 t)$$

- and line 2 beating with line 3.

$$2a_2a_3\cos(\omega_2 t - \omega_3 t)$$

This principle can be applied to find the signal resulting when the two modulated beams in the optical implementation of SSB frequency shifting experiment are detected. In this case there is a total of six laser lines (three for the reference beam and three for the Doppler shifted beam) represented by

$$a\cdot\exp\left[j(\omega t)\right]$$
$$\frac{1}{2}ab\cdot\exp\left[j(\omega t+\Omega t)\right]$$
$$\frac{1}{2}ab\cdot\exp\left[j(\omega t-\Omega t)\right]$$
$$c\cdot\exp\left[j(\omega t+\Delta\omega t+\Delta\varphi)\right]$$
$$\frac{1}{2}cb\cdot\exp\left[j(\omega t+\Delta\omega t+\Omega t+\Delta\varphi)\right]$$
$$\frac{1}{2}cb\cdot\exp\left[j(\omega t+\Delta\omega t-\Omega t+\Delta\varphi)\right]$$

where ω is the laser frequency, Ω is the modulating frequency, $\Delta\omega$ is the Doppler shift, $\Delta\varphi$ is the phase shift, and t is time.

The result of each line interfering with each other, and these results collected on frequency is shown in the following tables, and the final result is

$$a^2+c^2+\frac{1}{2}a^2b^2+\frac{1}{2}c^2b^2+ac\left(2+b^2\right)\cos\left(\Delta\omega t+\Delta\varphi\right)$$
$$+2b\left(a^2+c^2\right)\cos\left(\Omega t\right)+2abc\cos\left(\Omega t+\Delta\omega t+\Delta\varphi\right)+2abc\cos\left(\Omega t-\Delta\omega t-\Delta\varphi\right)$$
$$+\frac{1}{2}b^2\left(a^2+c^2\right)\cos\left(2\Omega t\right)+\frac{1}{2}ab^2c\cos\left(2\Omega t+\Delta\omega t+\Delta\varphi\right)+\frac{1}{2}ab^2c\cos\left(2\Omega t-\Delta\omega t-\Delta\varphi\right)$$

Table of results collected on frequency.

Spectral lines	Detected beat signal	Simplified beat signal
$a \cdot \exp\left[j(\omega t)\right]$		
$\frac{1}{2}ab \cdot \exp\left[j(\omega t + \Omega t)\right]$	$a^2 + \frac{1}{4}a^2b^2 + a^2b \cdot \cos\left(\omega t - (\omega t + \Omega t)\right)$	$a^2 + \frac{1}{4}a^2b^2 + a^2b \cdot \cos\left(\Omega t\right)$
$\frac{1}{2}ab \cdot \exp\left[j(\omega t - \Omega t)\right]$	$a^2 + \frac{1}{4}a^2b^2 + a^2b \cdot \cos\left(\omega t - (\omega t - \Omega t)\right)$	$a^2 + \frac{1}{4}a^2b^2 + a^2b \cdot \cos\left(\Omega t\right)$
$c \cdot \exp\left[j(\omega t + \Delta\omega t + \Delta\varphi)\right]$	$a^2 + c^2 + 2ac \cdot \cos\left(\omega t - (\omega t + \Delta\omega t + \Delta\varphi)\right)$	$a^2 + c^2 + 2ac \cdot \cos\left(\Delta\omega t + \Delta\varphi\right)$
$\frac{1}{2}cb \cdot \exp\left[j(\omega t + \Delta\omega t + \Omega t + \Delta\varphi)\right]$	$a^2 + \frac{1}{4}c^2b^2 + abc \cdot \cos\left(\omega t - (\omega t + \Delta\omega t + \Omega t + \Delta\varphi)\right)$	$a^2 + \frac{1}{4}c^2b^2 + abc \cdot \cos\left(\Omega t + \Delta\omega t + \Delta\varphi\right)$
$\frac{1}{2}cb \cdot \exp\left[j(\omega t + \Delta\omega t - \Omega t + \Delta\varphi)\right]$	$a^2 + \frac{1}{4}c^2b^2 + abc \cdot \cos\left(\omega t - (\omega t + \Delta\omega t - \Omega t + \Delta\varphi)\right)$	$a^2 + \frac{1}{4}c^2b^2 + abc \cdot \cos\left(\Omega t - \Delta\omega t - \Delta\varphi\right)$
$\frac{1}{2}ab \cdot \exp\left[j(\omega t + \Omega t)\right]$		
$\frac{1}{2}ab \cdot \exp\left[j(\omega t - \Omega t)\right]$	$\frac{1}{4}a^2b^2 + \frac{1}{4}a^2b^2 + \frac{1}{2}a^2b^2 \cdot \cos\left((\omega t + \Omega t) - (\omega t - \Omega t)\right)$	$\frac{1}{2}a^2b^2 + \frac{1}{2}a^2b^2 \cdot \cos\left(2\Omega t\right)$
$c \cdot \exp\left[j(\omega t + \Delta\omega t + \Delta\varphi)\right]$	$\frac{1}{4}a^2b^2 + c^2 + abc \cdot \cos\left((\omega t + \Omega t) - (\omega t + \Delta\omega t + \Delta\varphi)\right)$	$\frac{1}{4}a^2b^2 + c^2 + abc \cdot \cos\left(\Omega t - \Delta\omega t - \Delta\varphi\right)$
$\frac{1}{2}cb \cdot \exp\left[j(\omega t + \Delta\omega t + \Omega t + \Delta\varphi)\right]$	$\frac{1}{4}a^2b^2 + \frac{1}{4}c^2b^2 + \frac{1}{2}ab^2c \cdot \cos\left((\omega t + \Omega t) - (\omega t + \Delta\omega t + \Omega t + \Delta\varphi)\right)$	$\frac{1}{4}a^2b^2 + \frac{1}{4}c^2b^2 + \frac{1}{2}ab^2c \cdot \cos\left(\Delta\omega t + \Delta\varphi\right)$
$\frac{1}{2}cb \cdot \exp\left[j(\omega t + \Delta\omega t - \Omega t + \Delta\varphi)\right]$	$\frac{1}{4}a^2b^2 + \frac{1}{4}c^2b^2 + \frac{1}{2}ab^2c \cdot \cos\left((\omega t + \Omega t) - (\omega t + \Delta\omega t - \Omega t + \Delta\varphi)\right)$	$\frac{1}{4}a^2b^2 + \frac{1}{4}c^2b^2 + \frac{1}{2}ab^2c \cdot \cos\left(2\Omega t - \Delta\omega t - \Delta\varphi\right)$
$\frac{1}{2}ab \cdot \exp\left[j(\omega t - \Omega t)\right]$		
$c \cdot \exp\left[j(\omega t + \Delta\omega t + \Delta\varphi)\right]$	$\frac{1}{4}a^2b^2 + c^2 + abc \cdot \cos\left((\omega t - \Omega t) - (\omega t + \Delta\omega t + \Delta\varphi)\right)$	$\frac{1}{4}a^2b^2 + c^2 + abc \cdot \cos\left(\Omega t + \Delta\omega t + \Delta\varphi\right)$
$\frac{1}{2}cb \cdot \exp\left[j(\omega t + \Delta\omega t + \Omega t + \Delta\varphi)\right]$	$\frac{1}{4}a^2b^2 + \frac{1}{4}c^2b^2 + \frac{1}{2}ab^2c \cdot \cos\left((\omega t - \Omega t) - (\omega t + \Delta\omega t + \Omega t + \Delta\varphi)\right)$	$\frac{1}{4}a^2b^2 + \frac{1}{4}c^2b^2 + \frac{1}{2}ab^2c \cdot \cos\left(2\Omega t + \Delta\omega t + \Delta\varphi\right)$
$\frac{1}{2}cb \cdot \exp\left[j(\omega t + \Delta\omega t - \Omega t + \Delta\varphi)\right]$	$\frac{1}{4}a^2b^2 + \frac{1}{4}c^2b^2 + \frac{1}{2}ab^2c \cdot \cos\left((\omega t - \Omega t) - (\omega t + \Delta\omega t - \Omega t + \Delta\varphi)\right)$	$\frac{1}{4}a^2b^2 + \frac{1}{4}c^2b^2 + \frac{1}{2}ab^2c \cdot \cos\left(\Delta\omega t + \Delta\varphi\right)$
$c \cdot \exp\left[j(\omega t + \Delta\omega t + \Delta\varphi)\right]$		
$\frac{1}{2}cb \cdot \exp\left[j(\omega t + \Delta\omega t + \Omega t + \Delta\varphi)\right]$	$c^2 + \frac{1}{4}c^2b^2 + c^2b \cdot \cos\left((\omega t + \Delta\omega t + \Delta\varphi) - (\omega t + \Delta\omega t + \Omega t + \Delta\varphi)\right)$	$c^2 + \frac{1}{4}c^2b^2 + c^2b \cdot \cos\left(\Omega t\right)$
$\frac{1}{2}cb \cdot \exp\left[j(\omega t + \Delta\omega t - \Omega t + \Delta\varphi)\right]$	$c^2 + \frac{1}{4}c^2b^2 + c^2b \cdot \cos\left((\omega t + \Delta\omega t + \Delta\varphi) - (\omega t + \Delta\omega t - \Omega t + \Delta\varphi)\right)$	$c^2 + \frac{1}{4}c^2b^2 + c^2b \cdot \cos\left(\Omega t\right)$
$\frac{1}{2}cb \cdot \exp\left[j(\omega t + \Delta\omega t + \Omega t + \Delta\varphi)\right]$		
$\frac{1}{2}cb \cdot \exp\left[j(\omega t + \Delta\omega t - \Omega t + \Delta\varphi)\right]$	$\frac{1}{4}c^2b^2 + \frac{1}{4}c^2b^2 + \frac{1}{2}c^2b^2 \cdot \cos\left((\omega t + \Delta\omega t + \Omega t + \Delta\varphi) - (\omega t + \Delta\omega t - \Omega t + \Delta\varphi)\right)$	$\frac{1}{2}c^2b^2 + \frac{1}{2}c^2b^2 \cdot \cos\left(2\Omega t\right)$

Frequency term	Collected coefficients	Simplified coefficient
DC	$a^2+c^2+\frac{1}{4}a^2b^2+\frac{1}{4}a^2b^2+\frac{1}{4}c^2b^2+\frac{1}{4}c^2b^2$	$a^2+c^2+\frac{1}{2}a^2b^2+\frac{1}{2}c^2b^2$
$\cos(\Delta\omega t+\Delta\varphi)$	$2ac+\frac{1}{2}ab^2c+\frac{1}{2}ab^2c$	$ac(2+b^2)$
$\cos(\Omega t)$	$a^2b+a^2b+c^2b+c^2b$	$2b(a^2+c^2)$
$\cos(\Omega t+\Delta\omega t+\Delta\varphi)$	$abc+abc$	$2abc$
$\cos(\Omega t-\Delta\omega t-\Delta\varphi)$	$abc+abc$	$2abc$
$\cos(2\Omega t)$	$\frac{1}{2}a^2b^2+\frac{1}{2}c^2b^2$	$\frac{1}{2}b^2(a^2+c^2)$
$\cos(2\Omega t+\Delta\omega t+\Delta\varphi)$	$\frac{1}{2}ab^2c$	$\frac{1}{2}ab^2c$
$\cos(2\Omega t-\Delta\omega t-\Delta\varphi)$	$\frac{1}{2}ab^2c$	$\frac{1}{2}ab^2c$

Table of results collected on frequency.

Appendix II Storage loop simulation code

The storage loop simulation was performed in Matlab, using the following code.

```
% This program simulates the storage loop experiment
%
% Adrian Dorrington
% March 2000

% Define the number of data points per picosecond
ppns = 100;

% Define the delays between nodes
D1=26*ppns;
D2=41*ppns;
D3=13*ppns;
D4=13*ppns;
D5=13*ppns;
D6=13*ppns;
D7=4*ppns;
D8=4*ppns;
D9=13*ppns;
D10=13*ppns;
D11=13*ppns;
D12=13*ppns;
D13=15*ppns;

% Define the refelctions
InRefl = 0.2;
DetRefl = 0.2;
Refl = 0.1;
Trans = 0.99;

% Define the input signals
InputMeas(0:500*ppns) = 0;
InputRef(0:500*ppns) = 0;
a=100*ppns:160*ppns;
InputMeas(a) = sin((a-(100*ppns))/(60*ppns) * pi).^2 .* exp(i*2*pi*12.5*(a-
        (100*ppns))/ppns) .* .3;
InputRef(a) = sin((a-(100*ppns))/(60*ppns) * pi).^2 .* exp(i*2*pi*12.76*(a-
        (100*ppns))/ppns);

% Initalise a starting period of no signals
P(0:500*ppns,1:52) = 0;

% perfom the simulation
for t=100*ppns+1:500*ppns
  P(t,2) = P(t-D1,4);
  P(t,1) = InputMeas(t)+P(t-4,2)*InRefl;
  P(t,3) = P(t-D1,1);
  P(t,6) = P(t-D2,8);
  P(t,4) = P(t,6)*Trans+P(t-4,3)*Refl;
  P(t,5) = P(t,3)*Trans+P(t-4,6)*Refl;
  P(t,7) = P(t-D2,5);
  P(t,10) = P(t-D3,38);
  P(t,8) = P(t,10)*Trans+P(t-4,7)*Refl;
  P(t,9) = P(t,7)*Trans+P(t-4,10)*Refl;
  P(t,11) = P(t-D5,39);
```

```
  P(t,18) = P(t-D7,24);
  P(t,12) = P(t,18)*Trans+P(t-4,11)*Refl;
  P(t,13) = P(t-D6,43);
  P(t,20) = P(t-D8,26);
  P(t,14) = P(t,20)*Trans+P(t-4,13)*Refl;
  P(t,16) = P(t-D4,42);
  P(t,21) = P(t-D10,47);
  P(t,15) = P(t,21)*Trans+P(t-4,16)*Refl;
  P(t,17) = P(t,11)*Trans+P(t-4,18)*Refl;
  P(t,19) = P(t,13)*Trans+P(t-4,20)*Refl;
  P(t,22) = P(t,16)*Trans+P(t-4,21)*Refl;
  P(t,23) = P(t-D7,17);
  P(t,24) = P(t-4,23)*DetRefl;
  P(t,25) = P(t-D8,19);
  P(t,26) = P(t-4,25)*DetRefl;
  P(t,28) = P(t-D9,46);
  P(t,27) = InputRef(t)+P(t-4,28)*InRefl;
  P(t,29) = P(t-D11,51);
  P(t,32) = P(t-D13,34);
  P(t,30) = P(t,32)*Trans+P(t-4,29)*Refl;
  P(t,31) = P(t,29)*Trans+P(t-4,32)*Refl;
  P(t,33) = P(t-D13,31);
  P(t,36) = P(t-D12,50);
  P(t,34) = P(t,36)*Trans+P(t-4,33)*Refl;
  P(t,35) = P(t,33)*Trans+P(t-4,36)*Refl;
  P(t,37) = P(t-D3,9);
  P(t,40) = P(t-D5,12);
  P(t,44) = P(t-D6,14);
  P(t,38) = P(t,40)*0.707+P(t-2,44)*0.707;
  P(t,41) = P(t-D4,15);
  P(t,39) = P(t,37)*0.707+P(t-2,41)*0.707;
  P(t,42) = P(t-2,40)*0.707+P(t,44)*0.707;
  P(t,43) = P(t-2,37)*0.707+P(t,41)*0.707;
  P(t,45) = P(t-D9,27);
  P(t,48) = P(t-D10,22);
  P(t,52) = P(t-D11,30);
  P(t,46) = P(t,48)*0.707+P(t-2,52)*0.707;
  P(t,49) = P(t-D12,35);
  P(t,47) = P(t,45)*0.707+P(t-2,49)*0.707;
  P(t,50) = P(t-2,48)*0.707+P(t,52)*0.707;
  P(t,51) = P(t-2,45)*0.707+P(t,49)*0.707;

  % Report progress
  if mod(t,100) == 0
    fprintf ('%d / %d\n', t, 500*ppns);
  end
end

% Write data files for each node
for f=1:52
  filename = sprintf('.\\newstoresim\\ressqr%02d.csv', f);

  P(:,f) = abs(P(:,f)) .^ 2;
  outfile = fopen (filename, 'w');
  fprintf (outfile, '%f\n', P(:,f));
  fclose (outfile);
end;
```

Appendix III Storage loop data processing code

The storage loop data processing was performed in Matlab, using the following code.

```
% This program accepts data from the scope and
% proceses it to deterimne velocity
% FFT's are averaged and frequency is determind by
% locating the peak, for each rotation speed of the motor.
%
% Adrian Dorrington
% August 1999

% Set up colours for plots
col = ['y' 'm' 'c' 'r' 'g'];

% Clear data
clear avgs;

% Start loop to process each measurement range
for pulseno = 0:3

  % decide which centre frequency to use
  if pulseno == 2
    line = 260;
  else
    line = 180;
  end;

  % Define directory for data file
  d = sprintf('o:/mydocu~1/adrian/research/measur~1/pulse%d~1/', pulseno);
  fprintf ('%s\n', d);

  % clear data
  clear r2;

  % Start loop for each velocity at a particular range
  for freqno=0:9

    % Display progress
    fprintf ('%d : ',freqno);

    % Start loop for each measurement at a particular velocity
    for fileno=0:9

      % Establish file name for data
      if (freqno<10)
        filename = strcat(d,
          'dat000',int2str(freqno),int2str(fileno),'.csv');
      else
        filename = strcat(d, 'dat00',int2str(freqno),int2str(fileno),'.csv');
      end;

      % Display progress
      fprintf ('%d ',fileno);

      % Read data file
      infile = fopen (filename);
      a = fscanf(infile, '%f');
```

```
  fclose (infile);

  % Find number of points
  N = length(a);
  i=0:1:N-1;

  % Remove DC component
  DC = mean(a);
  a = a - DC;

  % Apply blackman window
  a = a.*blackman(N);

  % Autocorrelate
  a = xcorr (a);
  a(end+1)=0;

  % Find new number of points
  N = length(a);
  i=0:1:N-1;

  % Perform FFT
  clear b;
  G = 4;
  b = fft (a, N*G);
  k=0:1:(N*G)/2;
  c = abs(b(k+1));

  % Accumulate spectrums
  if fileno == 0
    avgs = c;
  else
    avgs = avgs + c;
  end;

end;

% Average spectrums
c = avgs / 10;

% Plot result
figure(freqno+1);
plot (k,avgs);

% Find maximum value
if line == 260
   m = max(c(25*G:end));
else
   m = max(c(10*G:23*G));
end;

% Determine frequency at max point
f=find(c==m);

% Display progress
fprintf ('%f  %fMHz  ',f/G,f/G/N*2*2500);

% Estimate noise level
noise = mean(c(40:end))*sqrt(length(c)-40);
m = m * sqrt(840);
ston = m/noise;
```

```
    fprintf ('%f\n', 20*log10(ston));

    % Determine velocity
    r=f/G/N*2*2500;
    if (freqno == 0)
      offset = r;
      rad = 0;
      radcount = 0;
      tston = ston;
    else
      rad=rad+((r-offset)/2.234/(freqno*50)/3.141592/2);
      radcount = radcount+1;
      tston = tston + ston;
    end;
    if line == 260
      r=r-offset;
    else
      r=offset-r;
    end;
    r=r/2.234;

    % Store velocity
    r2(freqno+1)=r;

  end;

  % Graph results
  fr=0:50:freqno*50;
  figure(freqno+2);

  if rad > 0
    r2=-r2;
  end;
  if pulseno == 0
    hold off;
  end;
  fprintf('Colour %d is %s\n', pulseno+1, col(pulseno+1));
  plot(fr,r2,col(pulseno+1));
  hold on;

  tston = tston / 10;

  % Display results
  rad = rad / radcount;
  fprintf ('Radius = %fmm   S/N = %fdB\n', rad*1000, 20*log10(tston));

  % Write results to file
  filename = sprintf ('res%d.csv', pulseno);
  outfile = fopen (filename, 'w');
  fprintf (outfile, '%f\n', r2);
  fclose (outfile);

end;
```

Appendix IV Time sliced FFT

The SSB frequency shift time sliced FFT processing was performed in Matlab, using the following code.

```
% This program reads data files from the scope then
% splits them onto 8 even blocks and performs an
% FFT on each block
%
% Adrian Dorrington
% June 2000

% Clear all variables
clear;

% Find number of points in each blocs
N=ceil(1000/8);
% Find total blocks
Blocks = ceil(1000/N);

% Load data files

infile = fopen ('mod1.csv');
a1 = fscanf(infile, '%f', [N,Blocks]);
fclose (infile);

infile = fopen ('mod2.csv');
a2 = fscanf(infile, '%f', [N,Blocks]);
fclose (infile);

infile = fopen ('mod3.csv');
a3 = fscanf(infile, '%f', [N,Blocks]);
fclose (infile);

infile = fopen ('mod4.csv');
a4 = fscanf(infile, '%f', [N,Blocks]);
fclose (infile);

infile = fopen ('mod5.csv');
a5 = fscanf(infile, '%f', [N,Blocks]);
fclose (infile);

%set up blackman matrix
Id(1,1:Blocks)=1;
Blk2 = blackman(N)*Id;

% Define number of points in FFT
M = 1000;

% Process mod1 file
a=a1;
a=a.*Blk2;
b = fft(a, M);
c=abs(b);

% Write results to data file
outfile = fopen ('fft1.csv', 'w');
```

```
for f=1:M/2
  fprintf (outfile, '%f,', 1000000/M*f);
  fprintf (outfile, '%f,', c(f,1:Blocks-1));
  fprintf (outfile, '%f\n', c(f,Blocks));
end
fclose (outfile);

% Process mod2 file
a=a2;
a=a.*Blk2;
b = fft(a, M);
c=abs(b);

% Write results to data file
outfile = fopen ('fft2.csv', 'w');
for f=1:M/2
  fprintf (outfile, '%f,', 1000000/M*f);
  fprintf (outfile, '%f,', c(f,1:Blocks-1));
  fprintf (outfile, '%f\n', c(f,Blocks));
end
fclose (outfile);

% Process mod3 file
a=a3;
a=a.*Blk2;
b = fft(a, M);
c=abs(b);

% Write results to data file
outfile = fopen ('fft3.csv', 'w');
for f=1:M/2
  fprintf (outfile, '%f,', 1000000/M*f);
  fprintf (outfile, '%f,', c(f,1:Blocks-1));
  fprintf (outfile, '%f\n', c(f,Blocks));
end
fclose (outfile);

% Process mod4 file
a=a4;
a=a.*Blk2;
b = fft(a, M);
c=abs(b);

% Write results to data file
outfile = fopen ('fft4.csv', 'w');
for f=1:M/2
  fprintf (outfile, '%f,', 1000000/M*f);
  fprintf (outfile, '%f,', c(f,1:Blocks-1));
  fprintf (outfile, '%f\n', c(f,Blocks));
end
fclose (outfile);

% Process mod5 file
a=a5;
a=a.*Blk2;
b = fft(a, M);
c=abs(b);

% Write results to data file
outfile = fopen ('fft5.csv', 'w');
for f=1:M/2
```

```
  fprintf (outfile, '%f,', 1000000/M*f);
  fprintf (outfile, '%f,', c(f,1:Blocks-1));
  fprintf (outfile, '%f\n', c(f,Blocks));
end
fclose (outfile);
```

Appendix V Arctangent processing

The arctangent processing used for the SSB frequency shift comparison was performed in Matlab using the following code.

```
% This program reads data files from the scope and
% performs arctanget processing to calculate displacement
% and velocity
%
% Adrian Dorrington
% July 2000

% Define files numbers to load
FileNum=[74 107 80];

% Repeat for each set of files to process
for fileno=1:3

  % Display current set number
  fprintf ('%d\n', fileno);

  % Read displacement data
  filename = sprintf ('o:\\My Documents\\Adrian\\Research\\modulation
         interferometer\\200um fiber\\Scope measurements\\Tek00%03d.csv',
         FileNum(fileno));
  infile = fopen (filename);
  a1 = fscanf(infile, '%f,%f\n',[2, 1000]);
  fclose (infile);

  % Read Doppler data 1
  filename = sprintf ('o:\\My Documents\\Adrian\\Research\\modulation
         interferometer\\200um fiber\\Scope measurements\\Tek00%03d.csv',
         FileNum(fileno)+1);
  infile = fopen (filename);
  a2 = fscanf(infile, '%f,%f\n',[2, 1000]);
  fclose (infile);

  % Read Doppler data 2
  filename = sprintf ('o:\\My Documents\\Adrian\\Research\\modulation
         interferometer\\200um fiber\\Scope measurements\\Tek00%03d.csv',
         FileNum(fileno)+2);
  infile = fopen (filename);
  a3 = fscanf(infile, '%f,%f\n',[2, 1000]);
  fclose (infile);

  % make sure signals have no DC offset
  dc = (max(a2(2,:))+min(a2(2,:)));
  a2(2,:) = a2(2,:) - dc/2;
  dc = (max(a3(2,:))+min(a3(2,:)));
  a3(2,:) = a3(2,:) - dc/2;

  %make sure signals are the same amplitude
  scale = max(a2(2,:))/max(a3(2,:));
  a3(2,:) = a3(2,:)*scale;

  % Plot Doppler signals
  pt(1,:)=a2(2,:);
```

```
pt(2,:)=a3(2,:);
figure (1);
plot (pt');

% Perform arctangent
p(1,:) = a2(1,:);
p(2,:) = a1(2,:);
p(3,:) = atan(a2(2,:)./a3(2,:));

% Plot arctangent result
figure (2);
plot (p(3,100:200)');

% Generate offset signal
o(1)=0;
for f=2:1000
  o(f)=o(f-1);
  if (p(3,f)-p(3,f-1)) > 1.2
    o(f)=o(f)-pi;
  end
  if (p(3,f)-p(3,f-1)) < -1.2
    o(f)=o(f)+pi;
  end
end

% Plot offset signal
figure (3);
plot (o(100:200));

% Write offset data for file number 1 only
q(1,:)=p(1,:);
q(2,:)=p(3,:);
q(3,:)=o;
if fileno == 1
  outfile = fopen ('arctan.csv', 'w');
  fprintf (outfile, '%f,%f,%f\n', q);
  fclose (outfile);
end


% Apply offset to arctangent
p(3,:) = p(3,:)+o;

% Filter result to reduce noise
for f=2:999
  p(3,f)=p(3,f-1)+(p(3,f)-p(3,f-1))*.2;
end

% Differentiate to derive velocity
for f=1:999
  p(4,f)=p(3,f+1)-p(3,f);
end

% Filter velocity signal
p(4,1000)=p(4,999);
for f=2:1000
  p(4,f)=p(4,f-1)+(p(4,f)-p(4,f-1))*.2;
end
p(4,:)=p(4,:)*10;

% Plot calcuated data
```

```
  figure (10+fileno);
  plot (p');

  % Write data to file
  filename = sprintf ('arctan%d.csv', fileno);
  outfile = fopen (filename, 'w');
  fprintf (outfile, '%f,%f,%f,%f\n', p);
  fclose (outfile);

end
```

Appendix VI Phase-locked pulsing circuit

The phase-locked pulsing circuit used in the storage loop experiment was designed using Protel 99 SE. The PCB and circuit diagram are illustrated below.

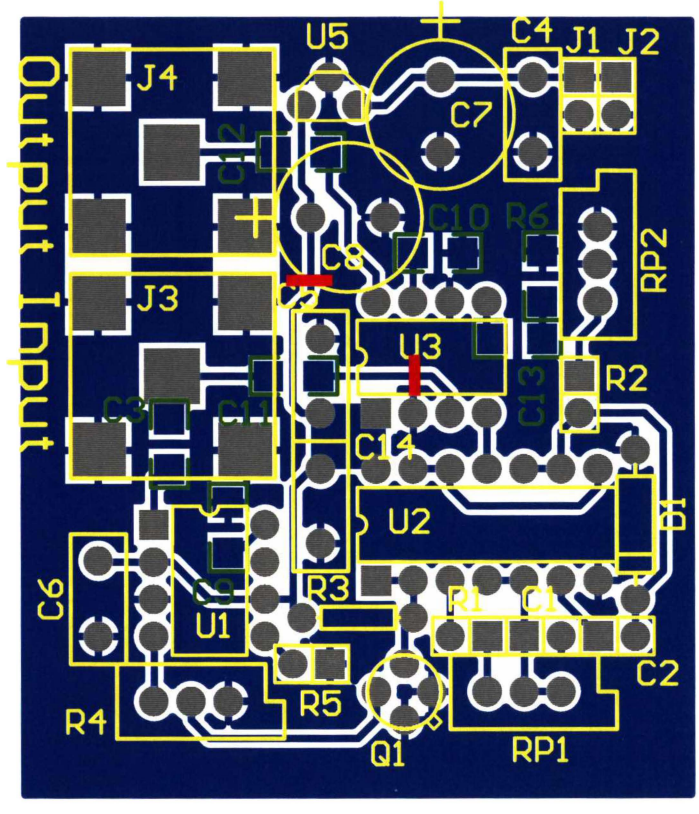

Because the PCB was single sided, additional ground links were added during assembly to make the RF current paths as short as possible. These are shown in red above.

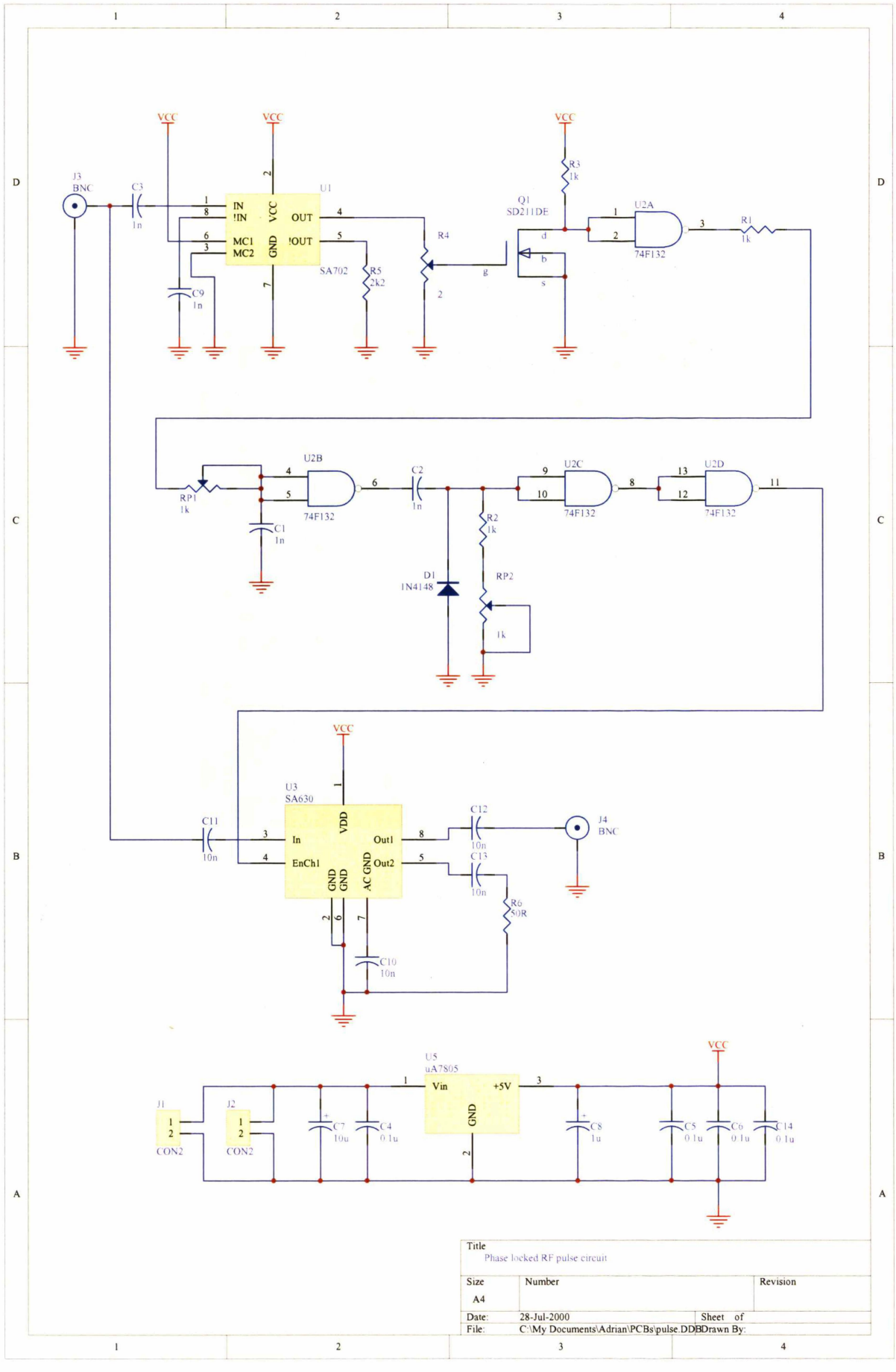
VCC
J3
BNC
C3
1n
U1
IN
!IN
MC1
MC2
VCC
GND
OUT
!OUT
SA702
R5
2k2
R4
C9
1n
Q1
SD211DE
R3
1k
U2A
74F132
R1
1k
U2B
74F132
RP1
1k
C1
1n
C2
1n
U2C
74F132
U2D
74F132
D1
1N4148
R2
1k
RP2
1k
U3
SA630
VDD
In
EnCh1
Out1
Out2
GND
GND
AC GND
C11
10n
C12
10n
C13
10n
J4
BNC
R6
50R
C10
10n
U5
uA7805
Vin
+5V
GND
J1
J2
CON2
CON2
C7
10u
C4
0.1u
C8
1u
C5
0.1u
C6
0.1u
C14
0.1u
Title
Phase locked RF pulse circuit
Size
A4
Number
Revision
Date:
28-Jul-2000
Sheet of
File:
C:\My Documents\Adrian\PCBs\pulse.DDB
Drawn By:

Appendix VII Quadrature detector circuit

The quadrature detector circuit used in the SSB frequency shifting experiment was designed using Protel 99 SE. The PCB and circuit diagram are illustrated below.

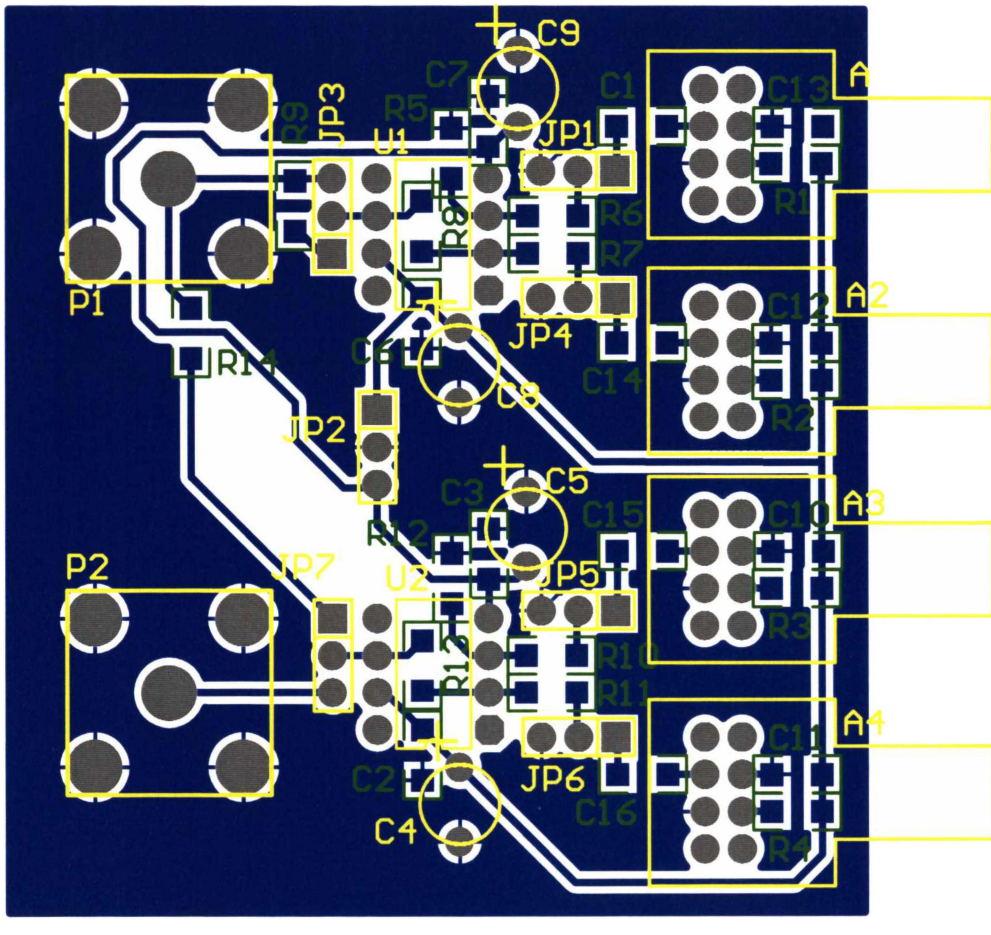

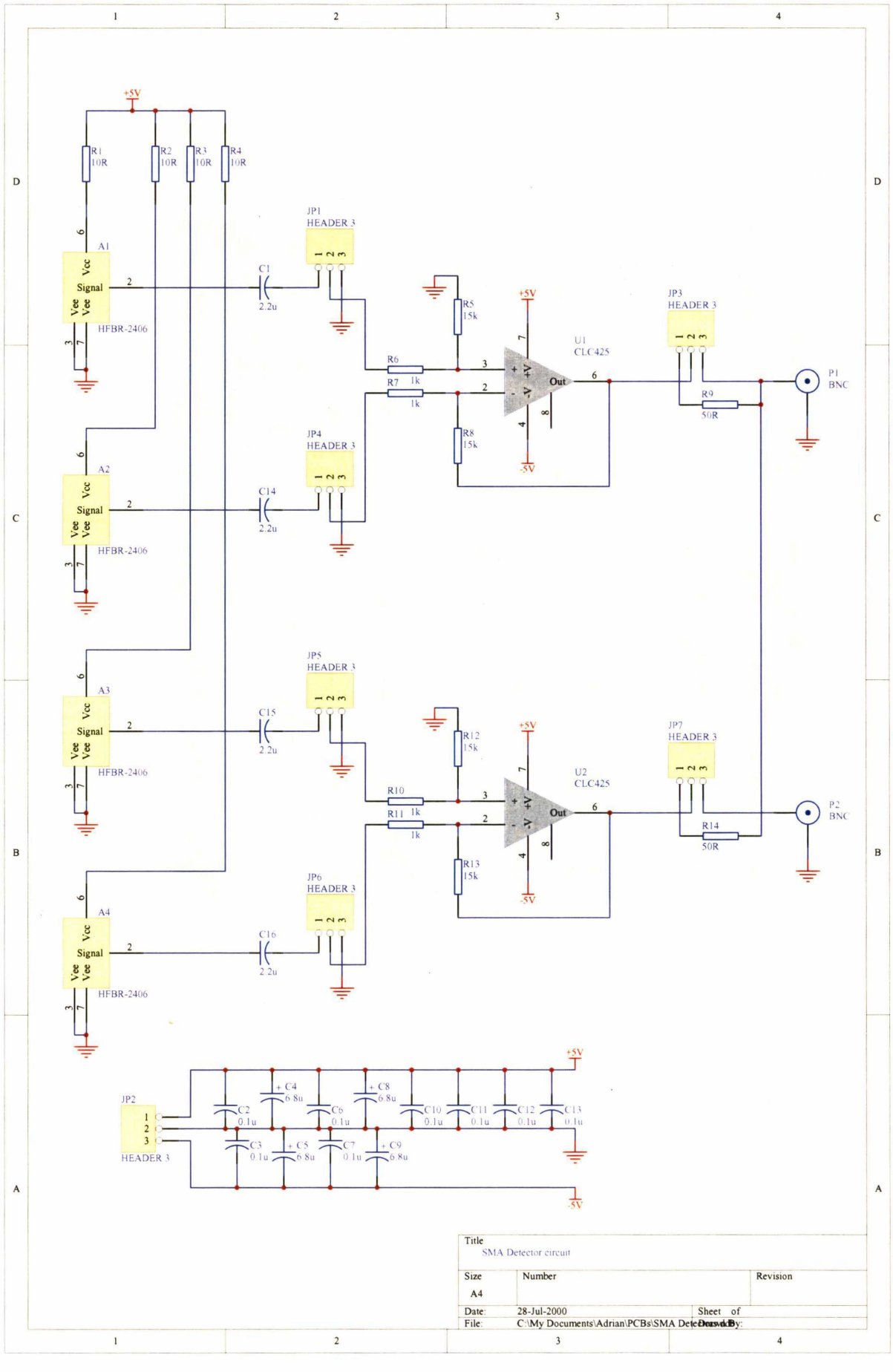
+5V
R1 10R
R2 10R
R3 10R
R4 10R
A1
Vcc
Signal
Vee
Vee
HFBR-2406
JP1 HEADER 3
C1 2.2u
R5 15k
R6 1k
R7 1k
R8 15k
U1 CLC425
Out
-5V
JP3 HEADER 3
R9 50R
P1 BNC
A2
C14 2.2u
JP4 HEADER 3
A3
C15 2.2u
JP5 HEADER 3
R10 1k
R11 1k
R12 15k
R13 15k
U2 CLC425
JP7 HEADER 3
R14 50R
P2 BNC
A4
C16 2.2u
JP6 HEADER 3
JP2 HEADER 3
C2 0.1u
C3 0.1u
C4 6.8u
C5 6.8u
C6 0.1u
C7 0.1u
C8 6.8u
C9 6.8u
C10 0.1u
C11 0.1u
C12 0.1u
C13 0.1u
Title
SMA Detector circuit
Size
A4
Number
Revision
Date: 28-Jul-2000
Sheet of
File: C:\My Documents\Adrian\PCBs\SMA Detector.ddb
Drawn By:

Appendix VIII SSB frequency shift simulation

The simulations of the SSB frequency shifting concept were performed in Mathcad. On the following pages are the simulation files for both the electronic and semi-optical configurations.

Electronic method

Total number of points in simulation:

$$N := 2^{13} \qquad N = 8.192 \times 10^3 \qquad i := 0 .. N - 1$$

Doppler signal:

$$f := 25$$

$$Sig1_i := \cos\left(2 \cdot \pi f \cdot \frac{i}{N}\right) \qquad Sig2_i := \cos\left(2 \cdot \pi \cdot f \cdot \frac{i}{N} + \frac{\pi}{2}\right)$$

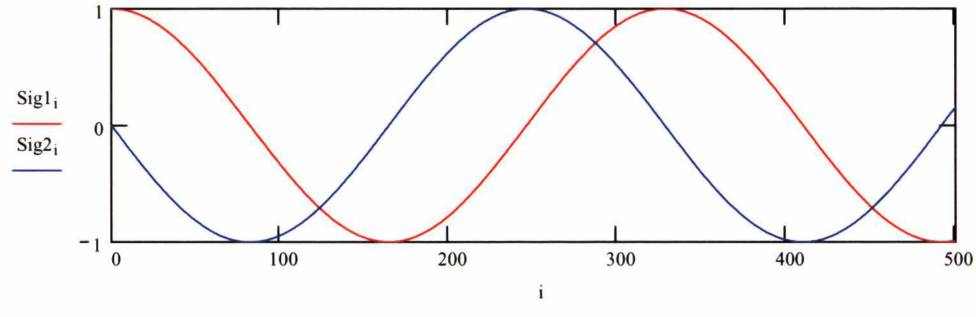

Carrier signal:

$$c := 500$$

$$Carrier1_i := \cos\left(2 \cdot \pi \cdot c \cdot \frac{i}{N}\right) \qquad Carrier2_i := \cos\left(2 \cdot \pi \cdot c \cdot \frac{i}{N} + \frac{\pi}{2}\right)$$

Double sideband signals:

$$Mod1_i := Sig1_i \cdot Carrier1_i$$

$$Mod2_i := Sig2_i \cdot Carrier2_i$$

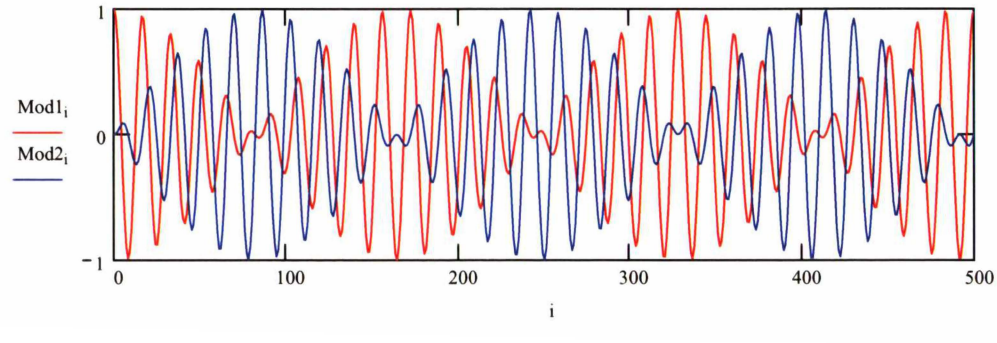

Single sideband signal

$$SSB_i := Mod1_i + Mod2_i$$

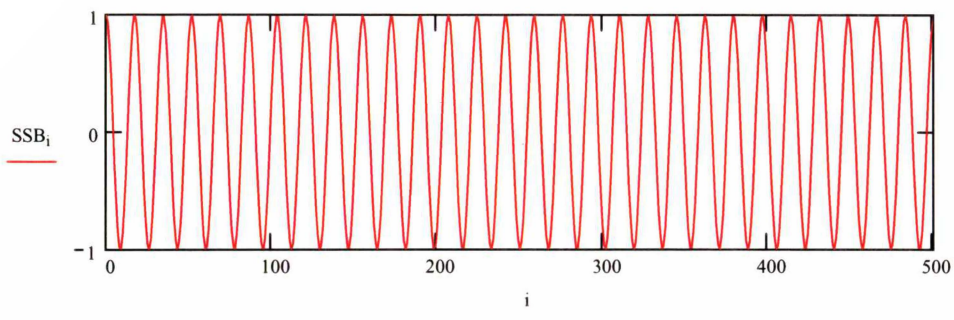

Fourier transforms:

$$FFTM1 := fft(Mod1) \qquad FFTM2 := fft(Mod2) \qquad FFTSSB := fft(SSB)$$

$$j := 0 .. \frac{N}{2}$$

Adjust sign of amplitude depending on phase, and apply offset:

$$SM1_j := |FFTM1_j| \cdot if\left(|arg(FFTM1_j)| > \frac{\pi}{2}, -1, 1\right) + 150$$

$$SM2_j := |FFTM2_j| \cdot if\left(|arg(FFTM2_j)| > \frac{\pi}{1.8}, -1, 1\right) + 75$$

$$SSSB_j := |FFTSSB_j| \cdot if\left(|arg(FFTSSB_j)| > \frac{\pi}{2}, -1, 1\right)$$

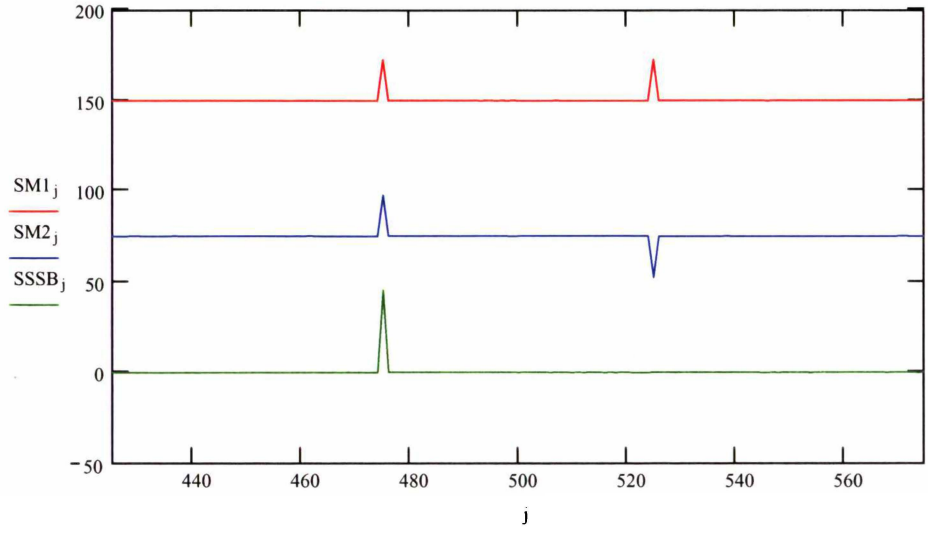

Semi-optical method

Total number of points in simulation:

$$N := 2^{13} \qquad N = 8.192 \times 10^3 \qquad i := 0 .. N - 1$$

Doppler signals:

$$f := 25$$

$$Sig1_i := \cos\left(2 \cdot \pi f \cdot \frac{i}{N}\right) + 2 \qquad Sig2_i := \cos\left(2 \cdot \pi \cdot f \cdot \frac{i}{N} + \frac{\pi}{2}\right) + 2$$

$$Sig3_i := \cos\left(2 \cdot \pi f \cdot \frac{i}{N} + \frac{2 \cdot \pi}{2}\right) + 2 \qquad Sig4_i := \cos\left(2 \cdot \pi \cdot f \cdot \frac{i}{N} + \frac{3 \cdot \pi}{2}\right) + 2$$

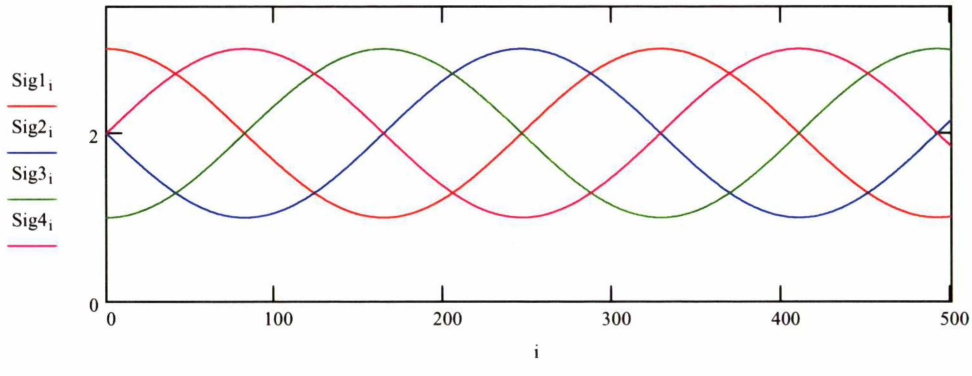

Full AM modulated signals:

$$c := 500$$

$$Carrier_i := 2^2 + 2 \cdot 2 \cdot \cos\left(2 \cdot \pi \cdot c \cdot \frac{i}{N}\right) + \cos\left(2 \cdot \pi \cdot c \cdot \frac{i}{N}\right)^2$$

$$Mod1_i := Sig1_i \cdot Carrier_i \qquad Mod3_i := Sig3_i \cdot Carrier_i$$

$$Mod2_i := Sig2_i \cdot Carrier_i \qquad Mod4_i := Sig4_i \cdot Carrier_i$$

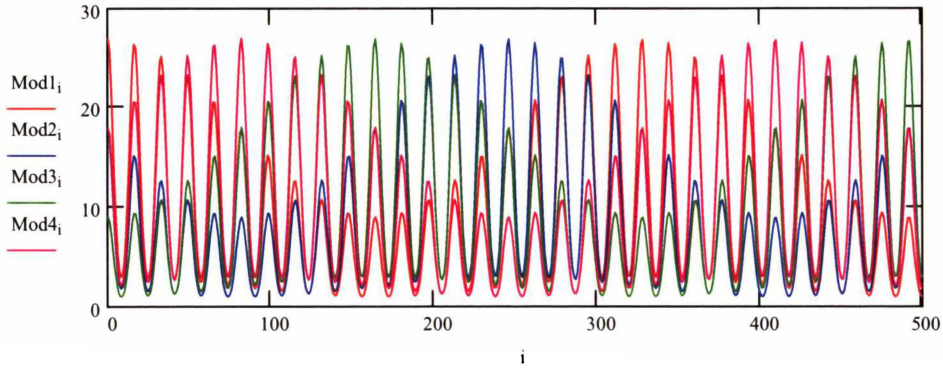

Add quarter wave delay:

$$Mod2S_i := if\left(i < floor\left(\frac{N}{c \cdot 4}\right), Mod2_{N+i-4}, Mod2_{i-floor\left(\frac{N}{c \cdot 4}\right)}\right)$$

$$Mod4S_i := if\left(i < floor\left(\frac{N}{c \cdot 4}\right), Mod4_{N+i-4}, Mod4_{i-floor\left(\frac{N}{c \cdot 4}\right)}\right)$$

Single sideband signals:

$$DSB1_i := Mod1_i - Mod3_i \qquad DSB2_i := Mod2S_i - Mod4S_i$$

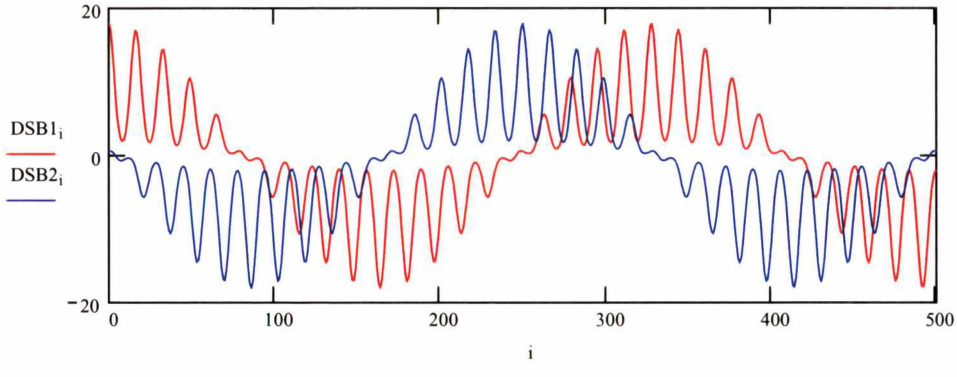

Single sideband saignal:

$$SSB_i := DSB1_i + DSB2_i$$

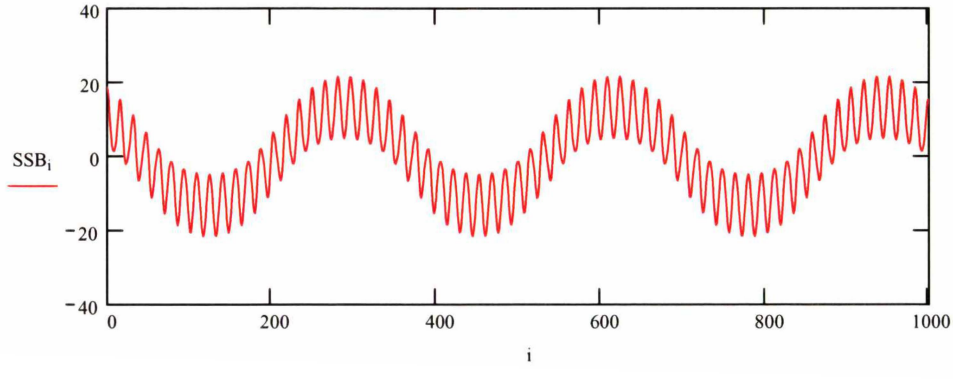

Fourier transform of AM and double sideband signal number 1:

$$FFTM1 := fft(Mod1)$$

$$FFTM2 := fft(Mod3)$$

$$FFTDSB := fft(DSB1)$$

$$j := 0 .. \frac{N}{2}$$

Adjust amplitude dependign on phase:

$$SM1_j := |FFTM1_j| \cdot if\left(|arg(FFTM1_j)| > \frac{\pi}{2}, -1, 1\right) + 800$$

$$SM2_j := |FFTM2_j| \cdot if\left(|arg(FFTM2_j)| > \frac{\pi}{1.8}, -1, 1\right) + 400$$

$$SDSB_j := |FFTDSB_j| \cdot if\left(|arg(FFTDSB_j)| > \frac{\pi}{2}, -1, 1\right)$$

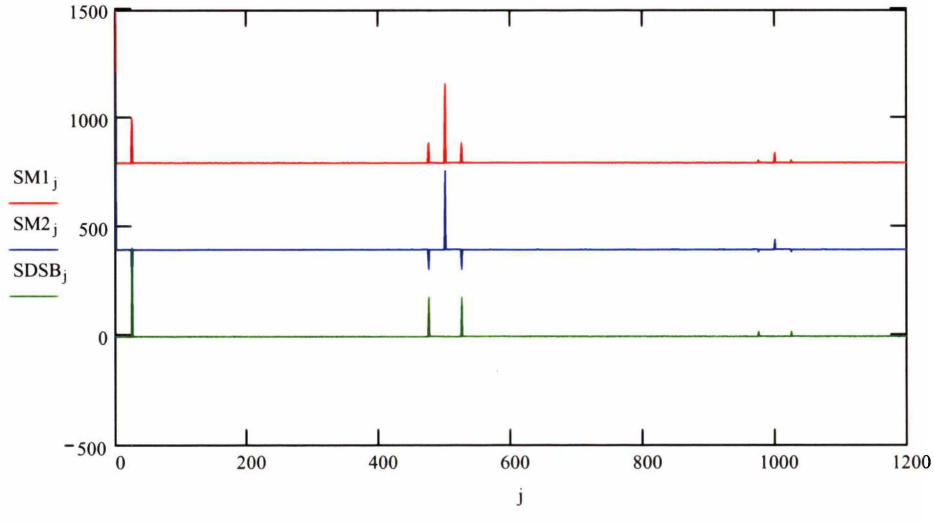

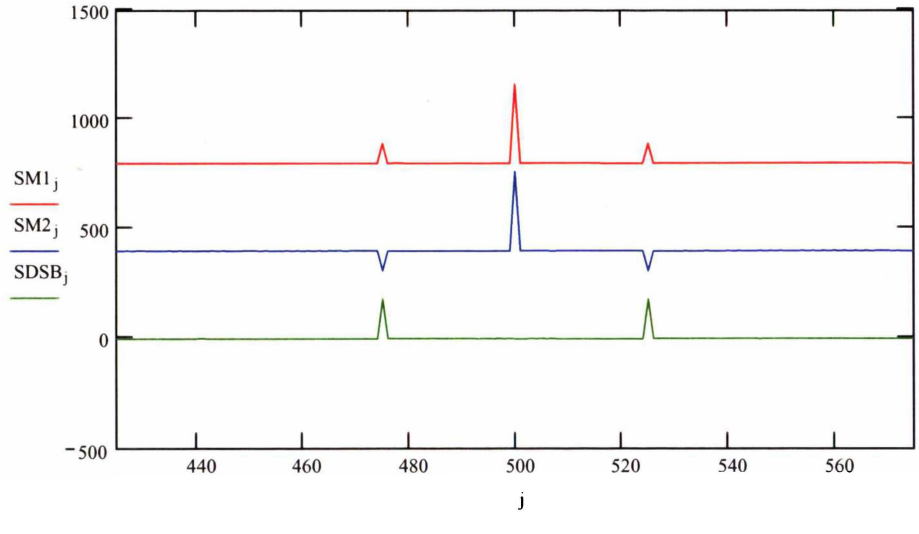

Fourier transform of AM and double sideband signal number 2:

FFTM1 := fft(Mod2S)

FFTM2 := fft(Mod4S)

FFTDSB := fft(DSB2)

Adjust amplitude dependign on phase:

$$SM1_j := |FFTM1_j| \cdot if\left(|arg(FFTM1_j)| > \frac{\pi}{2}, -1, 1\right) + 800$$

$$SM2_j := |FFTM2_j| \cdot if\left(|arg(FFTM2_j)| > \frac{\pi}{2}, -1, 1\right) + 400$$

$$SDSB_j := |FFTDSB_j| \cdot if\left(|arg(FFTDSB_j)| > \frac{\pi}{2}, -1, 1\right)$$

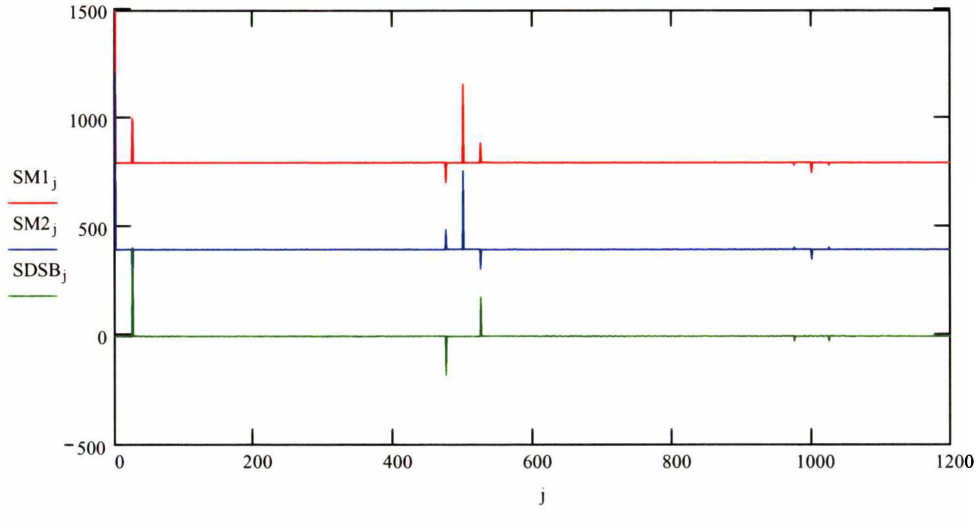

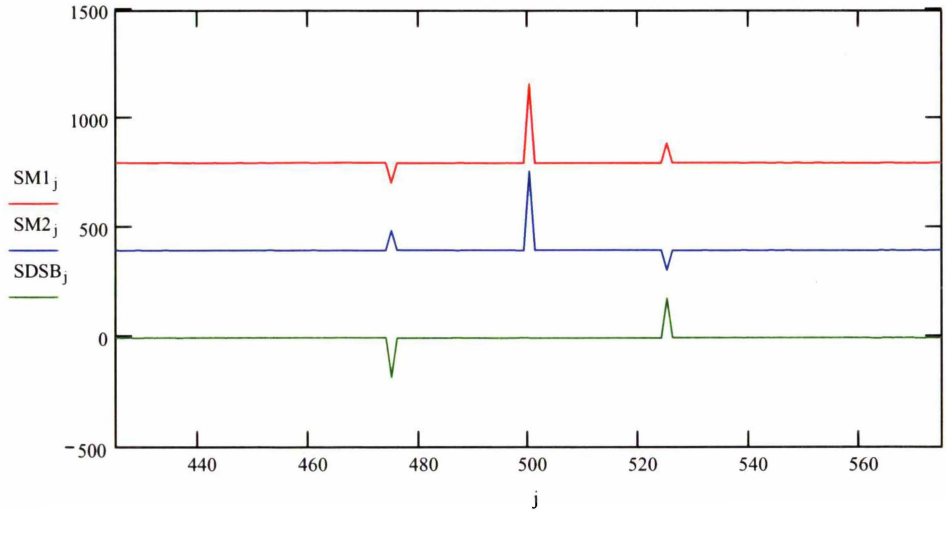

Fourier transform of double sideband and single sideband signals:

$$FFTM1 := fft(DSB1)$$

$$FFTM2 := fft(DSB2)$$

$$FFTDSB := fft(SSB)$$

Adjust amplitude dependign on phase:

$$SM1_j := \left|FFTM1_j\right| \cdot if\left(\left|arg\left(FFTM1_j\right)\right| > \frac{\pi}{2}, -1, 1\right) + 800$$

$$SM2_j := \left|FFTM2_j\right| \cdot if\left(\left|arg\left(FFTM2_j\right)\right| > \frac{\pi}{1.8}, -1, 1\right) + 400$$

$$SDSB_j := \left|FFTDSB_j\right| \cdot if\left(\left|arg\left(FFTDSB_j\right)\right| > \frac{\pi}{2}, -1, 1\right)$$

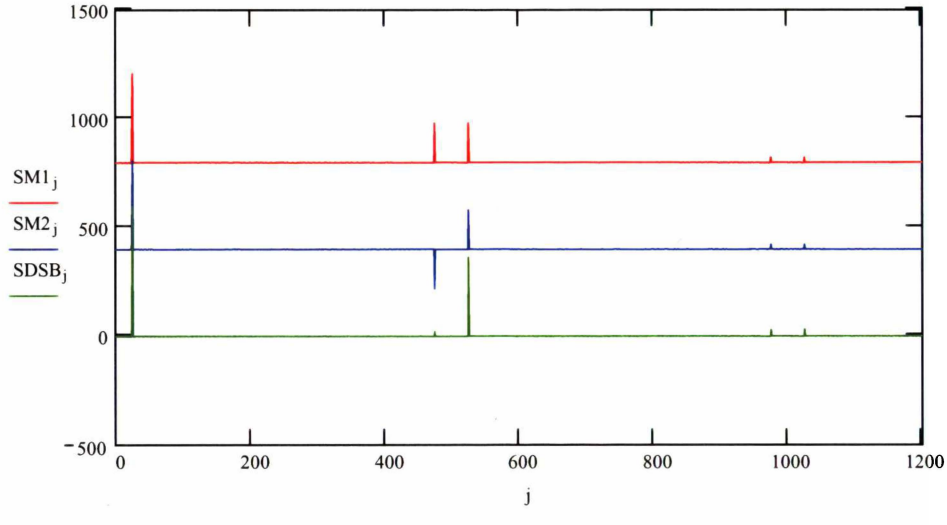

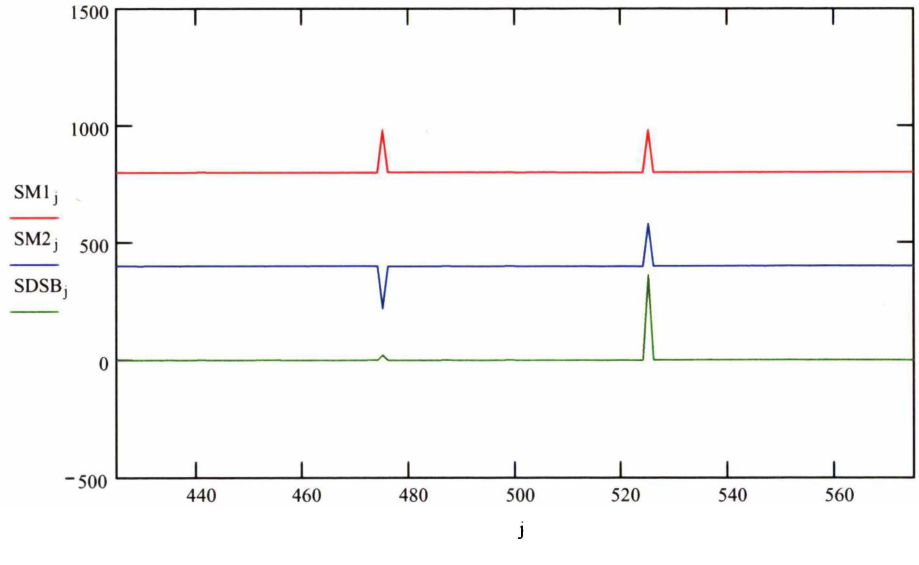

Appendix IX References

Agrawal GP. 1997. *Fibre-optic communication systems.* John Wiley & Sons Inc., New York, USA.

Agrawal YC. 1984. *Quadrature demodulation in laser Doppler velocimetry.* Appl. Opt. **23**(11), 1685-1686.

Biselli E and Werner C. 1989. *Determination of the direction of motion on the basis of cw-homodyne laser Doppler radar.* Appl. Opt. **28**(5), 915-920.

Bissonnette LR. 1996. *Multiple-scattering lidar equation.* Appl. Opt. **35**(33), 6449-6465.

Bohren CF. 1995. 'Scattering by Particles' in *Handbook of optics volume 1: Fundamentals, Techniques, and Design.* Ed. M Bass, EW Van Stryland, DR Williams, and WL Wolfe. Mcgraw-Hill, New York, USA, pp. 6.1-6.21.

Born M and Wolf E. 1980. *Principles of optics.* Pergamon Press, Oxford, Great Britain.

Czarske J and Dölle O. 1998. *Quadrature demodulation techniques used in laser Doppler velocimetry.* Electron. Lett. **34**(6), 547-549

Czarske J, Hock F, and Müller H. 1993. 'Quadrature demodulation – A new LDV-burst frequency estimator' in *Proc. of SPIE. Laser Anemometry advances and applications.* **2052**, 79-86.

Czarske JW and Müller H. 1996. *Two-dimensional directional fiber-optic laser Doppler anemometer based on heterodyning by means of a chirp frequency modulated Nd:YAG miniature ring laser.* Opt. Commun. **132**, 421-426.

DiMarzio CA and Lindberg SC. 1992. *Signal-to-noise-ration equations for a heterodyne laser radar.* Appl. Opt. **31**(21), 4240-4246.

Dorrington A and Künnemeyer R. 1998. *Electronic processing of small displacement Doppler signals.* ACOLS 98 Australasian Conference on Optics, Lasers and Spectroscopy, University of Canterbury, Christchurch, New Zealand. Dec. 14-17, p36.

Dorrington AA, Künnemeyer R, and Danehy PM. 1999. 'Reference beam storage for long range low coherence pulsed Doppler lidar', *Proc. of the Second Australian Conference on Laser Diagnostics in Fluid Mechanics and Combustion*, Monash University, Melbourne, Australia. Dec. 9-10, pp74-79.

Drain LE. 1980. *The laser Doppler technique.* John Wiley & Sons Inc., Chichester, Great Britain.

Fischer KW, Abreu VJ, Skinner WR, Barnes JE, Mcgill MJ, and Irgang TD. 1995. *Visible wavelength Doppler lidar for measurement of wind and aerosol profiles during the day and night.* Opt. Eng. **34**(2), 499-511.

Follett DH. 1981. *A frequency shift maximum frequency follower Doppler demodulator with amplitude correction.* Clin. Phys. Physiol. Meas. **2**(4), 277-284.

Frehlich RG. 1990. *Conditions for optimal performance of monostatic coherent laser radar.* Opt. Lett. **15**(11), 643-645.

Fürstenau N and Schmidt M. 1998. *Fiber-optic extrinsic Fabry-Perot interferometer vibration sensor with two-wavelength passive quadrature readout.* IEEE Trans. Instrum. Meas. **47**(1), 143-147.

Gras JL and Jones WD. 1989. *Australian aerosol backscatter survey.* Appl. Opt. **28**(5), 852-856.

Haywood JH. 1991. 'Erbium amplifier recirculation optical delay line', *Proc. of the 16th Australian Conference on Optical Fibre Technology.* Adelaide, Australia, Dec. 1-4, pp298-301.

Henderson SW, Suni PJM, Hale CP, Hannon SM, Magee JR, Bruns DL, and Yuen EH. 1993. *Coherent laser radar at 2μm using solid-state lasers.* IEEE Trans. Geosci. Remote Sensing. **31**(1), 4-15.

Ikeda Y and Nakajima T. 1996. *Burst digital correlator as laser-Doppler velocimetry signal processor.* Appl. Opt. **35**(18), 3243-3249.

James JF. 1995. *A student's guide to Fourier transforms : with applications in physics and engineering.* Press Syndicate of the University of Cambridge, Cambridge, Great Britain.

Kavaya MJ, Henderson SW, Magee JR, Hale CP, and Huffaker R.M. 1989. *Remote wind profiling with a solid-state Nd:YAG coherent lidar system.* Opt. Lett. **14**(15), 776-778.

Koo KP, Tveten AB, and Dandridge A. 1982. *Passive stabilization scheme for fiber interferometers using (3X3) fiber directional couplers.* Appl. Phys. Lett. **41**(7), 616-618.

Korb CL, Gentry BM, and Li SX. 1997. *Edge technique doppler lidar wind measurements with high vertical resolution.* Appl. Opt. **36**(24), 5976-5983.

Lang T, Genon-Catalot D, Dandrea P, Duport IS, and Benech P. 1998. *Integrated optical displacement sensor with four quadrature phase-shifted output signals.* J. Opt. **29**(3), 135-140.

Lo YL, and Sirkis JS. 1995. *Passive demodulation techniques for michelson and polarimetric optical fibre sensors.* Exp. Tech. **19**(3), 23-27.

Lo YL, Sirkis JS, and Fourney WL. 1997. *In-fiber Doppler velocimeter for velocity measurements or moving surfaces.* Exp. Mech. **37**(3), 328-332.

McGill MJ and Skinner WR. 1997. *Multiple fabry-perot interferometers in an incoherent Doppler lidar.* Opt. Eng. **36**(1), 139-145.

McGill MJ and Spinhirne JD. 1998. *Comparison of two direct-detection Doppler lidar techniques.* Opt. Eng. **37**(10), 2675-2686.

Menzies RT and Tratt DM. 1994. *Airborne CO_2 coherent lidar for measurements of atmospheric aerosol and cloud backscatter.* Appl. Opt. **33**(24), 5698-5711.

Mocker HW and Wagener TJ. 1994. *Laser Doppler optical air-data system: feasibility demonstration and systems specification.* Appl. Opt. **33**(27), 6457-6471.

Müller H, Strunck V, and Dopheide D. 1997. *The application of quadrature demodulation techniques for the investigation of flows.* Flow Measur. Instrum. **7**(3/4), 237-245.

Nakatani N, Muneo T, and Yamada T. 1984. *LDV using polarization-preserving optical fibers from simultaneous measurement of two velocity components.* Appl. Opt. **23**(11), 1686-1687.

NASA. 1992a. *Tests show fewer air pockets.* Aerospace Technology Innovation. **6**(3), 8.

NASA. 1992b. 'Making the skies safe from windshear', *NASA Facts Online.* http://oea.larc.nasa.gov/PAIS/Windshear.html, (accessed 1 July 2000).

NASA. 1998. 'ACLAIM: Airborne coherent LIDAR for advanced in-flight measurement', *NASA Facts.* FS 1998-04-042-DFRC, http://trc.dfrc.nasa.gov/PAO/PAIS/PDF/FS-042-DFRC.pdf, (accessed 1 July 2000).

Niemeier Th and Ulrich R. 1986. *Quadrature outputs from fiber interferometer with 4X4 coupler.* Opt. Lett. **11**(10), 677-679.

Richter P, Péczeli I, and Böröcz S. 1994. *Coherent infrared lidar with enhanced optical heterodyne detection.* J. Mod. Opt. **41**(11), 2079-2084.

Rogers PL. 1989. *Wind shear detector.* US Patent 4,875,770.

Rye BJ and Hardesty RM. 1993a. *Discrete spectral peak estimation in incoherent backscatter heterodyne lidar. I: Spectral accumulation and the Caramer-Rao lower bound.* IEEE Trans. Geosci. Remote Sensing. **31**(1), 16-27.

Rye BJ and Hardesty RM. 1993b. *Discrete spectral peak estimation in incoherent backscatter heterodyne lidar. II: Correlogram Accumulation.* IEEE Trans. Geosci. Remote Sensing. **31**(1), 28-35.

Rye BJ and Hardesty RM. 1997a. *Detection techniques for validating Doppler estimates in heterodyne lidar.* Appl. Opt. **36**(9), 1940-1951.

Rye BJ and Hardesty RM. 1997b. *Estimate optimisation pareters for incoherent backscatter heterodyne lidar.* Appl. Opt. **36**(36), 9425-9436.

Saleh BEA and Teich MC. 1991. *Fundamentals of Photonics.* John Wiley & Sons Inc., New York, USA.

Sheem SK. 1980. *Fiber-optic gyroscope with [3X3] directional coupler.* App. Phys. Lett. **37**(10), 869-871.

Singh UN. 1997. 'Lidar for atmospheric remote sensing' in *Optical measurement techniques and applications.* Ed. PK Rastogi. Artech House Inc., Boston, USA.

Spinhirne JD, Chudamani S, Cavanaugh JF, and Bufton JL. 1997. *Aerosol and cloud backscatter at 1.06, 1.54 and 0.53μm by airborne hard-target-calibrated Nd:YAG/methane Raman lidar.* Appl. Opt. **36**(15), 3475-3490.

Sroga JT, Petheram JC, Bowers MS, Romea R, and Lee RW. 1994. *Frequency spectral measurements of a pulsed, TE CO_2 laser incorporating LAWS transmitter design features*, J. Mod. Opt. **41**(11), 2085-2100.

Stoyanov DV, Bratanov BM, and Stoykova EV. 1995. *Novel wide-band lidar detection technique.* Rev. Sci. Instrum. **66**(3), 2400-2404.

Stoyanov DV, Gurdev LL, Kolarov GV, and Vankov OI. 2000. *Lidar profiling by long rectangular-like chopped laser pulses.* Opt. Eng. **39**(6), 1556-1567.

Targ R, Steakley BC, Hawley JG, Ames LL, Forney P, Swanson D, Stone R, Otto RG, Zarifis V, Brockman P, Calloway RS, Klein RS, and Robinson PA. 1996. *Coherent lidar airborne wind sensor II: flight-test results at 2 and 10 mm.* Appl. Opt. **35**, 7117-7127.

Tatterson KG. 1998. *Avionics looks to photonics to watch turbulent skies.* Photo. Spect. **32**(2), 20-21.

Tippler PA. 1983. *Physics.* Worth Publishers Inc., New York, USA.

Tratt DM and Menzies RT. 1994. *Recent climatological trends in atmospheric aerosol backscatter derived from the Jet Propulsion Laboratory multiyear backscatter profile database.* Appl. Opt. **33**(3), 424-429.

Veen DT, Sikken BH, Krommendijk FN, and Koonen AMJ. 1998. 'Modelling dynamic behaviour of Erbium doped fibre amplifers in all-optical ring networks' in *Proc. of SPIE. All-optical networking: Architecture, control, and management issues.* **3531**, 39-44.

Weir K, Boyle WJO, Palmer AW, Grattan KTC, and Meggitt BT. 1991. *A novel processing scheme for a fibre optic low coherence laser Doppler anemometer*, IEE Colloquium on 'Optical Techniques and Biomedical Applications' **128**, 9/1-4.

Woodfield AA. 1986. *Wind shear detection.* US Patent 4,585,341.

Yariv A. 1996. *Optical electronics in modern communications.* Oxford University Press, New York, USA.

Zeines B. 1970. *Electronic communications systems.* Prentice-Hall, Englewood Cliffs, USA.

Zeitler R. 1997. *Digital correlator for measuring the velocity of solid surfaces.* IEEE Trans. Instrum. Meas. **46**(4), 803-806.

Zhao Y, Post MJ, and Hardesty RM. 1990a. *Receiving efficiency of monostatic pulsed coherent lidars. 1: Theory.* Appl. Opt. **29**(28), 4111-4119.

Zhao Y, Post MJ, and Hardesty RM. 1990b. *Receiving efficiency of monostatic pulsed coherent lidars. 2: Applications.* Appl. Opt. **29**(28), 4120-4132.